Friedrich-Alexander-Universität
Erlangen-Nürnberg

ERLANGEN CENTRE
FOR ASTROPARTICLE
PHYSICS

From the Lab to the Telescopes – Intensity Interferometry with H.E.S.S.

Vom Labor zu den Teleskopen – Intensitätsinterferometrie mit H.E.S.S.

Der Naturwissenschaftlichen Fakultät der Friedrich-Alexander-Universität Erlangen-Nürnberg zur Erlangung des Doktorgrades Dr. rer. nat.

vorgelegt von **Andreas Zmija** aus Erlangen

June 2024

From the Lab to the Telescopes – Intensity Interferometry with H.E.S.S.

Vom Labor zu den Teleskopen – Intensitätsinterferometrie mit H.E.S.S.

Der Naturwissenschaftlichen Fakultät der Friedrich-Alexander-Universität Erlangen-Nürnberg zur Erlangung des Doktorgrades Dr. rer. nat.

vorgelegt von **Andreas Zmija** aus Erlangen

Als Dissertation genehmigt von der Naturwissenschaftlichen Fakultät
der Friedrich-Alexander-Universität Erlangen-Nürnberg

Tag der mündlichen Prüfung:
19.09.2024

Gutachter/in:
Prof. Dr. Stefan Funk
Prof. Dr. Gisela Anton

Abstract

High angular resolution optical imaging with traditional telescopes is constrained by the diffraction limit defined by the telescope's diameter. As constructing ever larger apertures is prohibitively expensive and complex, astronomers make use of interferometric techniques, where the light information from different telescopes is combined. The limiting factor in angular resolution is then the separation between the telescopes rather than their individual sizes. Stellar intensity interferometers measure correlations in the flux of photons (an effect called *photon bunching*) detected by separated telescopes, and by subsequent analysis the angular sizes of stellar objects can be determined. In contrast to amplitude interferometers, an intensity interferometer is almost insensitive to atmospheric turbulence, and works without the need to optically combine the electromagnetic waves at wavelength-scale precision.

The design of an astronomical intensity interferometer can be simplified to a light collector (telescope) focusing light into a photo-detector. Initially developed in the 1950s by Hanbury Brown and Twiss, efforts were discontinued due to too low signal-to-noise for faint stars – a fundamental characteristic of intensity interferometric measurements. However, technological developments yielded high time resolution photo-detectors and electronics, as well as the construction of large light collector telescopes, which both counteract low signal-to-noise. Given that the telescopes do not need high optical quality, arrays of Imaging Atmospheric Cherenkov Telescopes – constructed in recent decades primarily for the purpose of measuring gamma- and cosmic rays – have been identified as ideal candidates to revive stellar intensity interferometry at optical wavelengths.

This thesis describes the development of an intensity interferometry application for use at the High Energy Stereoscopic System (H.E.S.S.) – a gamma-ray telescope array located in Namibia. Initial measurements in the laboratory are presented, which were performed to characterize the photon correlations, statistical noise and potential sources of systematic noise. Photon bunching was detected in LED light, measured at low photon rates in photon time-tagging mode, as well as in light of a xenon lamp, measured at high photon rates in photo-current sampling mode. In both cases, the interferometer was found to operate at the theoretical sensitivity limit.

A comparison study between two approaches towards stellar intensity interferometry, the "high photon rates" approach (pursued in this thesis) versus the "high time resolution" approach by collaborators, was then carried out in a measurement of a xenon lamp. Signal-to-noise investigations showed that systems that can sustain high photon rates by sampling the photo-current are suitable at large telescopes, while systems with very high time-resolution are suitable for arrays of small optical telescopes.

In 2022, the intensity interferometer was installed onto two of the H.E.S.S. telescopes, and measurements of three bright star systems were performed. Angular uniform disk diameters of the single star σ Sgr as well as of the two primary components in the (effective) binary star system λ Sco – assuming equal stellar diameters – were measured to be (0.52 ± 0.07) mas and (0.49 ± 0.06) mas, respectively.

An outlook to the potential of intensity interferometry with future telescopes is given.

Zusammenfassung

Die optische Bildgebung mit hoher Winkelauflösung ist in traditionellen Teleskopen beugungsbegrenzt, defininert durch den Durchmesser des Teleskops. Da der Bau immer größerer Teleskope zunehmend teuer und komplex wird, benutzen Astronomen interferometrische Techniken, bei denen Lichtinformation von verschiedenen Teleskopen kombiniert wird. Der limitierende Faktor bei der Winkelauflösung ist dann die Entfernung der Teleskope, nicht ihre Größe. Stellare Intensitätsinterferometer messen Korrelationen im Fluss der Photonen (ein Effekt, der *Photon Bunching* genannt wird), detektiert mit separaten Teleskopen, und durch anschließende Analyse kann die Winkelgröße stellarer Objekte bestimmt werden. Im Gegensatz zu Amplitudeninterferometern ist ein Intensitätsinterferometer nahezu unempfindlich gegenüber atmosphäerischen Turbulenzen, und funktioniert ohne die Notwendigkeit, die elektromagnetischen Wellen mit einer Präzision in der Größenordnung der Wellenlänge zu kombinieren.

Das Design eines astronomischen Intensitätsinterferometers besteht vereinfacht dargestellt aus einer Lichtsammelfläche (Teleskop), die das Licht in einen Photodetektor fokussiert. Ursprünglich in den 1950er Jahren von Hanbury Brown und Twiss entwickelt, wurden Bemühungen aufgrund von zu geringem Signal-to-Noise bei leuchtschwachen Sternen eingestellt – eine grundlegende Charakteristik intensitätsinterferometrischer Messungen. Allerdings führten technologische Entwicklungen zu Photodetektoren und Elektronik mit hoher Zeitauflösung, sowie zum Bau von Teleskopen mit riesigen Lichtsammelflächen, was beides dem schwachen Signal-to-Noise entgegenwirkt. Angesichts der Tatsache, dass die Teleskope nicht über eine hohe optische Qualität verfügen müssen, wurden Arrays von Imaging Atmospheric Cherenkov Telesopes – errichtet in den letzten Jahrzehnten hauptsächlich für die Messung von Gamma- und kosmischer Strahlung – als ideale Kandidaten identifiziert, um stellare Intensitätsinterferometrie in optischen Wellenlängen wieder aufleben zu lassen.

Diese Arbeit beschreibt die Entwicklung einer Intensitätsinterferometrie-Anwendung zur Benutzung am High Energy Stereoscopic System (H.E.S.S.) – einem Gammastrahlenteleskop in Namibia gelegen. Anfängliche Messungen im Labor werden vorgestellt, welche durchgeführt wurden, um die Photonenkorrelationen, statistisches Noise und möglichen Quellen von systematischem Noise zu charakterisieren. Photon Bunching wurde in LED Licht detektiert, gemessen bei geringen Photonenraten im Photon-Time-Tagging Modus, sowie in Licht einer Xenonlampe, gemessen bei hohen Photonenraten im Photostrom-Sampling Modus. In beiden Fällen arbeitete das Interferometer am theoretischen Sensitivitätslimit. Eine Vergleichsstudie zwischen zwei Ansätzen für stellare Intensitätsinterferometry, der "Hohe Photonenraten"-Ansatz (der in dieser Arbeit verfolgt wird) gegen den "hohe Zeitauflösung"-Ansatz von Kollaboratoren, wurde dann durch Messungen mit einer Xenonlampe durchgeführt. Signal-to-Noise-Untersuchungen haben gezeigt, dass Systeme, die mit hohen Photonenraten umgehen können indem sie den Photostrom messen, für große Teleskope geeignet sind, während Systeme mit sehr hoher Zeitauflösung in Arrays kleiner optischer Teleskope passen. Im Jahr 2022 wurde das Intensitätsinterferometer in zwei H.E.S.S. -Teleskopen installiert, und Messungen von drei hellen Sternsystemen durchgeführt. Uniform-Disk-Winkeldurchmesser des Einzelsternes σ Sgr sowie von den zwei Hauptkomponenten im (effektiven) Doppelsternsystem λ Sco – unter der Annahme gleicher Sternendurchmesser – wurden zu (0.52 ± 0.07) mas bzw. (0.49 ± 0.06) mas gemessen. Ein Ausblick auf das Potenzial von Intensitätsinterferometrie mit zukünftigen Teleskopen wird gegeben.

Contents

CHAPTER 1

A General and Personal Introduction

"Aus punktgroßen Sternen sickert das Licht
Einmal durch die Galaxie uns direkt ins Gesicht"
Friedrich Kautz

It is not surprising that romantics all around the (German-)speaking part of the world are falling for lines like these. However, such lyrics might qualify the creator as an artist, but certainly not as an astrophysicist. It raises the suspicion that the songwriter does not own an array of telescopes standing in his backyard, which he could combine as an interferometer, only to realize that the stars in the night sky are not point-like.

But why are human eyes, and even ordinary (amateur) telescopes insufficient to come to this conclusion, and are not able to resolve the stellar disks of even the stars closest to our solar system? Stars other than the Sun are so distant that they appear extremely small, and it is natural to assume that one needs increasingly larger detectors in order to explore increasingly smaller objects in the sky. But it requires the considering of the wave-like nature of light (or any messenger that is used for the study) in order to physically understand why the angular resolution of a telescope is defined and limited by its aperture. There are different ways on how to deal with this *diffraction limit*, and while the invention of astronomical interferometers seemed to find a loophole to escape the dilemma of building progressively larger telescopes, new technical problems arose.

Collecting the light information from multiple (potentially small) apertures overcomes the need for large telescope aperture sizes, but instead requires combining the light from telescopes, that may be hundreds of meters apart, at a precision on the scale of micrometers or less. This sets a new limit on the possible angular resolution, defined by the largest distance two telescopes can have, while the combination of the light between them is still precise enough to measure interference. Turbulences in the atmosphere that the light has to travel through add to this difficulty.

A conceptually similar, but slightly different technique is the method of *intensity interferometry*, where correlations of the light intensities recorded in different telescopes are observed. The strength of the correlation is the messenger of the star's geometry. In contrast to the aforementioned interferometers, one does not need to optically combine and interfere the light, but can record the light intensities at the telescopes independently, except that the clocks of the measurement apparatuses must be synchronized.

There are not many research areas which have developed as rapidly and dynamically as the field of stellar intensity interferometry in recent years. When I was first introduced to the concept in August 2017, as I started to work on laboratory intensity interferometry experiments in the course of my master's thesis, the only published astronomical measurements that existed so far dated back to the late 1950s until early 1970s by Robert Hanbury Brown and Richard Q. Twiss [1, 2, 3, 4], two physicists who undoubtedly can be called the pioneers of intensity interferometry. The narrative, however, was that an exciting future lies ahead of us with intensity interferometers that - implemented into large telescope arrays - will provide micro-arcsecond resolutions for imaging of astronomical objects in the optical [5, 6, 7]. And it was precisely at this time when first successful intensity interferometry measurements with starlight after more than 40 years began to appear. In 2017 Guerin at al. measured the *photon bunching* signature of three stars with a 1 m diameter telescope near Nice [8], the first successful on-sky measurement of what could be called the second wave of stellar intensity interferometry.

Now, just 6 years later, not only do additional proofs of concept like photon bunching measurements of Vega in Asiago [9] or at a telescope in Bamberg of only 0.5 m in diameter [10] exist, but intensity interferometry applications have also been implemented into the VERITAS [11] and MAGIC [12] arrays of large Imaging Atmospheric Cherenkov Telescopes (IACTs), which are now performing routine observations with an intensity interferometry program.

But how can this rapid rise in interest and progress in this technique be explained, especially after the long stalling period? A comprehensive explanation requires some introduction into the history and challenges of stellar imaging, and especially the challenges of intensity interferometers, which is given in chapter 2. In short, stellar intensity interferometry typically struggles to achieve high signal-to-noise observations. And while the pool of available large telescopes was very limited in the 1960s and 1970s, the amount of big light "buckets" - a term introduced by Hanbury Brown in his book about intensity interferometry [13] - has increased in the last decades, especially with the construction of several IACT arrays. Even though optically crude, IACT layouts satisfy the requirements to act as potential intensity interferometers. When at the beginning of the 21st century there were only a handful of people rethinking this technique in the context of modern IACT arrays [14, 15, 5], the second wave of the intensity interferometry "virus" infected all three famous current IACT arrays, with H.E.S.S. now being the latest one to establish an intensity interferometry program.

I consider myself very lucky that I had the chance to participate in the project from the very beginning: testing the first hardware in form of photomultiplier tubes, amplifiers and digitizers, developing the first software code on correlating time-tagged photons in two channels, and executing the first experiments in the laboratory with very controllable sources of very high coherence times. And I had the chance to follow, shape, design, and guide this project on its path to field experiments with on-sky sources at the H.E.S.S. telescope array in Namibia.

Major parts of this road build the structure of this thesis, along four publications which are the record of this progress. References to the publications are included in this thesis, and each chapter revolves around the content of the corresponding publication while placing them in the larger context. In addition, several key aspects that are discussed in the publications are explained in more detail.

Chapter 3 revolves around laboratory experiments with an LED, which shows thermal light characteristics, with moderate photon rates of about 10 MHz. The interferometer was operated in photon counting mode by time tagging the arrival times of photons in both interferometer arms. The simple design of the interferometer helped to understand the parameter space in which intensity interferometry measurements can be performed. In addition, concrete mathematical calculations of signal-to-noise are introduced in this chapter.

Chapter 4 extends the previously limited parameter of the observable photon rates by changing to an interferometer which is not time-tagging photons any more, but instead continuously digitizing the photo-current from the used photomultipliers. Several changes in the setup as well as in the analysis that had to be made in comparison to the time-tagging interferometer are explained, and eventually measurements at very high photon rates of up to 4.7 GHz are performed.

A quantitative comparison between these two concepts is provided in chapter 5. A collaborative measurement was performed with another working group, who pushes the concept of time-tagging to its limits. The conclusion is that a time-tagging system is more suitable for smaller optical telescopes, where improvements in time resolution can increase the signal-to-noise of the measurement, while the current-correlation is the method of choice for large, often IACT-like telescopes, where the high photon statistics act positively on the signal-to-noise.

Finally, in chapter 6, the current correlation setup is installed on two of the *Phase I* telescopes of H.E.S.S., and measurements of multiple stars and star systems are performed. Additional hardware elements are described, such as motorized elements which can remotely guide the focus into the interferometer. Further, new software was implemented, especially for the optical path delay compensation, which re-synchronizes the induced time delay between the recorded photons due to differently long travel times to the telescopes. With the strongest result of the measurement campaign, a measurement of the angular diameter of Nunki (σ Sgr), the experimental part of this thesis closes, and an outlook into the future of IACT intensity interferometry is given in chapter 7.

As the publications build the main structure of this work, their sections and equations are occasionally referenced. To make clear that the references point to the publications, and not to sections or equations in the system of this thesis, they are marked in this style. Whenever one reads something like section 4 or equation 7, it refers to section 4 or equation 7 in the publication the chapter is based on.

Chapter 2

Basics of Astronomical Interferometry

This chapter contains the general ideas of astronomical interferometry, as well as the challenges of stellar interferometers. Even though this work is specifically concerned with intensity interferometry, the reader will encounter a lot of physics and concepts that are related to astronomical interferometers in general. In fact, the basic concept of coherence is first introduced in the context of amplitude interferometry. The reason for this approach is that the idea of intensity interferometry is conceptually very similar to that of amplitude interferometry, but less intuitive. Therefore, after first getting familiarized with first-order coherence effects, which are made use of by amplitude interferometers, the transition to second-order coherence is made, as it is observed in intensity interferometry, where all of the important quantities for amplitude interferometry appear as well, but in a slightly different fashion.

The common thread of this chapter is as follows: first it will become apparent why direct imaging of astronomical sources becomes impractical if very high angular resolution is required. Thereupon, the basic concept of the Michelson (amplitude) interferometer is introduced and expanded to the introduction of coherence, and the way amplitude interferometers exploit spatial coherence information. The challenges and limits of modern amplitude interferometers are pointed out, which leads to the idea of using intensity interferometry to potentially overcome these limits. The concepts of amplitude interferometry will be adapted to the observable quantities of intensity interferometry, and an introduction of the famous *Narrabri Stellar Intensity Interferometer*, as well as into modern intensity interferometers is given.

2.1 Angular Sizes in Astronomy

Resolving the disks of a star - meaning the two-dimensional image of the (mostly) spherical shape of a star - is a very challenging task for any star other than the Sun. Even though the diameters of most stars are at least one order of magnitude larger than the diameters of planets in our solar system, their distance makes them appear smaller than most solar system objects which can be observed from ground based observatories.

To deal with the small angular sizes it is common to use the unit system of minutes and seconds of arc, also called arcminutes and arcseconds. One degree is divided into 60 arcminutes (am), while each arcminute is divided into 60 arcseconds (as). The angular diameter of both the Moon and the Sun is approximately half a degree, translating to about 30 am or 1800 as [16, 17], which makes their extension easily visible with the naked eye. The angular sizes of planets in the solar system are typically on the scale of multiple arcseconds. For Jupiter it is $30 - 50$ as [18], for Saturn $15 - 20$ as [19] and for Mars $4 - 26$ as [20]. These objects can be observed with the human eye using binoculars or low-cost amateur telescopes, and the planetary disks appear resolved.

Betelgeuse (α Ori), a massive and relatively close star, is amongst the stars with the largest apparent sizes. It has an angular diameter of around 50 mas[1] and appears to have about the same size as Pluto in its most distant orbital position (angular diameter = 60 mas [22]). This corresponds to the angular size of a 1 € coin at a distance of 84 km. Typical angular diameters of many bright stars are, however, on the order of only 1 mas. This relates to the coin being observed at a distance of around 5000 km - across the ocean from Europe to Northern America. Every star other than the Sun appears to the naked eye and to amateur telescopes as a point source, and resolving the stellar disks requires professional equipment and meter-scale telescope apertures. The physical reason for this is motivated in the next section.

2.2 Diffraction Limit

One might believe that the limit for image resolution is a technical one, such as the pixel density in the camera that is used for observation, which eventually limits the minimum angles of incident light that can be distinguished. However, the actual limit is a fundamental physical one, originating in the wave-like nature of light. A simple telescope may be reduced to a pinhole with an aperture of the telescope's opening diameter. Every plane wave incident on the telescope is being diffracted at the aperture. Hence the optical image of each inclination angle (the light from each angle can be interpreted as a "point source") in the focal plane is not point-like. Instead, an interference pattern shaped as an Airy disk (in case of a circular telescope aperture) is detected, as shown in figure 2.1.

If one considers an astrophysical object as the sum of infinitely many point sources, the received image is a superposition of Airy disks generated by every point source. Thus the obtained image becomes blurred and there is a limit on the angular resolution in the sky defined by the aperture of the instrument. To quantify this resolution one can ask the fundamental question of what is the minimal angle of two point sources (e.g. distant stars) that can be distinguished from each other in the telescope, which transfers to the question of when can the two superimposed Airy disks be separated into individual structures.

The common convention is written down in the Rayleigh criterion, as Lord Rayleigh concluded in 1879 [24]: if the first trough of one of the disks coincides with the maximum position of the other, the dip in between the two brightest spots decreases to 81% of the maximum

[1] Wilson et al. e.g. measured (57 ± 2) mas for the disk diameter at 546 nm [21]

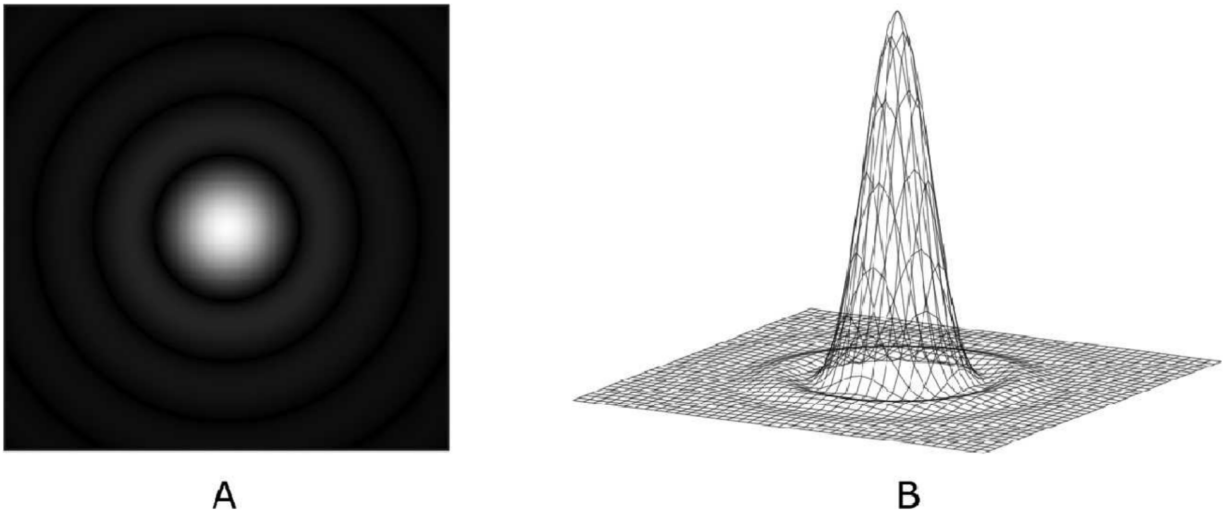

Figure 2.1: Airy disk interference pattern created by a circular aperture, top view (A) and side view (B). Image taken from [23].

intensity, and the identification of the maxima of both disks is still conveniently possible (see figure 2.2).

In a small angle approximation ($\sin\theta \approx \theta$) one finds the first minimum of an Airy disk at [24]

$$\theta = 1.2197 \cdot \frac{\lambda}{2R} \approx 1.22 \cdot \frac{\lambda}{D} \tag{2.1}$$

with λ being the observation wavelength, and $2R = D$ twice the radius, hence the diameter of the aperture. While a one-dimensional slit results in $\theta = \lambda/D$, the factor of 1.22 accounts for the two dimensional circular geometry of the (circular) aperture. The angle θ is identified as the angular separation of the objects in the focal length of the instrument, and is identical to the angular separation of the two objects in the sky.

The Rayleigh criterion serves as a suitable convention for defining the resolving power of an instrument with diameter D. It also enables asking the reverse question of how big a telescope needs to be to resolve two objects with an angular separation θ, or analogously to be able to resolve the disk of a planet/star with angular diameter θ, by rearranging equation 2.1

$$D_{\min} = 1.22 \cdot \frac{\lambda}{\theta} \tag{2.2}$$

For an exemplary wavelength of $\lambda = 500\,\text{nm}$ one finds, that the disks of the Sun and the Moon can be resolved with an aperture of 70 µm, while the planets mentioned in section 2.1 require telescope apertures of up to 0.4 cm for Jupiter, 0.8 cm for Saturn and 3.1 cm for Mars. These objects are at or above the resolution limit of the human eye, with a mean dark-adapted pupil diameter of about 0.69 cm [25].

The angular size of Betelgeuse translates to a minimum telescope aperture of

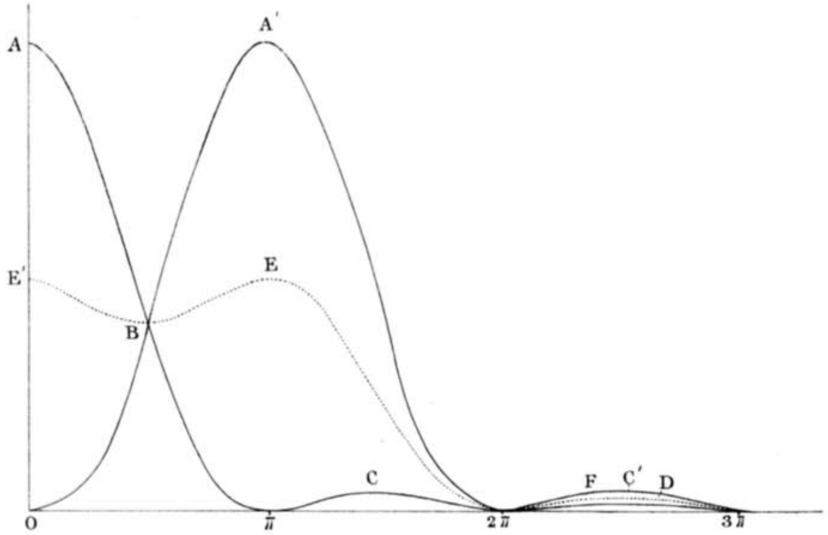

Figure 2.2: Rayleigh criterion: the position of the interference patterns of two point sources are aligned such that the maximum of one Airy disk falls into the first zero of the other (solid lines). The resulting superposition is shown as dashed line. Image adapted from [24].

$$D_{\min}(\lambda = 500\,\mathrm{nm}, \theta = 57\,\mathrm{as}) = 2.2\,\mathrm{m}. \tag{2.3}$$

Only a few stellar disks have been optically resolved. Figure 2.3, released in 1996, shows Betelgeuse photographed by the Hubble Space telescope, and is the first direct image of a stellar disk other than the Sun [26]. With a primary mirror diameter of 2.4 m [27] the telescope would just be able to resolve Betelgeuse's disk in the optical. The picture was taken in the ultra-violet (smaller λ), which further improves the image quality, and the angular diameter in UV was measured to be (125 ± 5) mas at a wavelength of 250 nm [26].

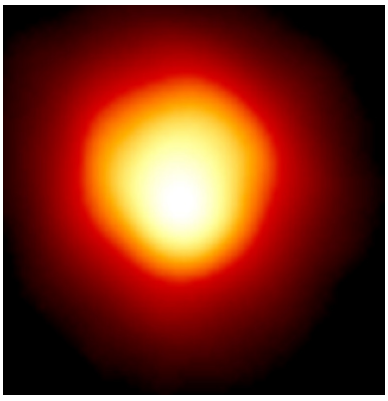

Figure 2.3: Ultra-voilet image of Betelgeuse taken with the Hubble Space Telescope. Image credit: Andrea Dupree (Harvard-Smithsonian CfA), Ronald Gilliland (STScI), NASA and ESA (adapted).

The diffraction limit directly leads to the quest for progressively larger telescopes for higher angular resolving powers. The currently largest optical telescopes have aperture diameters on the order of 10 meters, such as the *Large Binocular Telescope* in Arizona, which consists of two 8.4 m mirrors [28], or the *Gran Telescope Canarias* in La Palma, which has a single dish of 10.4 m diameter [29]. Larger telescopes are currently in the planning or construction phase. The biggest amongst these are the *Giant Magellan Telescope* (diameter of 25 m [30]), the *Thirty Meter Telescope* (diameter of 30 m [31]), and eventually the European Extremely Large Telescope (E-ELT), which is planned to feature an aperture of approximately 40 m [32]. According to equation 2.1 the E-ELT will provide an angular resolution of 3.1 mas, which is sufficient to resolve structures on the surface of the biggest stars.

However, there is a lot of exciting physics beyond the milli-arcsecond resolution limit. If one is able to resolve features below the size of stellar disks, such as substructures of even smaller stars and stellar systems, one becomes sensitive to measuring some stars being oblate due to their high rotational frequencies, seeing winds emerging from hot stars or studying stellar interactions in close binary systems [33]. Since larger telescopes are becoming increasingly expensive and complicated to assemble and operate, the highest angular resolutions are nowadays typically achieved with interferometric techniques between multiple telescopes rather than direct imaging with a single telescope. The concept of interferometric measurements and imaging is explained in the next section.

2.3 Michelson Interferometry and First Order Correlations of Light

On the one hand the fact that clear images are blurred by the diffraction of the starlight at the instrument's aperture is a disadvantage for astronomical imaging, but on the other hand also an evidence that there is more information in the light field than just the incidence angle of individual rays. Stable interference patterns require stable relations of the phases of the electromagnetic waves, and the spatial coherence of the light is a messenger about the original star's geometry. The appearance and disappearance of interference fringes under different measurement conditions can even be used to measure the angular sizes of stars, as was successfully performed by Michelson and Pease on Betelgeuse in 1920 [34].

2.3.1 The Michelson Stellar Interferometer

The measurement concept makes use of the physics of a classical double slit interferometry experiment, where two slits, separated by a distance d are illuminated by a coherent[2] light source, and the interference pattern is observed in the far field.

If the slits are infinitely small and there is a single plane wave incident on the slits, the interference pattern can be calculated interpreting both slits as emitters of spherical waves. Positions of maxima and minima of the interference pattern observed on a screen can be found via the relation

[2] light is called coherent if its wave-fronts arrive predictably. A quantitative description of coherence is given later on

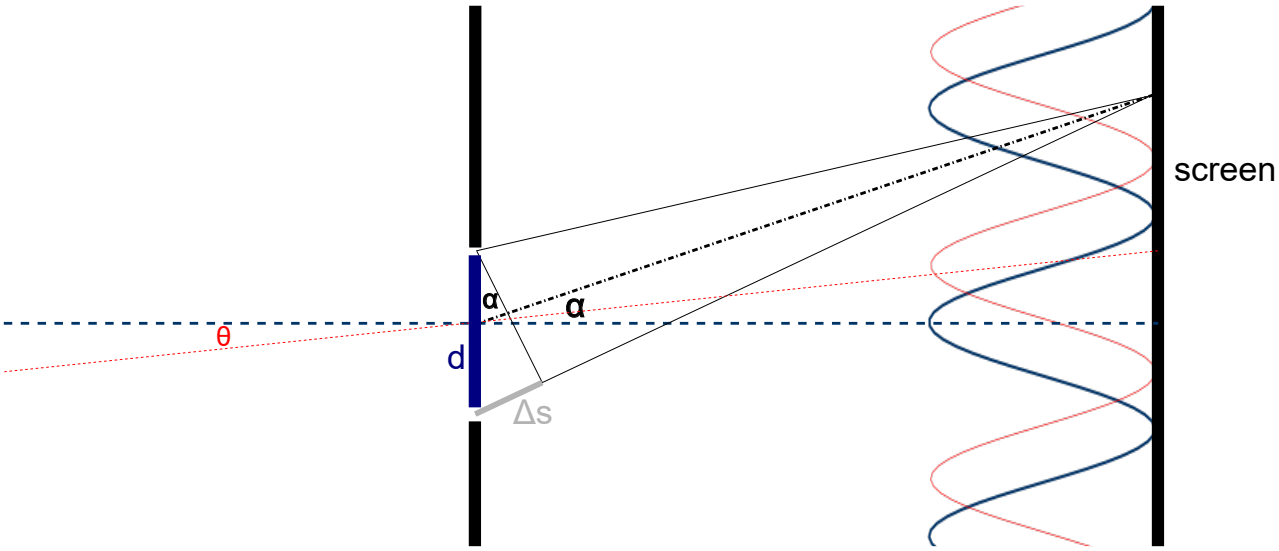

Figure 2.4: Schematic view of the double slit experiment with highlighted parameters explained in the text.

$$\alpha \approx \sin\alpha = \frac{\Delta s}{d}, \tag{2.4}$$

with $\Delta s = k \cdot \lambda, k \in \mathbb{N}_0$ for maxima, and $\Delta s = (k + \frac{1}{2}) \cdot \lambda, k \in \mathbb{N}_0$ for minima. Figure 2.4 shows the geometry in use. The interference pattern for perpendicular incidence is shown in dark blue. If the observed light source, however, is not point-like, but extended, all the incidence angles produce shifted interference patterns on the screen (e.g. light on an angle θ results in the pattern shown in red), resulting in a pattern that is a superposition of interference patterns of every incoming angle. If the angular size of the object θ is significantly smaller than the angular distance between the diffraction maxima of the single angles $\Delta\alpha = \lambda/d$, interference fringes are visible despite the angular extent of the source. In particular, this is true for small d, which favors large separations of the interference fringes. Thus, it becomes clear that by observing the interference fringes of the source at small slit separations, and then progressively increasing d results in a blurring of the interference fringes until they disappear, and once this slit separation is found one can draw back to the angular size of the source.

The idea of implementing this setup on a telescope was already suggested by Albert Michelson in 1890, who also provided the mathematical framework for the calculations of angular diameters: in case of a uniformly illuminated disk, the fringes disappear for the first time for [35]

$$d = 1.22 \cdot \frac{\lambda}{\theta}. \tag{2.5}$$

In his measurement of Betelgeuse in 1920 he found the fringes to disappear at $d = 3.065\,\mathrm{m}$ at a wavelength of $\lambda = 575\,\mathrm{nm}$, and determined the angular diameter to be $\theta_{\alpha\mathrm{Ori}} = 47\,\mathrm{mas}$ [36]. Figure 2.5 shows the interferometer, where two mirrors M_1 and M_4 served as the "slits".

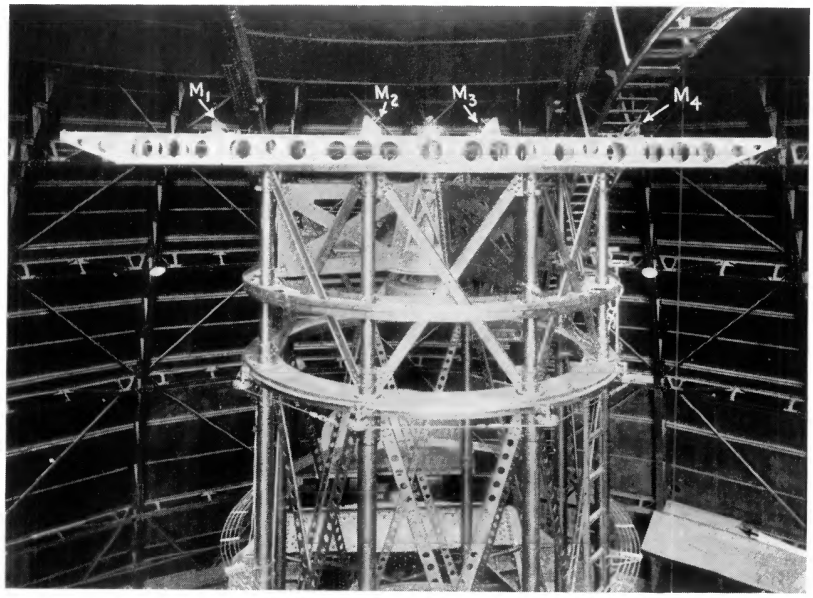

Figure 2.5: Michelson stellar interferometer. Taken from [34]

This proof of concept shows the benefit of interferometric measurements of angular diameters: while a traditional telescope would need to be 3 m in diameter to resolve the disk of Betelgeuse, each of Michelson's four used mirrors was only 15.2 cm in diameter [34]. The resolving power of this instrument can be defined by the necessity to observe the first disappearance of the interference fringes at

$$\theta_{\min} = 1.22 \cdot \frac{\lambda}{d_{\max}}. \tag{2.6}$$

It is apparent that the resolving power is unaffected by the sizes of the individual mirrors, but instead only depends on the maximum separation between the light collecting mirrors. And it is easy to argue that the realization of large separated mirrors observing the same source is simpler and more cost-effective than the construction of huge telescope mirrors. The concept of stellar interferometry can be expanded from one telescope mount to multiple separated telescopes, as long as it is ensured that the light is combined at the necessary precision.

The downside of an interferometer is, however, that it has only access to a fraction of the information compared to a direct-imaging telescope with a single dish of the size of the maximum separation of the interferometer. While the imaging telescope produces a two-dimensional gapless image of the object, the two-slit interferometer only measures one-dimensional parameters, such as the angular diameter of a star. In the following section it will however also be motivated, how interferometry, especially when performed with arrays of telescopes, is able to create dense information maps and by that reconstruct two-dimensional images.

2.3.2 Temporal and Spatial Coherence of Light

To find permanent interference fringes it is required that the electromagnetic waves obey constant phase relations at the positions where the light is collected (the telescopes). For a monochromatic point source at a quasi-infinite distance, one receives a plane wavefront

and the mutual consistency of the phases of the electromagnetic wave between the telescopes is obvious. The light field is called fully coherent. In case of an extended source which in addition is also emitting light with more than one frequency, the degree of spatial and temporal coherence at the observer can be questioned. Especially when the source - considering a star - is assumed to be incoherent in the sense that the individual light emitters (atoms) do not obey temporal or spatial phase relations amongst each other, but rather emit electromagnetic radiation independently.

Coherence as indicator of the phase-stability of light can be defined in time, quantifying how well the state of a wave at a time $t + \tau$ can be predicted, if the state at time t is known at the same position. It, however, can also be defined in space, quantifying how well the state of a wave at a position $\vec{r} + \vec{\rho}$ can be predicted, if the state at the position $\vec{r}$ is known at the same time. The first aspect relates to temporal coherence and can be expressed via the coherence time τ_c. If $\vec{\rho}$ points into the direction of light propagation, the second aspect is also related to temporal coherence, and can be expressed via the coherence length $L_c = c\tau_c$. [37]

If $\vec{\rho}$ is aligned perpendicular to the light propagation direction, the spatial coherence is observed, and one can define a coherence cell b_c in which light can be called spatially coherent.

The mutual degree of coherence of the wave-field at two points $(\vec{r_1}, t_1)$ and $(\vec{r_2}, t_2)$ in time and space can be quantified with the help of the first order correlation function [38]:

$$g^{(1)}(\vec{r_1}, t_1, \vec{r_2}, t_2) = \frac{\langle E^*(\vec{r_1}, t_1) E(\vec{r_2}, t_2) \rangle}{\sqrt{\langle |E(\vec{r_1}, t_1)|^2 \rangle \langle |E(\vec{r_2}, t_2)|^2 \rangle}}, \tag{2.7}$$

where E is the electric field and the bracket notation $\langle\rangle$ denotes time-averaging. If the distance between the observers is much smaller than the distance from the observers to the source, the time-averaged light intensities $\langle |E(\vec{r_1}, t_1)|^2 \rangle = \langle |E(\vec{r_2}, t_2)|^2 \rangle = \langle |E|^2 \rangle) = I$ can be approximated to be equal, and equation 2.7 simplifies to

$$g^{(1)}(\vec{r}, t, \vec{\rho}, \tau) = \frac{\langle E^*(\vec{r}, t) E(\vec{r} + \vec{\rho}, t + \tau) \rangle}{I} \tag{2.8}$$

setting $\vec{r_1} = \vec{r}$ and $\vec{\rho} = \vec{r_2} - \vec{r_1}$, and analogously $t_1 = t$ and $\tau = t_2 - t_1$. In many cases the choice of the absolute position and time is arbitrary, and $g^{(1)}$ is only dependent on $\vec{\rho}$ and τ.

Spatial correlations

The fact that the light field of a spatially extended source, which is emitting incoherent light, can show (partial) coherence has been shown in Michelson's stellar interferometer. He observed that the light from a star is spatially coherent over a certain distance $|\vec{\rho}|$, which increases with decreasing angular size of the star. The appearance of spatial coherence may seem surprising in this situation, but there is an intuitive approach to understanding this: consider observing the Sun, a very close and therefore visibly extended star. It does not show "everyday" interference effects, and thus the light is not coherent[3]. However, considering the same star now being at infinite distance, it appears as a point source and will thus show full spatial coherence. The transition between these two regimes directly leads to the observation in Michelson's

[3] following equation 2.5 it actually is coherent on the scale of µm

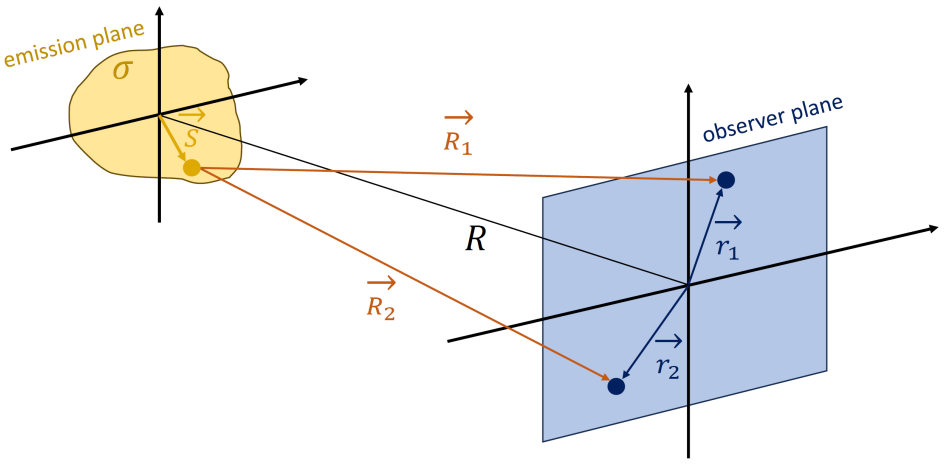

Figure 2.6: Geometry of the van Cittert-Zernike theorem. This figure is inspired by Fig. 10.3. in [41]

interferometer - the increasing degree of spatial coherence with decreasing angular size of the observed object. For simplicity, the Sun is assumed to be monochromatic in this example. Effects of extended optical bandwidths are neglected here, but discussed later on.

The mathematical framework, generalized to an arbitrary shape of the source, has been developed by van Cittert (1934) [39] and Zernike (1938) [40]. They found that the degree of spatial coherence between two observers can be described by the amplitude of a (virtual) diffraction pattern of the source, that one sees when the pattern is centered around the other observer [40]. Figure 2.6 shows the geometry used in the following situation. If the light emission area is denoted by σ, and $\vec{S}$ is a point in the plane of that area, the spatial dependency of the $g^{(1)}$ function in the observer plane can be linked to the intensity profile $I(\vec{S})$ of the source (per unit area) via a Fourier transform [41]:

$$g^{(1)}(\vec{r}_1, \vec{r}_2) = \frac{1}{\sqrt{I_1 I_2}} \int_\sigma I(\vec{S}) \frac{e^{i\vec{k}(\vec{R}_1 - \vec{R}_2)}}{\vec{R}_1 \vec{R}_2} d\vec{S}, \tag{2.9}$$

where $\vec{R}_{1,2} = \vec{r}_{1,2} - \vec{S}$ are the distance vectors between the observer positions and the points in the emission plane, and $I_{1,2} = \int_\sigma \frac{I(\vec{S})}{|\vec{R}_{1,2}|^2} d\vec{S}$ are the intensities at the observer positions. For astronomical observations, where the distance R between the observers (telescopes) and the source (e.g a distant star) is orders of magnitude larger than the distance between the observers themselves or the extent of the source, one can simplify $\vec{R}_1 \vec{R}_2 \approx R^2$ and $I_1 = I_2 \approx \frac{1}{R^2} \int_\sigma I(\vec{S}) d\vec{S}$. Equation 2.9 becomes

$$g^{(1)}(\vec{r}_1, \vec{r}_2) = \frac{\int_\sigma I(\vec{S}) e^{i\vec{k}(\vec{R}_1 - \vec{R}_2)} d\vec{S}}{\int_\sigma I(\vec{S}) d\vec{S}}. \tag{2.10}$$

With this relation, the *van Cittert-Zernike theorem*, the degree of spatial coherence produced by a light source of arbitrary shape and intensity profile can be computed for any separation of two observers. In the scope of measurements of a single star, whose intensity profile is assumed

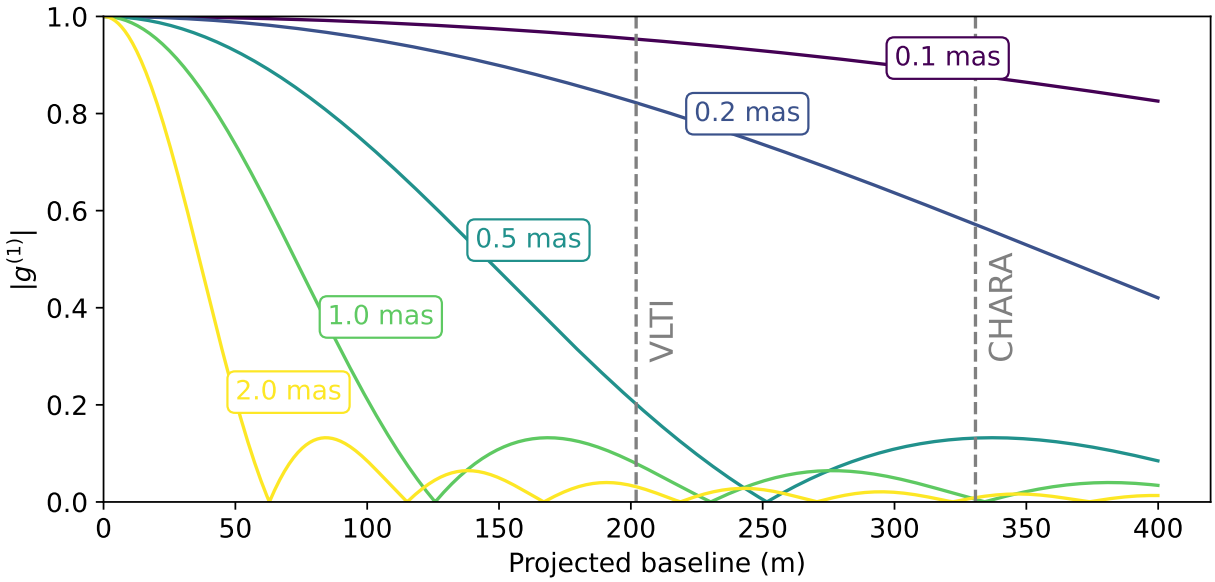

Figure 2.7: Spatial degree of coherence that can be observed with amplitude interferometers at $\lambda = 500\,\text{nm}$. The grey lines denote the maximum baseline between telescopes of the currently operating VLTI [44] and CHARA [45] arrays.

to be constant within its diameter (the so-called *uniform disk* model), the spatial degree of coherence, calculated by the Fourier transform of the star's sphere, appears to be the equal to a two-dimensional representation of a sinc function [42]:

$$g^{(1)}(\vec{r}_1, \vec{r}_2) = \frac{2J_1(\pi b\Theta/\lambda)}{\pi b\Theta/\lambda} \tag{2.11}$$

where J_1 is the Bessel function of the first kind, and $b = |\vec{\rho}| = |\vec{r_2} - \vec{r}_1|$ is the projected baseline between the two observers. The radially symmetric source profile translates to an also radially symmetric spatial coherence map, which allows to plot it in one dimension without loss of information. In case of a fixed observation wavelength and angular size of the star, the distance between the observers is the only free parameter affecting the degree of coherence. In figure 2.7 the absolute of the $g^{(1)}$ function, which is actually the observable quantity and relates to the clearness, or *visibility*, of the interference fringes[4], is plotted versus the projected baseline for different angular diameters of the star at a wavelength of 500 nm.

If the requirement for resolving the star is set by the ability to measure the first minimum of the spatial degree of coherence, which lies at $b_c = 1.22\lambda/\theta$, one again finds the familiar relation from equation 2.6. Looking at figure 2.7 one may define the baseline region up to the first zero as *coherence cell* b_c. In case the interferometer is sensitive to quantitatively determine the degree of coherence, rather than just observe whether or not the fringes are visible, it does not necessarily need to measure the spatial coherence curve up to the border of the coherence cell to determine the angular diameter, and the strict limit of equation 2.6 is softened.

[4]In traditional interferometry literature the *visibility* V is defined quantitatively, but this concept is not introduced in this work. It turns out that for equal wave amplitudes at the interfering points, $|g^{(1)}|$ is equal to V [43].

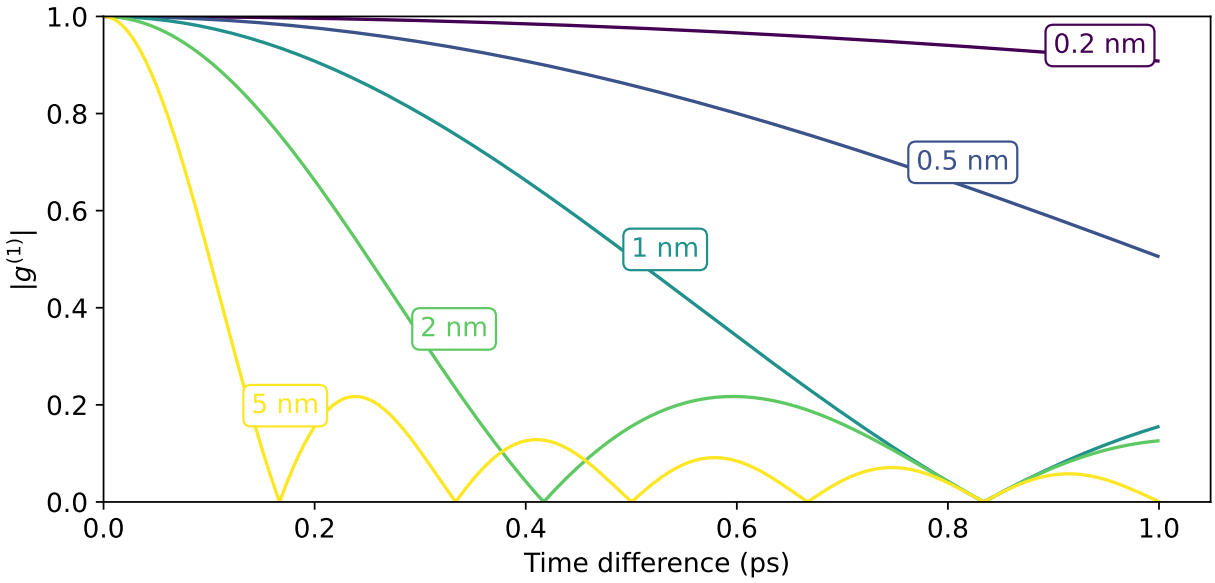

Figure 2.8: Temporal degree of coherence that can be observed with amplitude interferometers at $\lambda = 500\,\text{nm}$ for different optical bandwidths.

Temporal coherence

The above calculations are performed for the case of a single wavelength. When the emission profile of the source is not a single sharp emission line, but broad, the different wavelengths interfere. Analogously to the spatial extent of the source decreasing spatial coherence $g^{(1)}(\vec{\rho})$, its extent in optical bandwidth decreases temporal coherence $g^{(1)}(\tau)$: consider the self-coherence of a point ($\vec{\rho} = 0$), which is therefore fully spatially coherent. The wave-field will show irregular and unpredictable variations of amplitude and phase in time, where its predictability is limited to a characteristic time scale inverse proportional to the spectral bandwidth of the source.

Similarly to the van Cittert-Zernike theorem, the quantitative relation between the frequency spectrum $s(\omega)$ (the *power spectrum*) and the temporal $g^{(1)}$ function can be found via a Fourier transform, and is written down in the *Wiener–Khinchin theorem* [46], which reads [47]:

$$g^{(1)}(\tau) = \int_{-\infty}^{+\infty} s(\omega) e^{-i\omega\tau} d\omega \tag{2.12}$$

This equation emphasizes the symmetry between the relations of spatial coherence and source geometry, and temporal coherence and the source's emission spectrum. So analogously to figure 2.7 one can observe the decay in temporal coherence and draw back to the emission profile of the source. For a rectangular power spectrum around ω_0 with width $\Delta\omega$ one finds, transitioning to the frequency regime [48]

$$g^{(1)}(\tau) = e^{-i\frac{2\pi c}{\lambda_0}} \operatorname{sinc}\left(\frac{\tau \Delta\lambda \pi c}{\lambda_0^2}\right). \tag{2.13}$$

The observable $|g^{(1)}|$ is visualized in figure 2.8 for different optical bandwidths, which all however are very small compared to the bandwidths of stars.

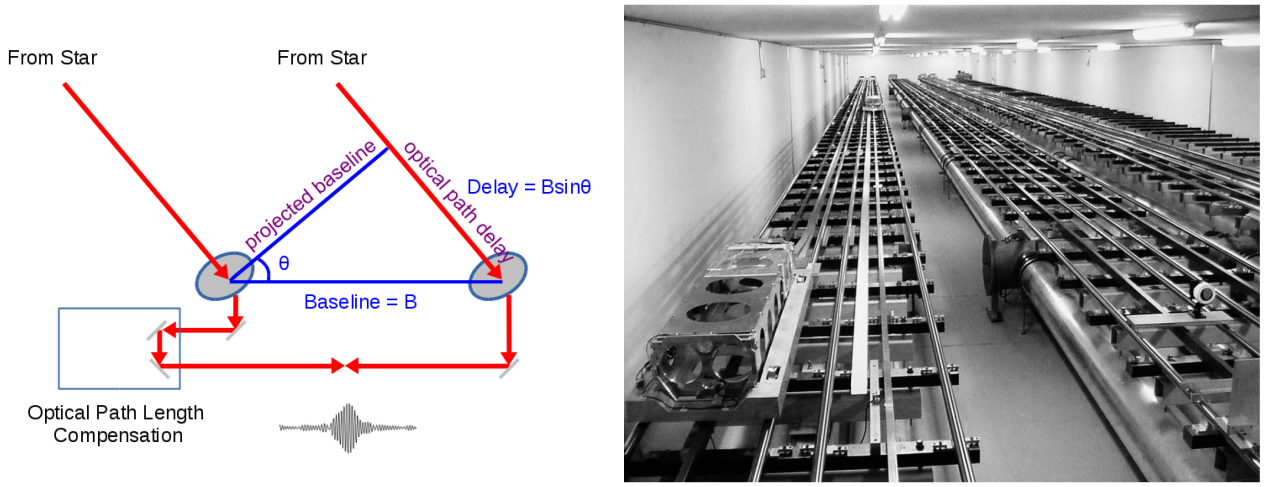

Figure 2.9: Left: geometry for two-telescope interferometry. The image is adapted from [49] with the violet text added. Right: delay lines for optical path length compensation for the CHARA array. Taken from [50].

Just as the coherence cell can be defined for the spatial coherence, one can define the time up to the first zero as *coherence time* τ_c, and one finds[5]

$$\tau_c = \frac{\lambda_0^2}{c\Delta\lambda}. \tag{2.14}$$

This equation is very popular for describing temporal coherence in literature, and even though it precisely describes the decrease to the first zero of the temporal degree of coherence only in the specific case of a rectangular optical bandpass, it is widely used as an approximation for the time range in which temporal coherence can be observed.

The symmetry between spatial and temporal coherence is broken when the observer is interested in the spatial geometry of the source, but not in its intrinsic emission profile, which happens to be more often the case than the other way around, just like in this work. In this case, the temporal coherence is not used as a source of information, but nevertheless needs to be taken into account. To measure $g^{(1)}(\vec{\rho}, \tau)$ a certain degree of temporal coherence is required, in order to observe the change in the spatial dimension. The effect of temporal coherence is further described in section 2.3.3.

2.3.3 Modern Amplitude Interferometers and Their Limitations

The concept of the Michelson interferometer is nowadays one of the most common instruments in high angular resolution astronomy. Its technique of interfering the amplitudes of the electromagnetic waves is commonly called *amplitude interferometry*, and extended to multiple telescopes operating in arrays. For the case that the interferometer consists not only of a single telescope mount, but different telescopes are being used, the physics of the Michelson interferometer remains unaffected, except for taking a more complex instrument geometry into account.

[5]There are other general approaches of defining the coherence time which also lead to the same equation, such as simply defining $\tau_c = 1/\Delta\nu$, where $\nu = \omega/2\pi$

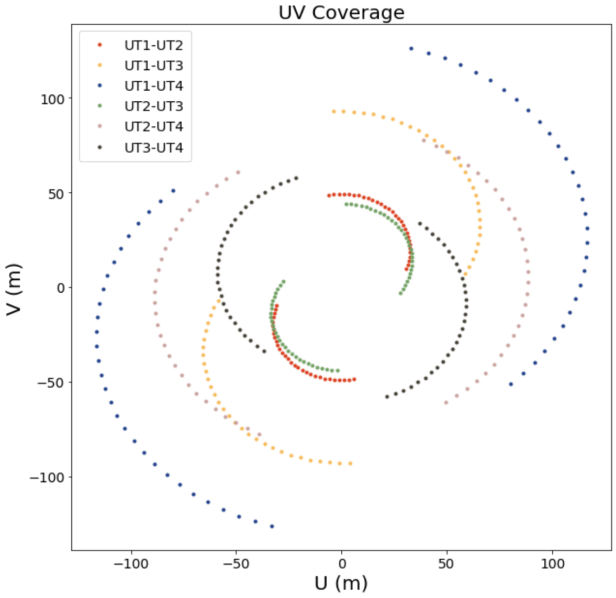

Figure 2.10: Exemplary UV plane coverage of the utility telescopes of the *Very Large Telescope Interferometer*. Image taken from [52].

Figure 2.9 (left) shows the following situation: while the two telescopes are separated by the "absolute" baseline B, the effective separation as seen from the source is different and changes over time while the telescopes are tracking the target. This effective separation, which matches the definition of $|\vec{\rho}|$ in this thesis, is often called *projected baseline*, even though it may also be just called *baseline* and should not be confused with the actual separation of the telescopes. The second aspect to consider is the *optical path delay*, meaning the star's wavefront arrives at the left telescope in Figure 2.9 (left) first, and has to travel an additional distance to reach the other (right) telescope. Since the light from the two telescopes needs to be interfered in phase, this path delay has to be compensated for continuously by adding additional delay lines to the light path of the left telescope before combining them. This is usually done in long halls where the light is reflected by mirrors that are driven on rails to precisely adjust the path delay compensation. Figure 2.9 (right) shows the path delay compensation hall of the CHARA (Center for High Angular Resolution Astronomy) interferometer [50].

In an array of telescopes, every combination of two telescopes can be considered for interferometric observations. The resulting available baselines not only span over different ranges, but also in different directions enabling a two-dimensional analysis of the source. The usual description of the imaging power of an interferometer is given by the concept of the the *uv-plane* coverage. It makes use of a new coordinate system, defined not by the absolute positions of the telescopes, but by the (relative) projected baselines between them, often related to as *spatial frequencies* [51]. The plane is perpendicular to the direction of the source [52].

In figure 2.10 an example of a uv-plane is shown, where the four Utility Telescopes of the *Very Large Telescope Interferometer* (VLTI) observe an arbitrary target. Each telescope combination adds a point in the uv-plane for each point in time. While time progresses, not only do the values of the projected baselines change, but also their orientation, so that each

telescope combination begins to form elliptical curves in the uv-plane, which would complete after a 24 hour run, if daylight observations were possible.

For radially symmetrical targets, as one assumes many stars to be, the change in orientation of the baselines is not of importance and the uv-plane representation simplifies to the one-dimensional spatial coherence curves, with the one-dimensional baseline $b = |\vec{\rho}| = \sqrt{u^2 + v^2}$.

A short note on image reconstruction

The common thread running through this thesis revolves around the question of how to measure the angular size of an astronomical object. In the one-dimensional example of the uniform stellar disk model in equation 2.11 and figure 2.7, the angular diameter is determined by measuring the first zero b_c of the $|g^{(1)}|$ curve and calculating $\theta = 1.22\lambda/b_c$. However, in general, an interferometer is able to extract significantly more information from the measured b or u-v visibility curves. If not only the first zero, but the shape of $|g^{(1)}|$ is measured, one gets additional information about the structure of the source. In case the shape aligns with equation 2.11, the source can be modeled to be spherical with uniform brightness. Even though more realistic models, such as limb-darkening [42, 53], result in only slightly different shapes of the spatial coherence curve, precise measurements allow the detection of these differences.

The mathematical depiction of how to return to the source geometry from $g^{(1)}$ is envisioned by solving equation 2.9 for $I(\vec{S})$, which is essentially a reverse Fourier transform. This concept is expandable to two dimensions, and so in principle an image can be constructed from the one or two dimensional spatial coherence data, as long as the b or u-v coverage is sufficiently high. Such techniques will not be discussed further in this work, but can be studied in the literature in more detail (e.g. [54, 55]).

Implications of temporal coherence for the amplitude interferometer

Crucial for the appearance of interference fringes in the interferometer is the ability to interfere the two light waves from the telescopes with a high accuracy. The degree of temporal coherence is directly connected to the necessary precision of equalizing the path length of the light beams from the different telescopes. To make this connection clear it is important to ask which precision of the optical path delay compensation is necessary to observe interference fringes. One might first suspect that the precision must be close to a small fraction of the observed wavelength, in order to interfere the light in phase. However, this is not necessarily true, as interference can also occur between different wave-fronts. A stable interference pattern is visible, as long as the incoming wave-fronts from both telescopes continue to arrive coincidentally over the entire exposure time of the detector. This would always be true for perfectly monochromatic light, but becomes more and more inaccurate the broader the wavelength spectrum gets, due to the superpositions of all the wavelengths in the spectrum. This behaviour is described by the temporal coherence function $g^{(1)}(\tau)$, and in particular by the coherence time τ_c, which expresses the time range in which the wave-fronts arrive in a predictable manner. The coherence time can be translated to the coherence length $l_c = c\tau_c$, to understand within which spatial range along the propagation direction of the light interference can be observed, which eventually defines the necessary precision of the interferometer's optical path delay compensation.

As a quantitative example consider an optical filter centered around $\lambda_0 = 500\,\text{nm}$ with a bandwidth of $\Delta\lambda = 1\,\text{nm}$. According to equation 2.14, one obtains $\tau_c = 0.83\,\text{ps}$, and consequently $l_c = 250\,\mu\text{m}$. While there is no doubt that even this precision is a major technical challenge, the error budget of the interferometer with respect to the path delay compensation does not come down to the sub-wavelength precision, as long as narrow-band optical filtering is ensured.

Technical limitations by the influence of atmospheric turbulence

The technical challenges of the optical path delay compensation with its necessary precision are one factor that limits an interferometer's maximum baseline which could be realized. Another aspect are imperfect atmospheric conditions. Turbulent atmosphere (*seeing*) can directly induce relative phase shifts of the wave-fronts at the different telescopes as well as vary the propagation path of the light through the atmosphere [56], which results in the same effect. It is easy to understand that the interferometric measurement suffers from this, as constant relative phase variations decrease the fringe visibility.

In this context, two quantities are commonly used for describing the atmospheric quality and its implications on the interferometer: the *Fried length* r_0, describing over which spatial range phase fluctuations are small transversal to the propagation direction of the light, and the *atmospheric coherence time* τ_0, characterizing the time interval in which such phase fluctuations occur. r_0 primarily limits the aperture size of each telescope, while τ_0 limits the integration time for coherent observations. [57] Both limitations result in the reduction of the number of collected photons during one integration time by orders of magnitude, compared to conventional telescopes [58]. Therefore, observations are restricted to bright targets with maximum apparent magnitudes of 5 to 7 in the optical [59]. Even though adaptive optic techniques, which correct the wave-fronts usually with the help of tip-tilt mechanical mirror formations [60, 61, 62], have been developed, the operational practicability of optical amplitude interferometers seems to approach a baseline limit with $b_{\text{max}} \lesssim 500\,\text{m}$. The *Navy Precision Optical Interferometer* is constructing the world's longest baseline for optical interferometry of 432 m [63].[6]

2.4 Intensity Interferometry and Second Order Correlations of Light

It is quite remarkable that, even though the concept of measuring angular diameters of stars via amplitude interferometry was already proven with the Michelson stellar interferometer in 1920, not much progress in this field has been made in subsequent years and decades. While the consecutive work from the 20 feet Michelson interferometer resulted in a 50 feet interferometer in 1930 [66], it took until the early 1970s for developments of successful amplitude interferometers to be reported [67].

[6] As the *Event Horizon Telescope* keeps demonstrating, interferometry with radio wavelengths can work with baselines spanning the entire globe, however without the need to analogously combine the wave-fronts from the different telescopes [64, 65].

Instead, a new technique for measuring angular sizes of astronomical objects in a very similar manner, but with some crucial differences, appeared in the early 1950s. The pioneers of this work, Robert Hanbury Brown and Richard Q. Twiss, initially thought of their method, at a later stage called *intensity interferometry*, as a suitable application for radio interferometry [13]. Instead of optically interfering the amplitudes of the radio waves, their individual signals were recorded by superheterodyne receivers, upon which the signals were correlated electronically. Hanbury Brown and Twiss indeed were able to measure the angular extents of the two radio sources in Cygnus and Cassiopeia using baselines of up to four kilometers. [68]

While these baselines were not implausible to realize for conventional interferometry at radio wavelengths, which arguably made their specific experiment less revolutionary, they realized during operation of the interferometer that it was easily working even through a turbulent atmosphere. Hence they developed an intensity interferometer for optical wavelengths, resulting in the famous *Narrabri Stellar Intensity Interferometer*, which is described in more detail in section 2.4.2. [13]

But first, the questions how this technique physically works, even at optical wavelengths, and why this new idea overcomes the issue of atmospheric turbulence, are discussed in section 2.4.1.

2.4.1 Second-Order Coherence Theory of Light

As mentioned before, the difference between ”conventional” interferometry and Hanbury Brown and Twiss-like interferometry lies in the fact that latter is not actually optically interfering the wave-fronts of the electromagnetic waves. Instead, it already transfers the optical into electrical signals at the stage of the telescopes. Therefore, one needs to account for the collapse of the wave-light nature of the light field into the detection of photons, even before the information from the different telescopes is combined. Meaning, light *intensities* are correlated, instead of *amplitudes*.

As Hanbury Brown points out in his book in 1974 ([13]), there is an intuitive understanding of intensity correlations at radio wavelengths: the energies of single radio photons are so small and there are so many of them, that a single photon only contributes a small fraction to the amplitude of the electromagnetic wave. Fluctuations in the amplitude, as subject of observation in classical interferometry, can therefore be connected directly to fluctuations on the number of photons. In case of optical light however, this analogy is violated by the fact that single photons carry much more energy, and the idea that intensity fluctuations in both detectors are correlated is much more counter-intuitive. [13]

In fact, there was a controversy at that time [69] about the quantitative theory that Hanbury Brown and Twiss published [70]. But they could deliver experimental evidence as they detected the predicted photon correlations between two photo-multipliers that observed light from a mercury arc lamp [71].

Figure 2.11 (left) shows their setup. The two photo-multipliers are arranged in two arms behind a beamsplitter (semi-transparent mirror), where the position of one photo-multiplier can be altered precisely in order to create an effective separation between both detectors. The

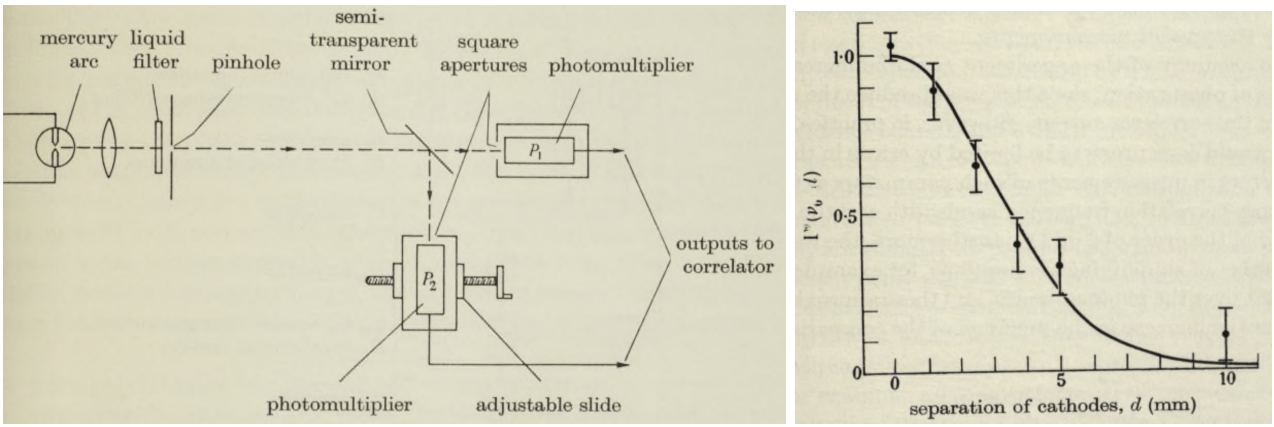

Figure 2.11: Left: experimental setup for the measurement of photon correlations by Hanbury Brown and Twiss. Right: the resulting correlation strength for different effective separations of the photo-multipliers. Both images are taken from [71].

results can be found in figure 2.11 (right), where the photon correlation is plotted versus the effective separation of the photo-cathodes, and the solid line represents the theory curve. Hanbury Brown and Twiss not only showed that they were able to measure the correlation in intensity (number of photons) fluctuations, but also the decrease of the signal strength with increasing "baseline", very analogously to the measurement of the degree of coherence in amplitude interferometry. It is worth to point out that Hanbury Brown and Twiss not only developed a new detector concept for astronomical interferometry, but also provided the theoretical calculations, which opened up a new research field in quantum optics that has expanded to applications in various other fields of physics, where this experiment is still referred to as *Hanbury Brown-Twiss (HBT) experiment*, and the effect of photon correlations is called *HBT effect*.

The second-order correlation function

The quantitative description of the HBT effect can be done equivalently to introducing the first order correlation function $g^{(1)}$ in section 2.3.2, now introducing the second order correlation function between two observers at positions $\vec{r}_1$ and $\vec{r}_2$ observing at times t_1 and t_2 [38, 72]:

$$g^{(2)}(\vec{r}_1, t_1, \vec{r}_2, t_2) = \frac{\langle E^*(\vec{r}_1, t_1) E^*(\vec{r}_2, t_2) E(\vec{r}_2, t_2) E(\vec{r}_1, t_1) \rangle}{\langle E^*(\vec{r}_1, t_1) E(\vec{r}_1, t_1) \rangle \langle E^*(\vec{r}_2, t_2) E(\vec{r}_2, t_2) \rangle}, \tag{2.15}$$

which can be rewritten using $E^*(\vec{r}_i, t_i) E(\vec{r}_i, t_i) = I(\vec{r}_i, t_i)$. Further one can again introduce the relative positions in space $\vec{\rho}$ and time τ:

$$g^{(2)}(\vec{r}, t, \vec{\rho}, \tau) = \frac{\langle I(\vec{r}, t) I(\vec{r} + \vec{\rho}, t + \tau) \rangle}{\langle I(\vec{r}, t) \rangle \langle I(\vec{r} + \vec{\rho}, t + \tau) \rangle} \tag{2.16}$$

A general observation is, that compared to the first-order coherence, the second-order coherence is sensitive to instantaneous intensities of light. These relate to the number of photons at a time, but not to the phase of the electromagnetic wave. While this phase-insensitivity is the key for why atmospheric turbulences do not influence the $g^{(2)}$ measurements significantly, the question remains why it is still possible to extract information about the source geometry.

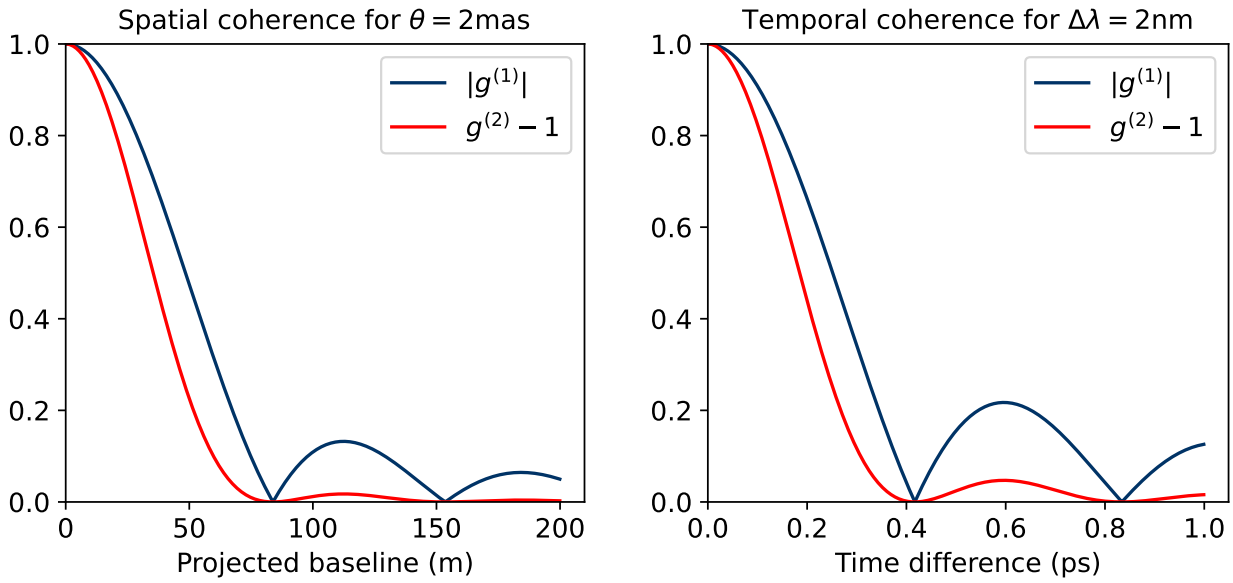

Figure 2.12: Left: spatial coherence for a source of angular diameter of $\theta = 2\,\text{mas}$. Right: temporal coherence for an optical bandwidth of $\Delta\lambda = 2\,\text{nm}$

Connections between first-order and second-order coherence

The answer lies in a link between $g^{(1)}$ and $g^{(2)}$, which can be found for the case of *chaotic light*. That means that the light is emitted by independent atoms, which show both *collision broadening* and *Doppler broadening* in their frequency spectra. Collision broadening means that the atom's radiation randomly changes the phase once a collision between two atoms occurs. Doppler broadening is related to the broadening of the frequency spectra due to the movement of the atoms in the gas either towards or away from the observer. [73]

For calculating $g^{(2)}$ one can write the electric field at the observer as the sum of the electric fields from all emitting atoms, $E(t) = \sum_i E_i(t)$, which can be inserted into equation 2.15. The calculation is performed in Loudon (2000), p.110 [73], where the arising time averages over electric fields from mixing atoms vanish due to their random relative phases. Eventually, for a large number of atoms, one finds the simple relation

$$g^{(2)}(\tau) = 1 + |g^{(1)}(\tau)|^2. \tag{2.17}$$

This equation is called *Siegert relation* [74], and is true for all thermal and chaotic light sources, but not for other sources of light, such as lasers, where the mixing terms in the derivation of this equation do not vanish. For stars and other typical astronomical objects, however, the thermal light character is valid and equation 2.17 can be applied. This simple equation is visualized in figure 2.12 for both the spatial (left) and temporal (right) coherence, and demonstrates the close conceptual similarity between measuring first- or second-order coherence between different baselines and extracting the angular diameter from the visibility curve.

Interpretation of second-order coherence

Note that the red curve in figure 2.12 shows $g^{(2)} - 1$, so the actual $g^{(2)}$ values distribute between $g^{(2)}(\tau = 0, \vec{\rho} = 0) = 2$ for small time differences and baselines, and $g^{(2)}(\tau \to \infty, |\vec{\rho}| \to \infty) = 1$ for big time differences or large baselines. A physical interpretation of different values for $g^{(2)}$ is possible when rewriting equation 2.16. Expressing the instantaneous intensity by the fluctuation around the mean, $I(t) = \langle I(t) \rangle + \Delta I(t)$, one finds (for simplicity assuming equal average intensities in both detectors)

$$g^{(2)}(\vec{r}, t, \vec{\rho}, \tau) = 1 + \frac{\langle \Delta I(\vec{r}, t) \Delta I(\vec{r} + \vec{\rho}, t + \tau) \rangle}{\langle I \rangle^2}. \tag{2.18}$$

In the case of large baselines and time differences, $g^{(2)} = 1$ and thus

$$\langle \Delta I(\vec{r}, t) \Delta I(\vec{r} + \vec{\rho}, t + \tau) \rangle = 0, \tag{2.19}$$

which means that the time average over the product of intensity fluctuations in both detectors vanishes. In other words: the intensity fluctuations in both detectors are statistically uncorrelated. However, for small baselines $|\vec{\rho}|$ and time differences τ one finds $g^{(2)} > 1$ and, therefore, a positive remainder in the product of intensity fluctuations. This in fact means that the intensities are correlated in both detectors. If one detector measures a positive fluctuation, the other one is likely to measure the same.

This effect can be broken down to the level of individual photons. Consider e.g. very low photon rates in the detectors. The positive correlation of intensities means that if one detector measures a photon, there is an increased probability that there is a coincident photon measured by the other detector. This observation, the fact that photons from chaotic light sources tend to arrive in pairs, or, more generally speaking, in bunches, rather than randomly distributed, is the famous Hanbury Brown-Twiss effect, and is also called *photon bunching* [75]. The appearance of photons arriving preferentially in pairs, even though emitted completely randomly and independently at the source, lacks of intuition, and was a major part of the aforementioned controversy about the theory [13].

It should be noted that mathematically the time-averaged product of the intensity fluctuations can be < 0, and consequently $g^{(2)} < 1$, if the intensities at the detectors anti-correlate. According to equation 2.17, this will never be the case for thermal light, as the absolute is positive by definition, but can actually be realized e.g. in single photon sources, such as a single atom. The emission of a photon prevents an immediate second photon of being emitted. In a beamsplitter arrangement with a photo-detector in each arm, this results in the photon being detected in one detector, but certainly there is no coincident photon in the other arm. This effect is called anti-bunching [75], and is a clear signature of quantum mechanics [37].

Implications of temporal coherence for the intensity interferometer

Just like for the amplitude interferometer, the valuable information lies in the spatial coherence, but temporal coherence is also of importance. For amplitude interferometry a lack of temporal coherence complicates the measurements in terms of the necessary spatial precision of interfering the light, and limits the exposure times as well as the aperture sizes (latter

due to the atmospheric coherence time). As already discussed, atmospheric turbulence does not hinder intensity interferometry, and neither are the requirements for spatial precision as strict as for amplitude interferometers, since the phases of the electromagnetic waves are not measured. Instead, the measurand is the number of coincident photons (with the term "coincident" referring not only to $\tau = 0$, but rather $\tau \lesssim \tau_c$) relative to the absolute photon stream.

If one takes the same example with a bandwidth of $\Delta\lambda = 1\,\text{nm}$ centered around $\lambda_0 = 500\,\text{nm}$, the coherence time is $\tau_c = 0.83\,\text{ps}$. The physical meaning is that correlated photons effectively only appear within that time frame. As commercial photo-detectors have time resolutions typically on the order of $\tau_e = 1\,\text{ns}$, it is impossible for a realistic astronomical intensity interferometer to measure the shape of the temporal $g^{(2)}$ function as depicted in figure 2.12 (right). Instead, if the time binning of the measurement is set approximately equal to the time resolution of the detectors, the whole photon bunching signal will be contained within the single central time bin around $\tau = 0$. However, this time bin also contains a factor of τ_e/τ_c more uncorrelated photon pairs. The height of the correlation signal will therefore decrease from $g^{(2)}(\tau = 0) = 2$ to

$$g^{(2)}(\tau = 0) \approx 1 + \frac{\tau_c}{\tau_e} \approx 1.001. \tag{2.20}$$

Further reductions are caused if the light is not polarized or by spatial coherence losses if $|\vec{\rho}| \neq 0$. While a detailed quantitative description will be given in section 3.4, this simple consideration points out one major challenge of an intensity interferometer: the ability to detect the small correlation signals in the stochastic photon noise - to detect the tiny number of physically correlated photons in the stream of randomly arriving photons.

2.4.2 The Narrabri Stellar Intensity Interferometer

After the successful laboratory experiments, in which Hanbury Brown and Twiss demonstrated the measurement of photon bunching at optical wavelengths [71], they applied their technique to on-star measurements in 1956. Using two army searchlight mirrors with a diameter of 1.56 m each, they focused the light of the star Sirius into photomultipliers and recorded the correlations of the intensity fluctuations for different separations of the mirrors. They were able to measure the decrease in correlation with increasing baseline (see figure 2.13), and an angular diameter $\theta = (7.1 \pm 0.5)\,\text{mas}$. [2]

After this first on-sky demonstration of optical intensity interferometry, they started building a larger observatory dedicated for intensity interferometry measurements of bright stars - the *Narrabri Stellar Intensity Interferometer* (NSII), located near the town of Narrabri in New South Wales, Australia. Figure 2.14 shows a photo of the observatory. It consisted of two telescopes which were both assembled on a circular track with 188 meters in diameter, on which they could be moved individually. The telescopes featured paraboloidal reflectors of 6.5 m in diameter, which focused the light into an optical system that collimates it using a negative lens, guides it through an (optical) interference filter, and finally focuses it on a photomultiplier. [76]

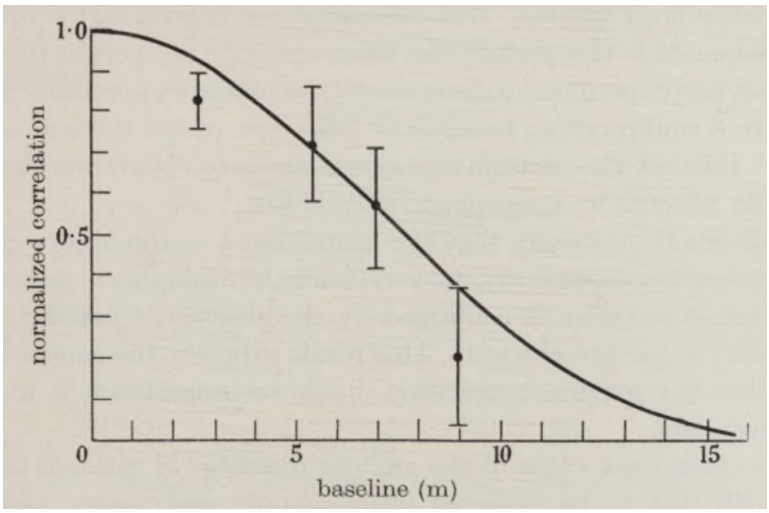

Figure 2.13: Normalized correlation (effectively $g^{(2)} - 1$) over the separation of the telescopes recorded by Hanbury Brown and Twiss measuring the star Sirius. Image taken from [2].

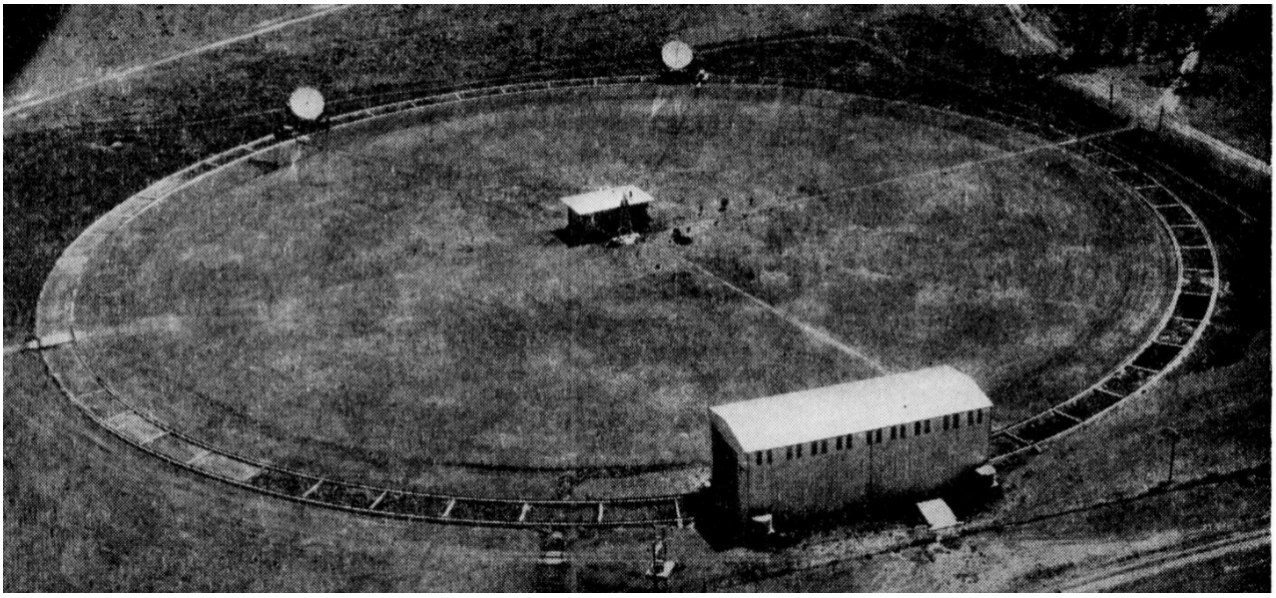

Figure 2.14: A photo of the Narrabri Stellar Intensity Interferometer. Image adapted from [76].

The mobility of the telescopes on the tracks allowed for the adjustment of various baselines between 10 and 188 meters, while a baseline could be kept constant during the tracking of the star by simultaneously moving both telescopes so that their baseline is perpendicular to the direction of the star [76]. In 1967 measurement results for angular diameters of 15 stars were presented [77], while in 1974 a final summary of the NSII observations was published, including angular diameter measurements of 32 stars, the smallest of which (ζ Pup) was measured to $\theta = (0.41 \pm 0.03)$ mas [4].

2.4.3 Requirements for an Intensity-Interferometric Telescope

The NSII was not pursued further due to the impracticability of measuring fainter stars, which would have required much longer measurement times. The biggest downside of an intensity interferometer is the small signal-to-noise of the photon correlation measurement. First of all the time resolution of the system is typically orders of magnitude larger than the coherence time of the light. In addition, the necessity of performing two-photon correlations instead of single-photon interferometry as in the case of amplitude interferometers makes the signal events much rarer [78], and signal-to-noise is significantly worse than in the case of amplitude interferometry. As an example, the *Sydney University Stellar Interferometer* measured the angular size of Sirius using amplitude interferometry at the same precision as the NSII, but in only 2.5 % of the measurement time, while only using 10 cm apertures, compared to the 6.5 m apertures of the NSII [43, 79]. A quantitative view on signal-to-noise for an intensity interferometer will be given in section 3.4, but it should be qualitatively noted here that the disadvantageous feature of poor signal-to-noise ratios in intensity interferometry limits the apparent magnitude of the sources that can be observed, and also results in the need of large telescopes. Figure 2.15 shows the measurements of the NSII in comparison with all the angular diameters that have been measured by various facilities with amplitude interferometers and occultation methods. It is apparent that the stars measured by Hanbury Brown and Twiss are amongst the smallest in angular size, but also amongst the brightest.

An example given by Hanbury Brown was that for the measurement of a magnitude-1 star it would need two telescopes with 2.5 meters in diameter. However, while the size of the telescopes is a strict requirement, the design of the telescope mirrors does not have to be of high optical quality, since their purpose is not to achieve an optical image, but to simply collect the photons and guide them to the photo-detectors. [13]

Large aperture sizes at reasonable costs are therefore realistic, such as the 6.5 m mirrors of the NSII. But also larger aperture sizes are practical and, especially at modern gamma-ray observatories, already available. The fundamental characteristics of an intensity interferometer indeed reveals great similarities with the design of Imaging Atmospheric Cherenkov Telescopes (IACTs). They observe gamma-ray sources by measuring the images of Cherenkov showers produced by gamma-rays entering the Earth's atmosphere. In fact, Hanbury Brown et. al. took the effect of potential coincident Cherenkov shower photons in both telescopes into account, worried that they act as a significant background for intensity interferometry measurements. They found the effect of Cherenkov light for stellar diameter measurements to be negligible, but were able to measure coincident Cherenkov light pulses looking at the dark sky [81]. After a few minor modifications to the telescope (exchanging the photomultipliers and adding additional

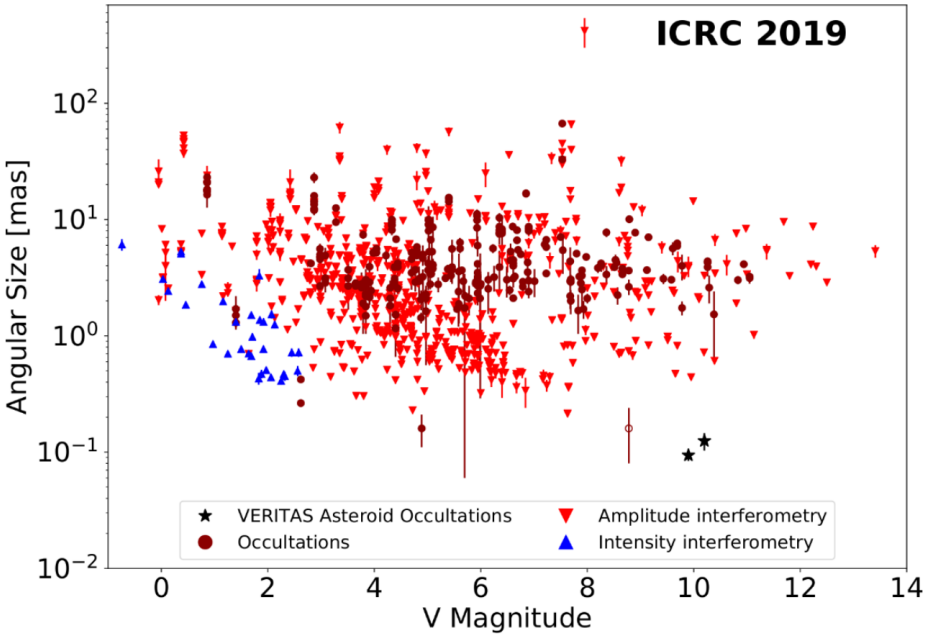

Figure 2.15: Representation of all directly measured angular sizes of stars as of 2019. Intensity interferometry measurements with the Narrabri Stellar Intensity Interferometer are shwon in blue. Image taken from [80].

off-axis photomultipliers) they found evidence for the detection of gamma-rays from the active galaxy *Centaurus A* at the $4.5\,\sigma$ level [82, 83].

Therefore, the inverse question, whether it is possible to perform intensity interferometry measurements with (modern) gamma-ray observatories, can be raised. Practical measurements have proven this suspect in recent years and are discussed in the next section. With the availability of larger mirror diameters of today's IACTs and modern high-time resolution electronics, the astronomical community recently experienced a revival of stellar intensity interferometry.

2.4.4 Modern Intensity Interferometers

The beauty of considering IACTs as intensity interferometers is not just the large mirror diameters and, in principle, fast photo-detector read-out electronics, but also the fact that they usually exist in arrays of two or more telescopes, which can all be combined to perform interferometric observations at various baselines simultaneously. Within the last couple of years, all three famous IACT arrays have started intensity interferometry measurements.

VERITAS

The first successful angular diameter measurements using intensity interferometry at modern IACTs were presented by *VERITAS*, which equipped all four of their IACTs with an external intensity interferometry setup that can be mounted on top of the gamma-ray camera. Correlations between all four telescopes were recorded in December 2019, and precise angular diameter measurements of two stars were initially published (see figure 2.16 for the measurement of β

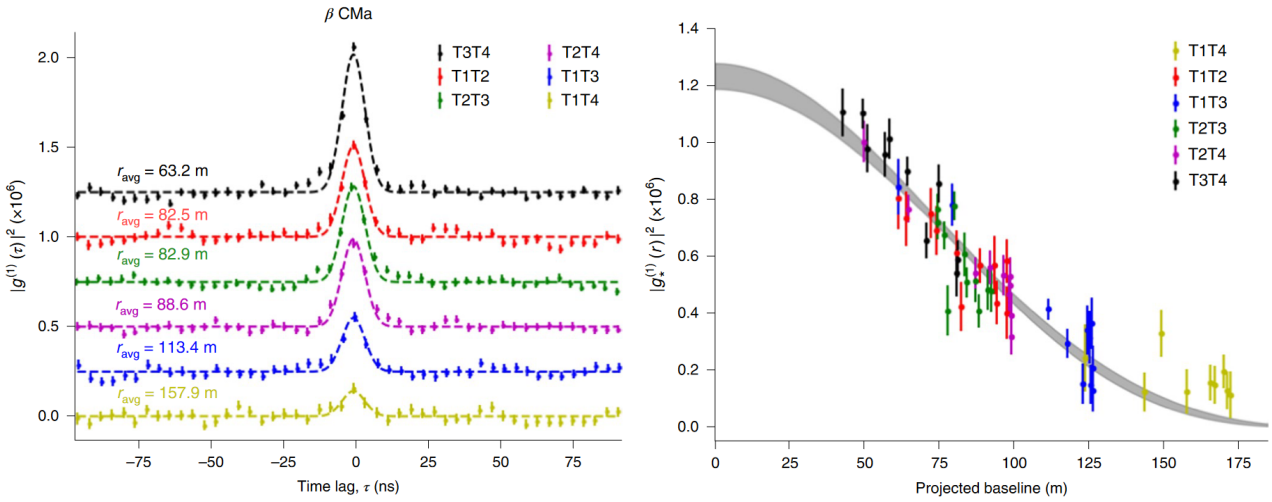

Figure 2.16: Different averaged temporal correlation functions for the different telescope combinations (left) of measurements of the star β CMa using the four VERITAS telescopes, and the amplitudes of the correlation functions plotted versus the projected baseline (right). Image taken from [11].

CMa). In both cases the measured angular diameters agreed with the NSII measurements, but VERITAS was able to measure the angular diameters with higher precision, using only one tenth of the NSII measurement time. [11]

The VERITAS intensity interferometry program is an established routine program during the bright moon times where moonlight prevents gamma-ray observations. Stellar magnitudes of up to 4.2 have been measured since the installation of the intensity interferometry application to the observatory [84].

MAGIC

Intensity interferometry electronics were also implemented into the two *MAGIC* telescopes. In contrast to VERITAS, some of the actual photomultipliers of the gamma-ray cameras are used to record the photon stream in intensity interferometry mode, only the readout procedure was manipulated to access the continuous photo-current from both telescopes [12]. While the number of observed targets as well as the path for fainter stellar magnitudes cannot compare to VERITAS yet, innovative techniques provided by the possibility of adjusting the individual mirror tiles (*active mirror control*) are tested, such as zero-baseline correlations by focusing the light from the individual mirrors in a chess-board fashion into two different photomultipliers, or measuring baselines smaller than the actual telescope diameter by creating sub-mirror configurations (see figure 2.17) [85].

H.E.S.S.

The H.E.S.S. observatory is the last of the three classic IACT arrays to perform intensity interferometry observations. The basic concept is similar to VERITAS' approach of implementing external optics and electronics, however, further spoilers are not given at this point, as the development of the H.E.S.S. intensity interferometry setup is the focus of this thesis, and the reader is encouraged to scan through the following chapters, which describe the tests and

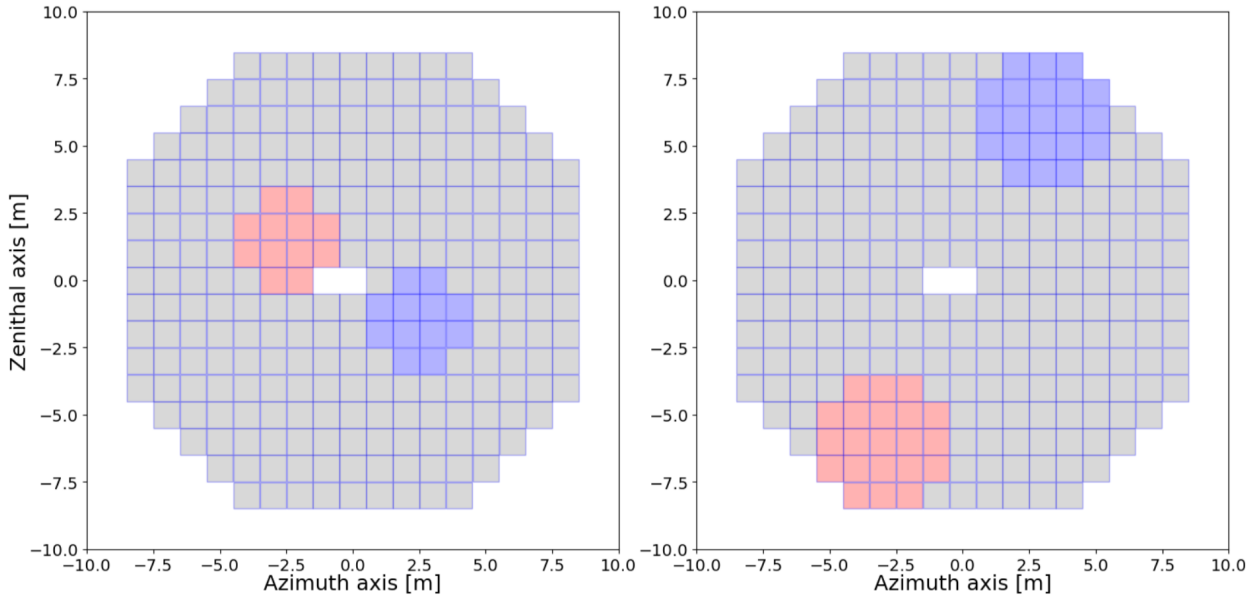

Figure 2.17: Exemplary sub-mirror configurations of MAGIC for the option of measuring baselines shorter than the telescope diameter. Image taken from [85].

analyses during the development of the setup, and finally result in the implementation of the interferometer in chapter 6.

All of these facilities may provide a handy environment for intensity interferometry measurements, but with maximum baselines of 172.5 m (VERITAS [11]) they do not provide baselines surpassing the current amplitude interferometry facilities, and therefore one cannot expect groundbreaking scientific results with never-before achieved angular resolutions. Instead, while each of these observatories may be able to provide valuable scientific contributions to geometric measurements of stars and star systems, they also serve as test facilities for a potential intensity interferometry implementation to the upcoming *Cherenkov Telescope Array* (CTA), which may provide baselines on the order of 2 km [86]. The potential of CTA as intensity interferometer will be discussed in chapter 7.

Optical-telescope intensity interferometers

Even though the desire for large aperture sizes for intensity interferometry has been motivated before, which is one of the main aspects why IACTs are such suitable candidates, there is another development branch of intensity interferometry hardware that is targeting the usually significantly smaller optical-quality telescopes. The idea is to improve in signal-to-noise not by using large light collection areas, but instead ultra-high time resolution electronics. These observatories include e.g. the 1 m diameter telescopes at the *Calern Plateau* near Nice, but also the 1.8 m auxiliary telescopes of the *Very Large Telescope* [87]. While there is no dedicated optical-telescope array for kilometer-scale baselines in construction, the option of measuring photon correlations between portable telescopes [88] opens up new possibilities for stellar intensity interferometry. A quantitative comparison between these two approaches will be given in chapter 5

CHAPTER 3

Broad Optical Bandwidth Intensity Interferometry Measurements at the Statistical Sensitivity Limit Using an LED

3.1 Scope of This Research

The theoretical framework for the calculations of signal as well as statistical noise has now been set up. The quantitative understanding of both aspects in the laboratory is a key aspect on the path to measurements at telescopes. The working group has already gained some experience with the intensity interferometry setup by taking measurements of photon correlations in laser light that is scattered at a rotating ground glass disc, which creates a quasi-thermal light source with a very large coherence time (on the order of several microseconds), and measurements with a mercury lamp, where the sharp atomic emission lines result in coherence times on the order of tens of picoseconds (see [48] for details).

Latter can still be considered large, compared to realistic coherence times in astronomical applications. The spectrum of stars are very broad due to their nature as black body radiators. To simulate this behavior in the laboratory, an LED was chosen, which mimics thermal light behaviour. Even though photon correlations from LEDs have been observed before [89, 90], its practicability as test source for photon bunching measurements hasn't been demonstrated yet. In addition to gaining a full quantitative understanding of the interferometer, the goal was also to test the feasibility of LEDs as sources of thermal light.

In the experiment the light from the LED will be optically filtered to a bandwidth of $\Delta\lambda = 1\,\mathrm{nm}$. The so obtained degree of temporal coherence, expressed by the coherence time, can be approximated to

$$\tau_c = \frac{\lambda_0^2}{c \cdot 1\,\mathrm{nm}} \approx 1\,\mathrm{ps} \tag{3.1}$$

in the green ($\lambda_0 = 532\,\text{nm}$ is used in the measurement). This is a significant decrease compared to the mercury lamp measurements and sets new requirements on the interferometer to be able to detect the bunching signal. While in the laboratory smaller optical bandwidths - resulting in higher degrees of temporal coherence - could be realized, it would be very challenging in telescope implementations, as described in section 3.2.

In the laboratory, the distance between the light source and the detector is limited to a couple of meters. This results in very small coherence lengths (couple of millimeters), even with the effective size of the light source being reduced by a small exit pinhole. Thus, instead of putting two photo-detectors side-by-side, a beamsplitter arrangement is used in which both detectors are ensured to share the same spatial coherence cell. A quantitative description of the degree of spatial coherence, which is even in the beamsplitter arrangement $< 100\,\%$, is given in section 3.3.

3.2 The Feasibility of Narrow-Band Optical Filters for Optical Telescopes and IACTs

In the scope of the astronomical application it is recommended to actively filter the light to a small part of the spectrum. One reason is the increase in the degree of temporal coherence at small optical bandwidths. This argument, however, only applies when systematic effects in the interferometer are not controlled well and systematic noise in the $g^{(2)}$ requires the bunching signals to be of certain absolute height to be visible. In the case of no systematic noise contributions, but pure statistical noise, the signal-to-noise of a photon correlation measurement is independent of the optical bandwidth, as derived in section 3.4. Nevertheless, small optical filters are beneficial since they precisely define the wavelength of observation, and in addition protect photo-detectors from too much incident light.

A filter width of $\Delta\lambda = 1\,\text{nm}$ seems to be working well for optical telescopes, as demonstrated by the C2PU facility at the Calern observatory [91]. Even smaller optical bandwidths can work as well. The Asiago intensity interferometer measured at a filter width of 0.3 nm [9], but the necessary control precision of the light paths is very high and requires very good optical quality telescopes, given that optical filters with bandwidths on the order of less than tens of nanometers are typically realized by interference filters, which require perpendicular incidence of the light. Optical telescopes often provide the option of attaching a user-defined optical setup into the light beam, where the focused light is collimated with the help of lenses.

The working group targets IACTs, which have a precisely defined science case of doing gamma-ray observations and do not allow for handy modifications in the focal plane. A possible workaround, which was adapted by VERITAS [92] and eventually also H.E.S.S. (see chapter 6), can be seen in figure 3.1, proposed in [15], where the light from the telescope mirrors is deflected to the side into a lens system, which collimates the light, leads it through an interference filter, and concentrates it onto a photo-detector.

However, IACTs are often characterized by poor optical mirror and focal spot qualities. The point spread functions of the telescopes CT2 and CT3 of the H.E.S.S. array have been measured to lie within $r_{80\%} = 0.4\,\text{mrad}$ and $r_{80\%} = 0.9\,\text{mrad}$, depending on the elevation of the source, where $r_{80\%}$ denotes the radius in which $80\,\%$ of the total intensity is accumulated [93].

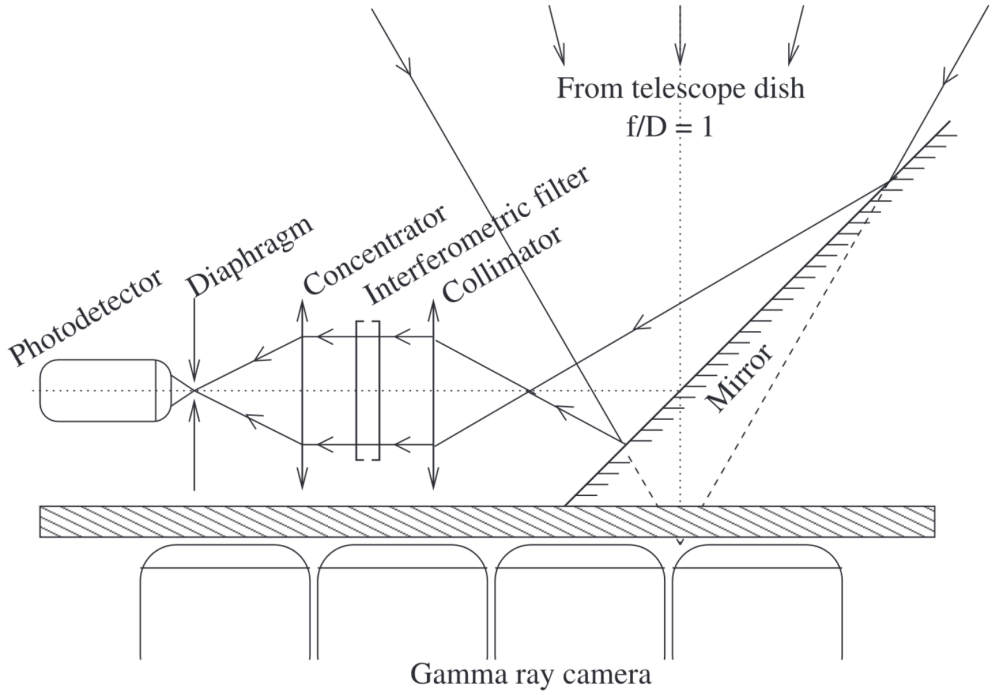

Figure 3.1: Potential optical implementation of collimating optics on a Cherenkov telescope for perpendicular incident light onto the interference filter. Image taken from [15]

This transfers to 6 and 13.5 mm, respectively, on the lid of the telescopes. If the optical filter bandwidth is chosen small (not more than a few nanometers), the quality of light collimation before the interference filter needs to be high, while the collimating optics need to be held rather small, since huge optics are expensive and inconvenient to implement on existing telescopes. For the use of an intensity interferometer at H.E.S.S., described in chapter 6, two-inch optics and 2 nm FWHM interference filters are foreseen.

3.3 Beamsplitter Arrangement and Spatial Coherence Losses

In the laboratory the angular diameter of the source is defined by the 0.3 mm exit pinhole that is installed in front of the LED. At a distance of 3.8 m, the angular diameter is $\theta = {}^{0.3\,\mathrm{mm}}/_{3.8\,\mathrm{m}} = 7.89 \cdot 10^{-5}\,\mathrm{rad} = 16.3\,\mathrm{as}$. This is orders of magnitude larger than the largest stars which one could observe, and the spatial coherence vanishes for the first time at a baseline of only

$$b_0 = 1.22 \cdot \frac{532\,\mathrm{nm}}{7.89 \cdot 10^{-5}} = 8.22\,\mathrm{mm}. \tag{3.2}$$

In order to measure a significant photon bunching signal, the two detectors must be brought together much closer than this distance. But since the housing of a single of the used photomultipliers is already $(22 \pm 0.5)\,\mathrm{mm}$ wide [94], a close enough distance is impossible to realize if put next to each other. For that reason the measurements can only be executed with both photomultipliers being arranged in two arms of a beamsplitter, which results in an effective detector separation of 0.

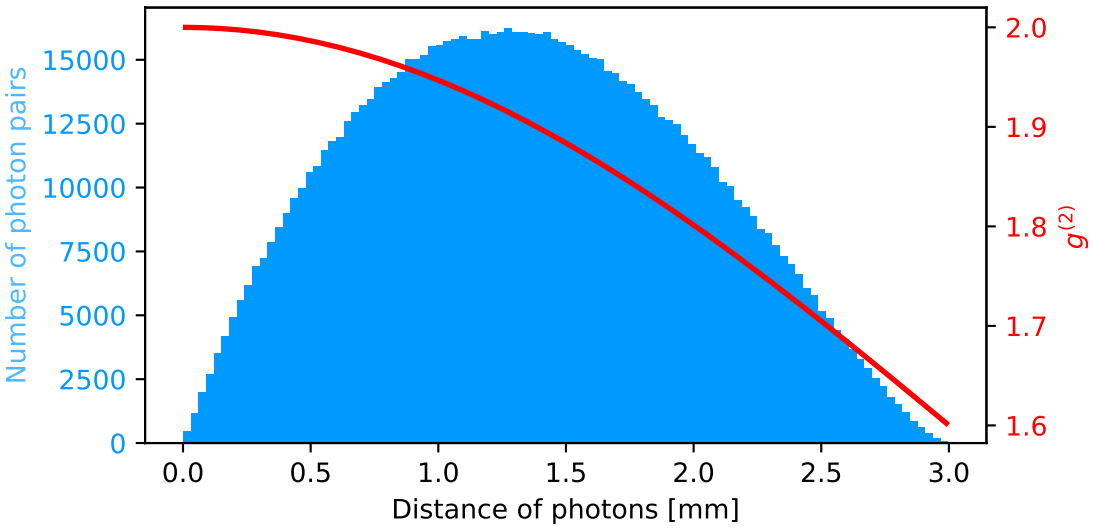

Figure 3.2: Simulations for the calculation of the loss in spatial coherence by the width of the entrance pinhole.

However, one still does not measure the full spatial coherence, since even within the size of the PMTs there is a detectable amount of spatial coherence loss. Photons that are detected at one end of the photo-cathode are already only partially correlated to photons detected at the other end of the photo-cathode. To keep this loss in spatial coherence small there is an additional pinhole of 3 mm installed in front of the beamsplitter, which defines the effective sizes of the PMTs.

The remaining spatial coherence loss within that 3 mm is calculated with a Monte-Carlo simulation, where the positions of photon pairs are simulated randomly over a spherical pinhole, resembling the entrance pinhole of the beamsplitter. The separation of the photons and mutual spatial coherence at this separation are calculated for each photon pair. The mutual spatial coherence is then averaged over all simulated photon pairs. Figure 3.2 shows the simulation for the geometry of the setup used.

The blue histogram shows the distribution of distances the photon pairs have at the pinhole, while the red curve displays the value of the $g^{(2)}$ function at these distances, defined by the angular diameter of the exit pinhole of the LED at the entry pinhole of the beamsplitter. Note that the actual (squared) degree of spatial coherence is $g^{(2)} - 1$, so that e.g. at 3 millimeters the spatial coherence is around 60 %. With this simulation the average degree of coherence turns out to be 0.887.

It is worth mentioning that the setup was not optimized for high signal-to-noise, but rather only for a relatively high signal. A choice of a bigger exit pinhole in front of the LED, or a bigger entrance pinhole in front of the beamsplitter, would result in a smaller expectation value for the measured coherence time due to the reduction in spatial coherence, but also in a smaller value for the statistical noise contributions, since more photons would be detected. While photon rates increase proportional to the square of the pinhole diameters (as long as they are smaller than either the LED or the PMTs themselves), and the noise therewith decreases

proportional to the pinhole diameters, the degree of spatial coherence, which is proportional to the signal, decreases slower, as confirmed by simulations. The motivation for choosing small pinholes is that the PMTs already operated close to their photon rate limit, and measurement time for observing significant signal-to-noise is not limited in the lab.

3.4 A Quantitative Discussion on Signal-To-Noise in Intensity Interferometry

Section 2 in the publication introduces quantitative calculations about signal-to-noise ratios for intensity interferometry measurements. The calculations, however, are kept short, so they are displayed in more detail in this section. The description of signal and noise can be treated independently and combined eventually. The derivations in this section are closely related to the calculations in section 2.3.2 of [48].

3.4.1 Modelling of the Photon Bunching Signal

As described in section 2.3.2, the Wiener-Khinchin theorem connects the power spectrum $s(\omega)$ of the observed light with the temporal $g^{(1)}$ function via a Fourier transform. When the light passes through a narrow optical bandwidth filter the power spectrum is dominantly characterized by the filter transmission spectrum. In the following analytical calculation a Gaussian-shaped filter spectrum is assumed, as it is the case for the measurements in section 3.5. The power spectrum of the transmitted light can be identified as

$$s(\omega) = \frac{1}{\Delta\tilde{\omega}} \exp\left(-\pi \frac{(\omega-\omega_0)^2}{\Delta\tilde{\omega}^2}\right), \tag{3.3}$$

where $\Delta\tilde{\omega}$ describes the width of the filter in angular frequency and translates to the full width at half maximum (FWHM) $\Delta\omega$ via [48]

$$\Delta\tilde{\omega} = \underbrace{\frac{1}{2}\sqrt{\frac{\pi}{\ln 2}}}_{:=k_\Delta \approx 1.06} \Delta\omega. \tag{3.4}$$

Applying the Wiener-Khinchin theorem one obtains

$$g^{(1)}(\tau) = \int_{-\infty}^{+\infty} s(\omega) e^{-i\omega\tau} = e^{-i\omega_0\tau} \cdot e^{-\pi k_\Delta^2 \Delta\nu^2 \tau^2}, \tag{3.5}$$

where $\Delta\nu = {}^{\Delta\omega}/_{2\pi}$. For thermal light sources one can further apply the Siegert relation to obtain

$$g^{(2)}(\tau) = 1 + |g^{(1)}(\tau)| = 1 + e^{-2\pi k_\Delta^2 \Delta\nu^2 \tau^2}. \tag{3.6}$$

As mentioned before, this function decreases towards 1 at a time-scale much shorter than the time resolution of the interferometer, and therefore one will not be able to measure the time-profile of the $g^{(2)}$ function, but only its integral (relative to 1). Latter is what defines the signal and turns out to be

$$S = \int_{-\infty}^{+\infty} \left(g^{(2)}(\tau) - 1\right) d\tau = \frac{1}{\sqrt{2}k_\Delta \Delta\nu} = \frac{1}{\sqrt{2}k_\Delta} \cdot \frac{\lambda_0^2}{c\Delta\lambda} = \underbrace{\frac{1}{\sqrt{2}k_\Delta}}_{:=k_\mathrm{f}} \tau_c. \tag{3.7}$$

With $k_f \approx 0.664$ being the factor described in section 4 of the publication. The peak integral is therefore on the order of τ_c, for a Lorentzian power spectrum one would obtain $S = \tau_c$ [48]. As it will be the case in later chapters, an alternative approach to define the coherence time is to set it equal to the peak integral.

$$\tilde{\tau}_c := S = \int_{-\infty}^{+\infty} \left(g^{(2)}(\tau) - 1\right) d\tau \tag{3.8}$$

This definition is setup-specific and affected by the spatial degree of coherence, but serves as a convenient quantity for signal-to-noise calculations. In case the light is not fully spatially coherent, but only to the degree k_s with $k_\mathrm{s} \in (0, 1)$, the measured signal reduces to

$$S = k_\mathrm{s} k_\mathrm{f} \tau_c. \tag{3.9}$$

As mentioned before, this signal should be contained within the central time bin of the measurement. If the time resolution of the interferometer is however on the order of the bin width or larger, the bunching signal will be spread over several time bins, typically in Gaussian shape.

$$g^{(2)}_\mathrm{lab}(\tau) = 1 + \frac{k_\mathrm{s} k_\mathrm{f} \tau_c}{\sigma_t \sqrt{2\pi}} \exp\left(-\frac{(\tau - \mu)^2}{2\sigma_t^2}\right) \tag{3.10}$$

with σ_t being the time resolution defined as the standard deviation of the Gaussian, and μ the center, which should be $\mu = 0$ unless the peak position is shifted artificially (e.g. by the use of different cable lengths). The amplitude of the Gaussian is set to satisfy equation 3.9, and the characteristic reduction in signal height from 1 to the order of τ_c/σ_t is apparent.

3.4.2 Statistical Noise in the $g^{(2)}$ Measurement

For the modelling of the shape of the $g^{(2)}(\tau)$ in the lab no concrete measurement procedure was specified, except that the transmission profile of the filter is Gaussian shaped and that the time resolution of the system results in a $g^{(2)}$ function that is also Gaussian shaped. For the estimation of the noise of the measurement it is necessary to think of a possible procedure on how to measure the temporal correlation function. Two different ways will be covered in this thesis. The first one in chapter 3 is time-tagging the arrival times of individual photons in both channels and correlating the time stamps. The second one, starting in chapter 4 is a continuous sampling of the photomultiplier currents and correlating the signals. While the treatment of the second method is significantly more complicated concerning both signal and noise, the obtained signal-to-noise ratio should be independent of the used measurement method if the photon rates and time resolution of the system are the same. For the moment it is therefore sufficient to calculate the noise behaviour for the case of photon time-tagging, and introducing the effects of photo-current correlations at a later stage in section 4.4.

A typical photon correlation measurement can look like this: in two time-synchronized photo-detectors the arrival times of the photons are measured and the time tags recorded. One can then compare the arrival time of each photon in one channel with the arrival times of all

photons in the other channel, and calculate the time differences τ. In the case where the light source is of thermal/chaotic nature and at least partially coherent more photon pairs will have a time difference $\tau \approx 0$ (washed out by the time resolution of the interferometer) than any other value, which reflects the detection of photon bunching. Nevertheless, there will be a background of random time differences between un-correlated photon pairs. If the photon rates in both detectors are R_1 and R_2, and the time binning of the measurement is δ_τ, the number of random photon-events for any τ bin after a measurement time T will be on average

$$C = R_1 R_2 \delta_\tau T, \tag{3.11}$$

with a Poissonian statistical fluctuation $\Delta C = \sqrt{C}$. The correlated photon events add on top of these random photon events in the time range around $\tau = 0$, but can only be detected if the excess number of photons in these time bins are significantly bigger than $\sqrt{C}$. The $g^{(2)}(\tau)$ can be obtained by normalizing the histogram of photon pair time differences, which effectively results in every time bin being divided by C. The statistical noise (also called *shot noise*) in each time bin then turns out to be

$$\Delta g^{(2)} = \frac{\Delta C}{C} = \frac{1}{\sqrt{R_1 R_2 \delta_\tau T}}, \tag{3.12}$$

which obeys the typical behaviour of the noise in a counting experiment being proportional to $1/\sqrt{T}$. These fluctuations, observed in the experiment, are the *root mean square* (RMS) oscillations of the correlation function. Combining equations 3.10 and 3.12 allows for the calculation of the signal to noise of a single τ_i bin by calculating $S/N(\tau_i) = g^{(2)}_{\text{lab}}(\tau_i)/\Delta g^{(2)}$, but that underestimates the significance of the whole bunching peak even for $\tau_i = \mu$. Instead, the contributions left and right from the peak maximum need to be taken into account. Approximating the signal to be contained in a range from $\mu - 2\sigma_t$ to $\mu + 2\sigma_t$ one can think of the signal as being composed of the individual time bin contributions. It can be calculated as

$$S = \delta_\tau \cdot \sum_i (g^{(2)}(\tau_i) - 1), \tag{3.13}$$

with the uncertainty

$$\Delta S = \delta_\tau \sqrt{\sum_i \left(\Delta g^{(2)}\right)^2} = \delta_\tau \sqrt{N_{\text{bins}} \cdot \frac{1}{R_1 R_2 \delta_\tau T}}, \tag{3.14}$$

with $N_{\text{bins}} = 4\sigma_t/\delta_\tau$ being the number of time bins in the calculation range. One can identify ΔS as the noise of the measurement and eventually obtains

$$N = \Delta S = \delta_\tau \sqrt{\frac{4\sigma_t}{\delta_\tau} \cdot \frac{1}{R_1 R_2 \delta\tau T}} = \sqrt{\frac{4\sigma_t}{R_1 R_2 T}}. \tag{3.15}$$

3.4.3 Signal-To-Noise

Combining equations 3.9 and 3.15 the signal-to-noise in the measurement is

$$S/N = \frac{S}{N} = k_\text{s} k_\text{f} \tau_c \sqrt{\frac{R_1 R_2 T}{4\sigma_t}} = \frac{k_\text{s} k_\text{f} \lambda_0^2}{c \Delta\lambda} \sqrt{\frac{R_1 R_2 T}{4\sigma_t}}. \tag{3.16}$$

Assuming the photo-detectors are identical, with a detection efficiency of η, one can express the photon rates in terms of the the photon flux density $n(\lambda)$, which describes the number of photons per area and wavelength interval, and the size A of the detector, which in the case of telescopes is their aperture size.

$$R_1 = R_2 = \eta \cdot n(\lambda) A \Delta\lambda \tag{3.17}$$

Equation 3.16 then becomes

$$S/N = \frac{\eta k_s k_f \lambda_0^2}{2c} n(\lambda) A \sqrt{\frac{T}{\sigma_t}}. \tag{3.18}$$

These calculations do not consider any background photons, e.g. flashing lights of electronic devices, as they were measured to be negligible. When the interferometer is installed at the H.E.S.S. telescopes, the effects of night sky background photons are discussed in section 6.7.

3.5 Publication: LED as Laboratory Test Source for Astronomical Intensity Interferometry

The publication has been published as a journal article in Optics Express

LED as laboratory test source for astronomical intensity interferometry

Volume 28, Issue 4, February 2020, Pages 5248-5256
https://doi.org/10.1364/OE.28.005248

The authors are Andreas Zmija, Peter Deiml, Dmitry Malyshev, Adrian Zink, Gisela Anton, Thilo Michel, and Stefan Funk.

First author's contribution (Andreas Zmija) Andreas is, together with Peter Deiml, the main contributor of the research and the text in the publication. The way in which the publication was written does not allow to precisely distinguish between text contributions from both main authors. Both authors worked in a very close collaboration for the execution of the measurements as well as for the writing of all the chapters for the publication. They performed the final as well as the preparatory measurements for the results that are discussed. The data analysis in section 4 was mainly performed by Andreas, but again in close collaboration with Peter. The theory was written by Andreas and Peter as well, however derived together with Gisela Anton.

Co-authors' contributions As described above, Peter Deiml collaborated very closely with the main author for both the execution of the measurements as well as the data analysis. Adrian Zink regularly helped with performing the preparatory experiments in the lab, and also assisted the data analysis frequently. Dmitry Malyshev wrote the first paragraph in the introduction. Stefan Funk produced the setup scheme in figure 1. He also produced all the final plots with the data given to him. While Peter and Andreas

developed the main structure and content of the paper, all the authors contributed with valuable discussions and suggestions for the development of the hardware and software chains, as well as for the publication draft.

Chapter 4

Intensity Interferometry by Photo-Current Correlation: Measurements at Very High Photon Rates

4.1 Scope of This Research

The previous work has proven that the time-tagging intensity interferometer works smoothly and on the theoretically expected signal-to-noise level. An application of this interferometer to optical telescopes seems to be feasible as long as the photon rates in each channel do not exceed significantly more than 10 MHz. However, measurement times of several hours for a single data point are impractical, especially at facilities with limited available observation time. Decreasing measurement time while maintaining high signal-to-noise is possible if the number of photons per wavelength interval can be increased. For astronomical observations, this quantity directly scales with the light collection area of the used telescope. For this reason, the Phase I telescopes of the H.E.S.S. observatory, which have mirror (dish) sizes of 13 m and mirror areas of about 100 m^2 [95], were taken into consideration for measuring the photon bunching peaks of stars. It can be shown that the expected photon rates exceed the rate threshold of the previously used time-tagging electronics by at least an order of magnitude, as it is quickly described in section 2 in the paper, and derived in more detail in section 4.2 of this thesis.

The bandwidths of the optical filters used in the new measurements are $\Delta\lambda = 2\,\mathrm{nm}$, and are input to the calculations. One may argue that a smaller bandwidth could decrease the photon rates to fall below 10 MHz again, while keeping the photon-per-bandwidth density constant. However, as described in section 3.2, the poor optics of IACTs do not allow for very small optical bandwidths. Instead, as given in equation 3.18, the optical bandwidth does not affect the signal-to-noise of the measurement[1], and consequently a broader optical bandwidth is a reasonable choice in the view of measurements at IACTs. A requirement however is a change of the electronics to a system that can deal with the much higher photon rates. Such photon counting detectors are currently being developed [96], but yet far from a practical

[1] assuming the emission spectrum of the star is constant within the range of potential filter widths

and cost-effective use. As an alternative to time-tagging of single photons at high photon rates, photon correlations can also be measured by continuously digitizing the photomultiplier currents (*waveforms*) in the correlation channels, and correlating the data streams. This is described in section 3 in the paper, and in more detail in section 4.3 in this thesis.

4.2 Calculation of Expected Photon Rates for Stars

The brightness of a star is usually given using the logarithmic magnitude scale, where the absolute magnitude M is a distant-independent classifier of a star, while the apparent magnitude m describes its brightness as observed from earth [97]. The definition of the magnitudes arises from the equation of the difference between two magnitudes:

$$m_1 - m_2 = -2.5 \cdot \log_{10}\left(\frac{f_1}{f_2}\right) \tag{4.1}$$

with f_i being the fluxes of the stars [98]. Setting $m_1 = m_x$ as the magnitude of the observed star observe and $m_2 = 0$ one finds

$$m_x(\lambda) = -2.5 \cdot \log_{10}\left(\frac{f_x(\lambda)}{F_\nu(\lambda)}\right) \Leftrightarrow f_x(\lambda) = F_\nu \cdot 10^{-m_x/2.5} \tag{4.2}$$

with F_ν being the flux that corresponds to a magnitude of $m = 0$, which has to be defined further. Since the spectrum of a star is not uniform, a wavelength dependency has to be added. The calibration star was defined to be Vega (α Lyrae) [98], and calibration data can be read from Bessell (1979) [99] for the different light bands. For the B band (calibration at $\lambda = 440\,\mathrm{nm}$) one reads

$$F_\nu(\lambda = 440\,\mathrm{nm}) = 4.26 \cdot 10^{-23} \frac{\mathrm{W}}{\mathrm{m^2 Hz}}. \tag{4.3}$$

f_x can be identified with the light power P per area A and frequency interval $\Delta\nu$.

$$f_x = \frac{P}{A\Delta f} = \frac{N_\gamma E_\gamma}{TA\Delta\nu} \tag{4.4}$$

with N_γ being the number of photons in the time interval T, and E_γ the photon energy. One can denote $R_\gamma = N_\gamma/T$ as the photon rate and change the frequency interval to a wavelength interval via $\Delta\nu = c\Delta\lambda/\lambda^2$ (see e.g. [48]), to calculate R_γ as

$$R_\gamma(\lambda) = \frac{f_x(\lambda) A \Delta\lambda}{h\lambda} \tag{4.5}$$

with h being the Planck constant, and finally, using equation 4.2, compute the measured photon rate in the detector as

$$R_{\mathrm{meas}} = \frac{1}{2} \cdot \eta \cdot \frac{A\Delta\lambda}{h\lambda} \cdot F_\nu(\lambda) \cdot 10^{-\frac{m_x}{2.5}} \tag{4.6}$$

where η is the combined efficiency of the light propagation in atmosphere, telescope and eventually detection efficiency of the photo-detector. The factor $1/2$ takes into account that the light is split in each telescope with a beamsplitter towards two photo-detectors. Figure 4.1 shows

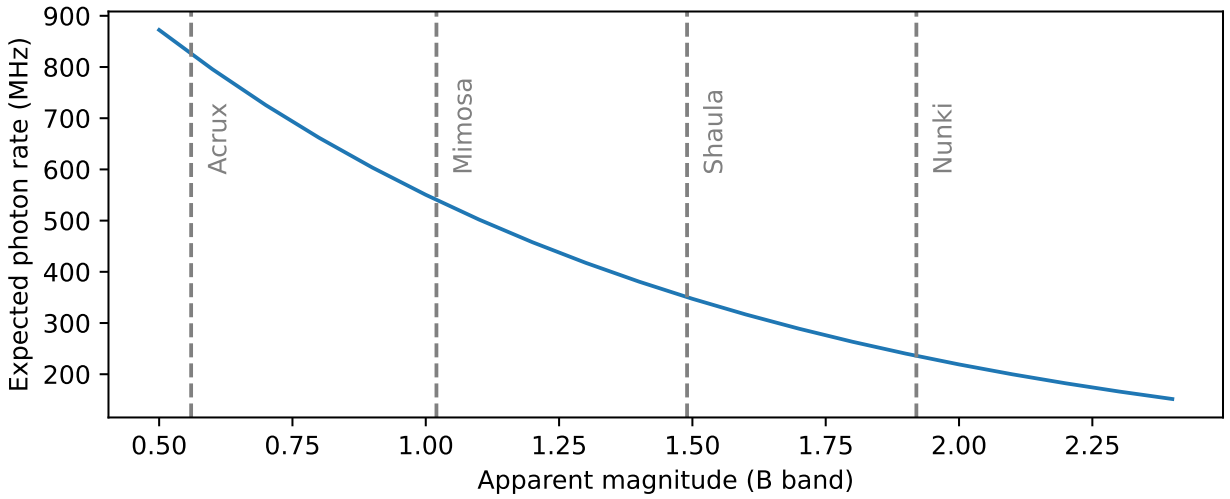

Figure 4.1: Expected photon rates as a function of the apparent magnitude following equation 4.6. Values for the apparent magnitudes of the stars were taken from the SIMBAD database [101], except for Acrux ([102]).

the expected photon rates per detector for an optical filter width of 2 nm and a telescope size of 100 m^2 as a function of the apparent magnitude of the source. Here, $\eta = 0.1$ is assumed, which is a realistic but conservative guess: the photomultipliers which are used in the measurements have quantum efficiencies of $> 30\,\%$ at 465 nm [100], in combination with the estimation of the light collection and transmission efficiency of also around 30 % it yields $\eta = 0.1$.

Photon rates of more than 200 MHz are expected for every planned target to be measured with H.E.S.S..

4.3 Current Correlation Electronics and Analysis Pipeline

The digitizer hardware was switched from a time-tagger to an analog-to-digital converter (ADC). Instead of time-tagging the photon arrival times, a waveform is recorded, which is the photo-multiplier current sampled in fixed time intervals. The digitizer is a M4i.2212-x8 card from Spectrum instrumentation. The signals in each of the up to four input channels can be digitized with a sampling frequency of 1.25 GHz, which relates to sampling time steps of 0.8 ns [103].

Figure 4.2 shows the analysis pipeline for this experiment. A single source data file contains 3.436 s of data of both correlation channels. A correlation is computed for each acquisition file. Figure 4.3 (blue) shows such a correlation of a 3.436 s measurement. At first, the DC offset of the measurement waveforms is removed. Instead of doing this in the raw waveform data, it can also be done in the correlation, which is faster and requires less computation power. The correction follows the subtraction of the last term in equation (7) in the corresponding publication. This does not change the shape of the correlation, but shifts it along the vertical axis in either positive or negative direction, depending on the DC offsets. The offset-corrected data is shown in figure 4.3 in red and differs from the blue curve only by the values on the vertical axis.

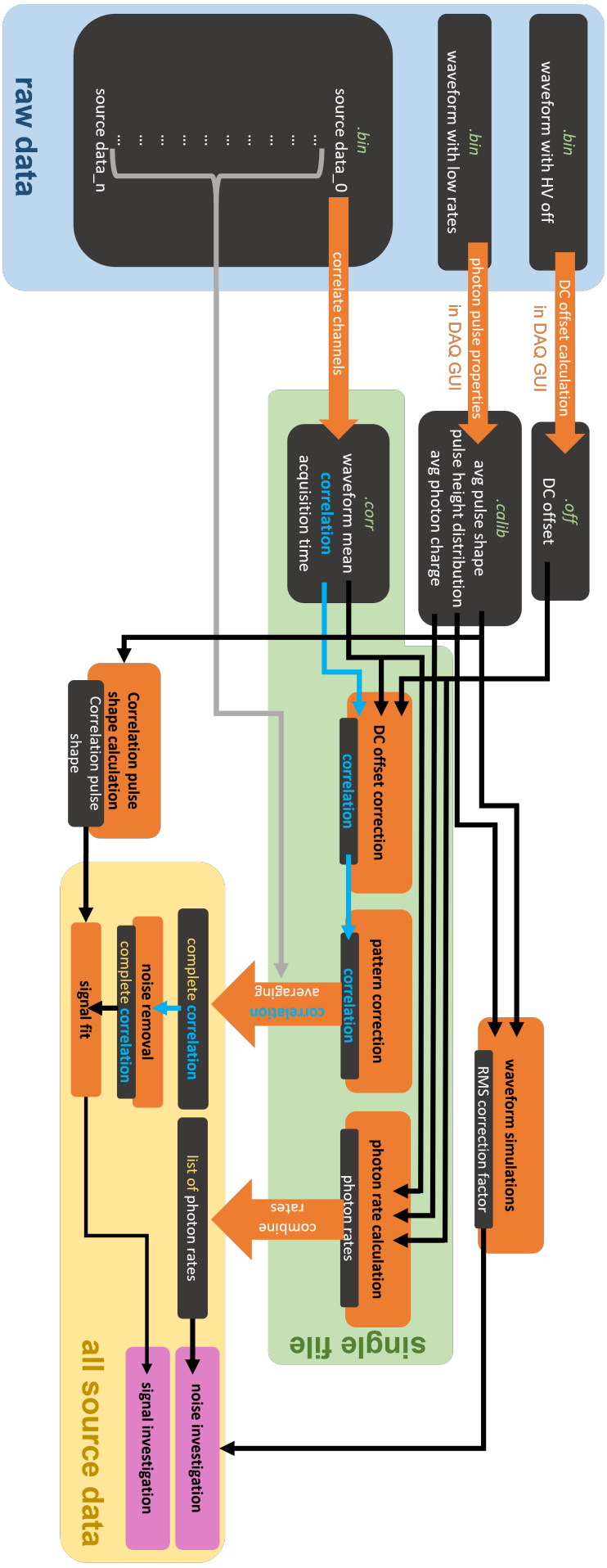

Figure 4.2: Analysis pipeline for laboratory experiments

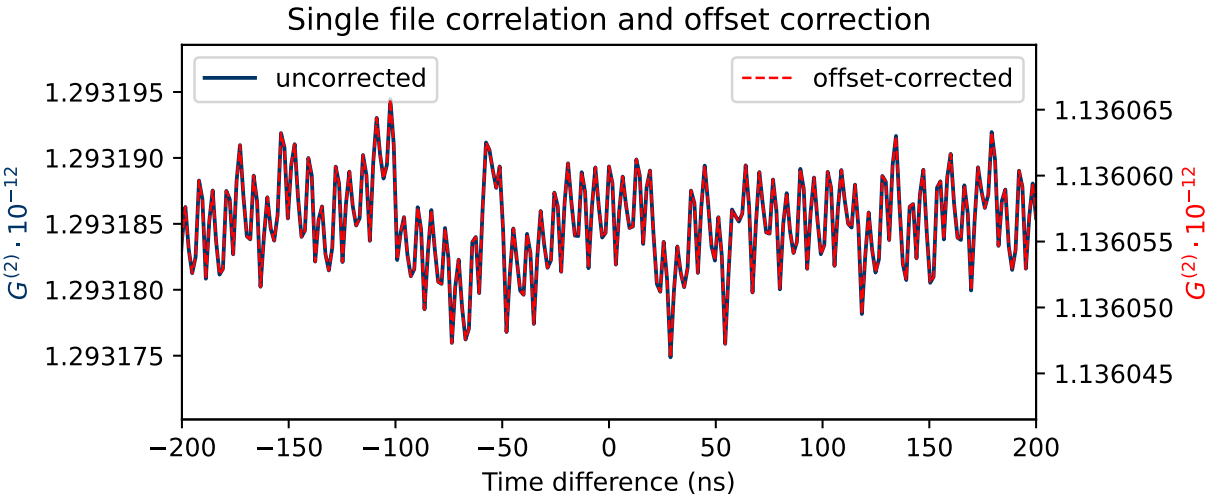

Figure 4.3: Single file correlation data without (blue) and with (red) DC offset correction.

Further it is apparent that the correlation shows a distinctive systematic oscillation pattern. It is 8-bin periodic and easily removed by extracting the pattern from the corresponding data itself. Since the pattern is deterministic, but superimposed by the stochastic oscillations of the photon statistics, averaging over many 8 bin periods averages out the stochastic part and leaves one with the systematic pattern, which can then be used to remove it from every correlation time bin. By this, the data automatically get normalized and oscillate around 1, and thus can be identified with $g^{(2)}$. Fig. 4.4 shows the data before and after the pattern correction.

The $g^{(2)}$ functions of all the data files are then averaged to form the correlation over the complete measurement time.

4.4 Signal and Noise in Current Correlation Measurements

The transition from time-tagging to current correlations changes the qualitative and quantitative behaviour of $g^{(2)}$. Since the pulses of (single) photons are extent over several time bins in a waveform, neighbouring time bins in the correlated data are not statistically independent of each other. Instead, correlation of the $g^{(2)}$ values over several time bins are observed, which is also affecting the RMS expectation value of the $g^{(2)}$ function in the regime where no photon correlations are observed. The quantitative behaviour, effectively the calculation of an RMS expectation correction factor, is understood with the help of waveform simulations. The RMS correction factor turns out to be smaller than one, meaning that the observed RMS of the $g^{(2)}$ curve falls below the shot noise expectation of equation 3.12.

The extent of photon pulses in the waveforms also results in the photon bunching peak in the $g^{(2)}$ function being broader than just the broadening by the time resolution. This behaviour is described in detail in the publication, but the important aspect for signal-to-noise calculations is that due to the broadening of the peak, its height decreases, so that the integral remains the same. The decrease in signal height compensates the decrease in the RMS, and signal-to-noise is therefore identical with the equations derived in section 3.4.

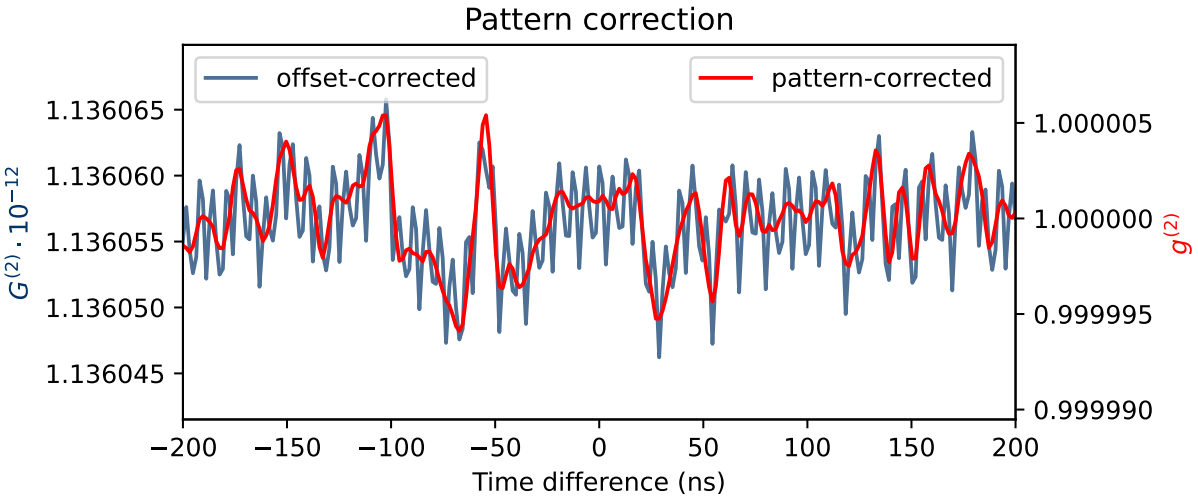

Figure 4.4: Single file correlation data without (blue) and with (red) pattern correction. Due to the low statistics of such a short correlation measurement, no bunching signal is visible.

4.5 Publication: Optical Intensity Interferometry Lab Tests in Preparation of Stellar Diameter Measurements at IACTs at GHz Photon Rates

The publication has been published as a journal article in the Monthly Notices of the Royal Astronomical Society

Optical intensity interferometry lab tests in preparation of stellar diameter measurements at IACTs at GHz photon rates

Volume 509, Issue 3, January 2022, Pages 3113-3118
https://doi.org/10.1093/mnras/stab3058

The authors are Andreas Zmija, Naomi Vogel, Gisela Anton, Dmitry Malyshev, Thilo Michel, Adrian Zink and Stefan Funk.

First author's contribution (Andreas Zmija) The author developed major parts of the analysis chain for the measurements, described in section 4 of the paper. This includes the correlation algorithm, the DC offset correction, and the concept of the calibration measurements and its application to the analysis. The measurement of the gain stability was performed together with Naomi Vogel and Adrian Zink, the correlation measurements were performed by the author. The analysis of the correlation, meaning developing the template fits as well as the RMS noise analysis was also performed by Andreas, who further developed the concept of the RMS correction factor with the help

of waveform simulations. The measurements were mainly performed by Andreas, often with the help of Naomi Vogel and Adrian Zink. Andreas was main contributor to almost all of the texts and figures in the publication, except of the parts mentioned below. The structure of the publication was developed mainly together with Naomi.

Co-authors' contributions Naomi Vogel developed algorithms for the calibration measurements described in section 4.3. This involves extracting the average photon pulse shape and the pulse height distribution, where she created the plots from figures 4 and 5. She also helped with measurements towards the publication, and developed section 3.1 together with Andreas. She regularly helped Andreas with preparatory measurements. Adrian Zink (re-)developed major parts of the hardware electronics and occasionally helped at measurements towards the publication. While Naomi and Andreas developed the main structure and content of the paper, all the authors contributed with valuable discussions and suggestions for the development of the hardware and software chains, as well as for the publication draft.

4.6 Virtual Telescope Baselines

The optical setup in the publication is very similar to the previous setup described in the paper in section 3.5, featuring a small pinhole in front of the thermal light source to increase the spatial coherence in the observation plane. And just like before, despite the fact that the photomultipliers do not have any effective separation in the arrangement of the beamsplitter, they are measuring a reduced spatial coherence, which is understood by the fact that the coherence length of the light field from the source is smaller than the size of a single photomultiplier cathode. For the initially used 30 µm diameter pinhole this results in an averaged spatial coherence of 80 %, in case of the 75 µm pinhole in an averaged spatial coherence of 36 %.

One would measure the same reduction in spatial coherence in a setup were both detectors were negligibly small, but actually separated from each other by a specific baseline. With this analogy, the two degrees of spatial coherence that were produced in section 5 in the publication can be interpreted as a virtual telescope baseline, and the measurement results can be plotted using this analogy, as it is done in fig. 4.5.

Using the analogy of the virtual telescope baseline it becomes apparent how similar the lab measurements are to an actual field measurement using spatially separated detectors observing the spatial coherence of a star. The transition to telescopes is therefore the next logical step. However, before the setup has actually been installed on IACTs, the two different approaches for intensity interferometry are compared in a combined experiment with the Quantum Information group of Prof. Dr. Joachim von Zanthier. This comparison will be demonstrated in the next chapter.

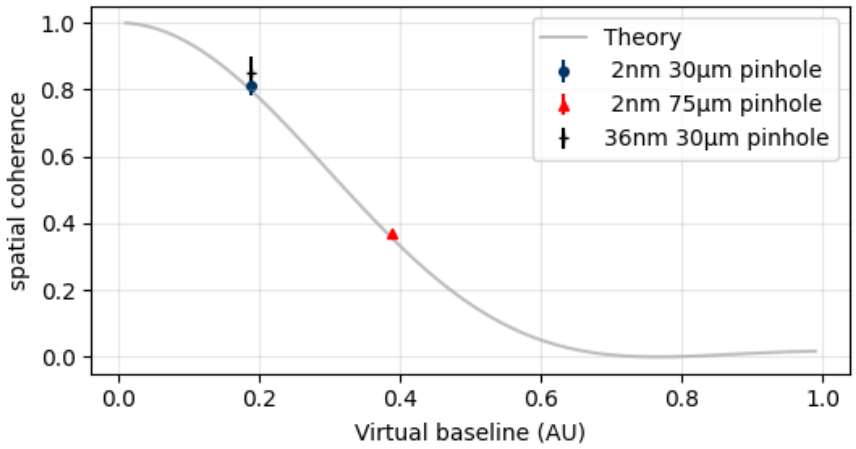

Figure 4.5: Measured spatial coherence values vs the virtual telescope baseline.

Chapter 5

Comparison of Different Approaches: High Time-Resolution Versus High Photon Rate Systems

5.1 Scope of This Research

Two different approaches for performing intensity interferometry were presented in the previous two chapters. The first method in chapter 3 uses time-tagging of the arrival times of single photons and calculating the time differences between the arrival times in both channels to do the correlation, which is a convenient method for photon rates of not more than a couple of MHz. The second method from chapter 4 instead uses the digitized photo-multiplier currents as input for the correlation. This method allows for high photon rates without a theoretical upper limit, as long as the PMT anode and/or cathode current is not exceeded or saturated in the digitizer, which can be prevented by decreasing the high voltage for increasing photon rates. It was mentioned that the reason for the transition to the current correlation system that can sustain the high rates was the desire for higher signal-to-noise, which can be achieved using larger collection areas such as the mirrors of IACTs. The quantitative description is given in equation 3.18 which is recalled here.

$$S/N = \frac{\eta k_s k_f \lambda_0^2}{2c} n(\lambda) A \sqrt{\frac{T}{\sigma_t}} \propto \frac{A}{\sqrt{\sigma_t}} \tag{5.1}$$

The approach of targeting large telescopes is justified in the linear dependency between signal-to-noise and the light collection area. However, as can be seen from this equation, another possible approach is increasing the time resolution (decreasing the value of σ_t). While the reported time-tagging system had a time resolution of $\sigma_t = (645 \pm 9)\,\mathrm{ps}$ [104], current state-of-the-art electronics can provide significant improvements to that. Photo-detectors with timing resolution on the order of only a few (tens) of picoseconds have been developed, e.g. single-avalanche photo diodes with a time resolution of 35 ps FWHM [105], or hybrid photo-detectors using avalanche diodes reached timing resolutions of $\sigma_t = 26\,\mathrm{ps}$ [106]. These detectors are typically restricted to only a couple of MHz per detector, mostly due to detector dead-times. Naturally, these detector systems fit to telescopes of rather small diameters, which

provide optical quality and enable precise control of the light path and therewith the option of narrow-band optical filtering.

The working group of Prof. Dr. Joachim von Zanthier from the institute for optics, information and photonics, also part of the Friedrich-Alexander-Universität Erlangen-Nürnberg and located in close proximity to ECAP, is developing high time-resolution photon counting systems. Their interferometer supports timing resolutions of 41.6 ps FWHM [107]. They identified stellar intensity interferometry as a possible application, and were able to measure the photon bunching signal of Vega with a 0.5 m telescope at the Bamberg observatory [10]. Both groups have already been cooperating for years, and decided to work on a combined project comparing both of the approaches, including combined intensity interferometry measurements with both detector systems.

The possible number of criteria for qualitative and quantitative comparisons is huge, depending on the scientific goal of the final experiment. The ideal astronomical intensity interferometer can be defined by a set of requirements:

- A good signal-to-noise in a reasonably short measurement time is desirable. This is especially crucial when the access to measurement time at the telescopes is limited, as it is true for any observatory which is not self-designed.
- A big u-v-coverage is important for a dense information map for reconstruction of the source parameters. This is defined by the number of telescopes of the array, as well as by their separations. Depending on the science target, there is again a wide span of parameters which suits the observation best.
- Cost-effective realizations of the intensity interferometry implementation allows for an expansion to many telescopes, if available.

A comprehensive discussion on which method and arrays are best suited for long-term intensity interferometry applications would require to either investigate the complete set of possible observation targets for each of the intensity interferometry options, or to restrict the survey to a limited amount of different targets. However, instead of deciding about a general ranking of the two intensity interferometry approaches, the working groups decided to only focus the research on signal-to-noise investigations.

5.2 Publication: Comparing Different Approaches for Stellar Intensity Interferometry

The publication has been published as a journal article in the Monthly Notices of the Royal Astronomical Society

Comparing different approaches for stellar intensity interferometry

Volume 512, Issue 2, May 2022, Pages 1722-1729
https://doi.org/10.1093/mnras/stac489

The authors are Sebastian Karl, Andreas Zmija, Stefan Richter, Naomi Vogel, Dmitry Malyshev, Adrian Zink, Thilo Michel, Gisela Anton, Joachim von Zanthier and Stefan Funk.
This paper is a collaborative effort of two working groups, where each group is responsible for parts of the data creation. Both groups provided a leading author for this paper, who is the main contributor of the content of the corresponding working group. for the "High time resolution" (HTR) system developed by the working group of Joachim von Zanthier, the main author is Sebastian Karl, while for the "High photon rates" (HPR) system developed by the working group of Stefan Funk, the main author is Andreas Zmija. Both authors therefore contributed equally and share a first authorship.

First author's contribution (Andreas Zmija) Andreas is the main contributor of the HPR part of the project. He described the HPR part of the setup in section 3 and performed major parts of the analysis of the HPR measurements. This results in the plots in figure 3 as well as in the description of the HPR results in section 4. Andreas wrote major parts of abstract and introduction. He provided the signal-to-noise analysis in section 5, including the analogy of the effective telescope areas for both measurements, and created the significance map in figure 5 with the help of the telescope data from figure 1, which he collected together with Naomi and Sebastian. The discussion part of figure 5, which extends until the end of the section 5, is written in a very segmented way together with Sebastian Karl, given the frequent alternations of description of HPR and HTR systems.

First author's contribution (Sebastian Karl) Sebastian is the main contributor of the HTR part of the project. He created the measurement setup scheme in figure 1, described the HTR part of the setup in section 3 and performed major parts of the analysis of the HTR measurements. This results in the plots in figure 2 as well as in the description of the HTR results in section 4. Sebastian wrote small parts of the introduction and major parts of the theory section. The discussion part of figure 5 in section 5, which extends until the end of the section is written in a very segmented way together with Andreas, given the frequent alternations of description of HPR and HTR systems. Sebastian provided the parameter definition illustration (figure 4).

Co-authors' contributions Together with the main authors, Sebastian and Andreas, Naomi Vogel and Stefan Richter can be identified as the main contributors to this paper. They produced the data for the publication, by performing the final correlation as well as several preparatory measurements. Adrian Zink occasionally helped during the preparatory measurements. Sebastian, Naomi and Andreas collected the data for comparison of the different telescopes, resulting in table 1 and figure 5. The four main contributors discussed the paper structure and its content in detail, while all the authors contributed with valuable ideas and discussions for the development of the project, as well as proof reading of the paper draft.

CHAPTER 6

Intensity Interferometry Measurements With the H.E.S.S. Gamma-Ray Telescopes

6.1 Scope of This Research

After the laboratory measurements have demonstrated that the intensity interferometry setup is capable to produce measurement results which not only show the expected coherence time, but are also only shot-noise limited, it was implemented onto two of the Phase I telescopes of the High Energy Stereoscopic System (H.E.S.S.). The transition from laboratory experiments with a single interferometer, consisting of one beamsplitter and two photomultipliers, to a system with setups installed on two separate telescopes, creates a set of new challenges to be dealt with.

In the laboratory, the incident light beams on the interferometer can be assumed to be effectively parallel and perpendicular on the interference filter, given the large ratio of the distance of the light source to its size (and the size of the aperture, respectively). In contrast, the light which is reflected from the telescope mirrors is focused and therefore highly non-parallel, which requires additional optics in order to keep the effects of non-parallel light on the interference filters minimal. Further, the tracking of the source by the telescope mechanics is not perfect, resulting in a movement of the star's spot in the focal plane, which needs to be accounted for. The modifications of the intensity interferometry setup to adapt for these issues are described in section 6.3.

While the telescopes observe a star over several hours within a night, the pointing direction of the telescopes changes in order to track the star. This results in a change of the projected baseline between both telescopes as seen from the star, which defines the effective detector separation. This variation in telescope baselines is actually desired, as it allows the observers to measure multiple baselines using only two telescopes. The constant change in telescope baselines, however, needs to be taken into account carefully in the analysis. An extension of the analysis pipeline from chapter 4 is briefly described in section 6.4.

Hand in hand with the changing of telescope baselines acts the changing of the difference in path lengths the wavefronts of the starlight need to travel to enter the telescopes separately. This shifts the bunching peak position in the $g^{(2)}$ function time-dependently. The effects that occur due to that optical path delay and the correction algorithms are described in section 6.5.

6.2 Measurement Timeline

The cameras of IACTs have to be very sensitive to the faint, short Cherenkov light flashes, which makes conventional gamma ray observations during phases of bright moonlight difficult, if not impossible [108]. Usually, observations pause during the phases of bright moonlight for a couple of days [109], while there are efforts and running programs to extend the duty cycle of IACTs during partial moonlight [108, 109], including H.E.S.S., which started with moonlight observations in 2019 [110]. Nevertheless, gamma-ray moonlight observations at H.E.S.S. are only performed up to a moon phase of 40% [110], and there is a significant amount of night time each moon cycle where the observation schedule pauses. For the moon light period in April 2022, this amount summed up to about 130 hours [111].

While bright night sky background due to moonlight is a major issue for the imaging atmospheric Cherenkov technique, it is not so much for intensity interferometry, as long as the ratio of the background photon rate R_B to the source photon rate R_S, denoted by $Q = {}^{R_\mathrm{B}}/_{R_\mathrm{S}}$ is small. Uncorrelated background photons increase the required measurement time for a given signal-to-noise proportional to $(1+Q^2)$, as will be derived in section 6.7. Since the field of view of an intensity interferometer can be kept small, so can Q for bright stars, even at significant moonlight conditions. Hence, intensity interferometry measurements can complement the measurement schedule of an IACT array.

The first intensity interferometry campaign at H.E.S.S. was scheduled for the moonlight period in April 2022. Figure 6.1 shows the available measurement time for intensity interferometry observations during that time. Due to the equipment being stuck in customs, the first half of the moonlight time could not be used for intensity interferometry measurements, only from the night of April 16 measurements were running. Significant amounts of data were taken for the three star systems of Acrux (α Cru), Shaula (λ Sco) and Nunki (σ Sgr), which are the main targets discussed in the paper.

6.3 The Intensity Interferometry Setup for H.E.S.S.

The intensity interferometry implementation to the telescopes should fulfil two requirements. The first is that the aforementioned optical and electronic conditions are satisfied, which are collimating optics for the optical bandwidth filtering and continuous digitization of the PMT currents. This makes it clear that the cameras of the H.E.S.S. telescopes can not be used for operation, but instead a fully external system was designed. The second requirement is that smooth transitions between gamma-ray and intensity interferometry measurements are ensured. The setup was hence designed to be mounted onto the lid of the Cherenkov cameras, in a way that the lid can open with the setup attached. Switching between gamma-ray and intensity

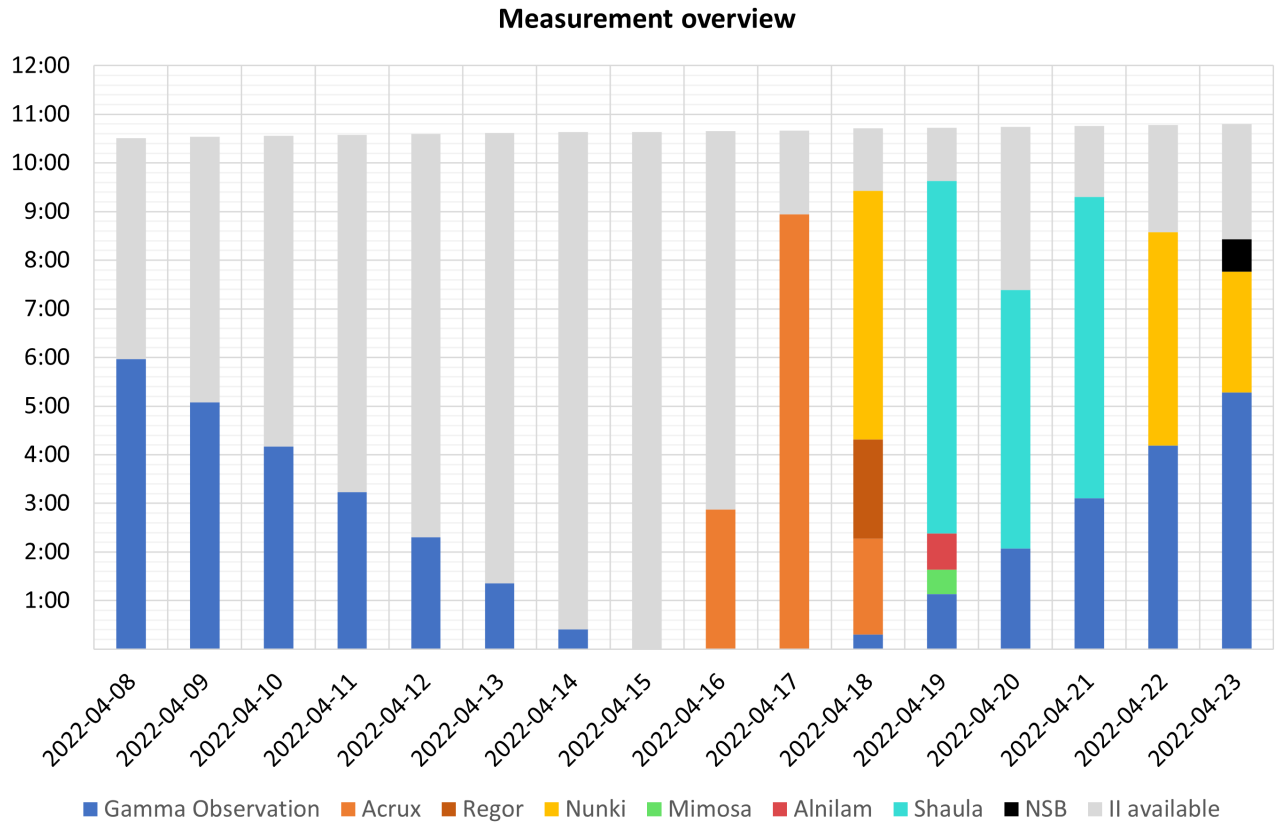

Figure 6.1: Measurement schedule for the 2022 campaign. The blue bars denote the gamma ray observation time for each night, while the other colored bars show the distribution of the intensity interferometry measurement time on the different targets. The grey bars denote the available measurement time for intensity interferometry which was not used, mainly due to the late arrival of the measurement equipment. Graphic adapted from [111].

interferometry measurements is possible by simply opening or closing the camera lids, which takes less then a minute, and does not require additional manpower.

In addition to previous versions of the interferometer, which consisted mainly only of the optical filter, a beamsplitter and both photomultipliers, a lens system was installed, which parallelizes the light incident from the telescope mirrors. Parallel light is necessary for the desired transmission at the interference filter. The optical setup is completed by a 45° mirror which reflects the light from the telescope mirrors into the lens system.

Unlike optical telescopes, IACTs often don't provide continuous tracking of the source with highest accuracy. Especially since the H.E.S.S. telescopes are controlled with altitude-azimuth mounts [112], which is prone to tracking uncertainties, significant pointing inaccuracies are likely. Quantitative pointing deviations can be read from pointing models, in Lennarz (2012) [113] one reads mean pointing offsets of 141 as in azimuth and −73 as in altitude, and additional fluctuating pointing deviations on the order of up to 50 as, depending on the altitude-azimuth position. At a focal length of 15 m [95] this transfers to an offset of the focal spot position on the camera lid with respect to its nominal position of 1.24 cm in horizontal and 0.53 cm in vertical direction, with an additional wobbling on the order of 0.36 cm. As corrections in the position reconstruction of gamma-rays can also be performed in the data after the measurement, there is no need for accurate live pointing corrections of the telescope tracking during gamma-ray measurements. However, the intensity interferometer does require precise control of the optical light path, as the light has to enter the optical system without much leeway.

Sebastian Konrad simulated the effect of inaccurate pointing with respect to the position of the intensity interferometry tube system, details can be found in [114]. The simulations have shown that the optical transmission through the lens system decreases from $\approx 85\%$ to $\approx 65\%$ at a pointing offset of 0.5 cm, while also the transmission spectra of the interference filters slightly change due to non-perpendicular incidence angles.

Instead of implementing a live pointing correction algorithm to the telescopes, it was decided to design the intensity interferometry setup in a way that the position of the optical elements, which are the 45° mirror and the lens tube system, can be moved via stepper motors and controlled remotely in order to "follow" the position of the focal spot. The initial spot finding algorithm was developed by Frederik Wohlleben in [115].

6.4 Analysis Pipeline

Figure 6.2 shows the extended analysis pipeline adapted to the analysis of telescope data. The main extension to the previously shown diagram (figure 4.2) is the division of the raw data into measurement segments, in which the correlation functions are analyzed individually. The purpose of this division is to separate measurement blocks of different projected baselines from each other, to observe the baseline-dependent change of the measured coherence time. If the star to be observed for the night is chosen wisely it is often possible to scan a range of different telescope baselines within one night that is sufficient for a spatial coherence analysis that eventually allows fitting the angular size of the star.

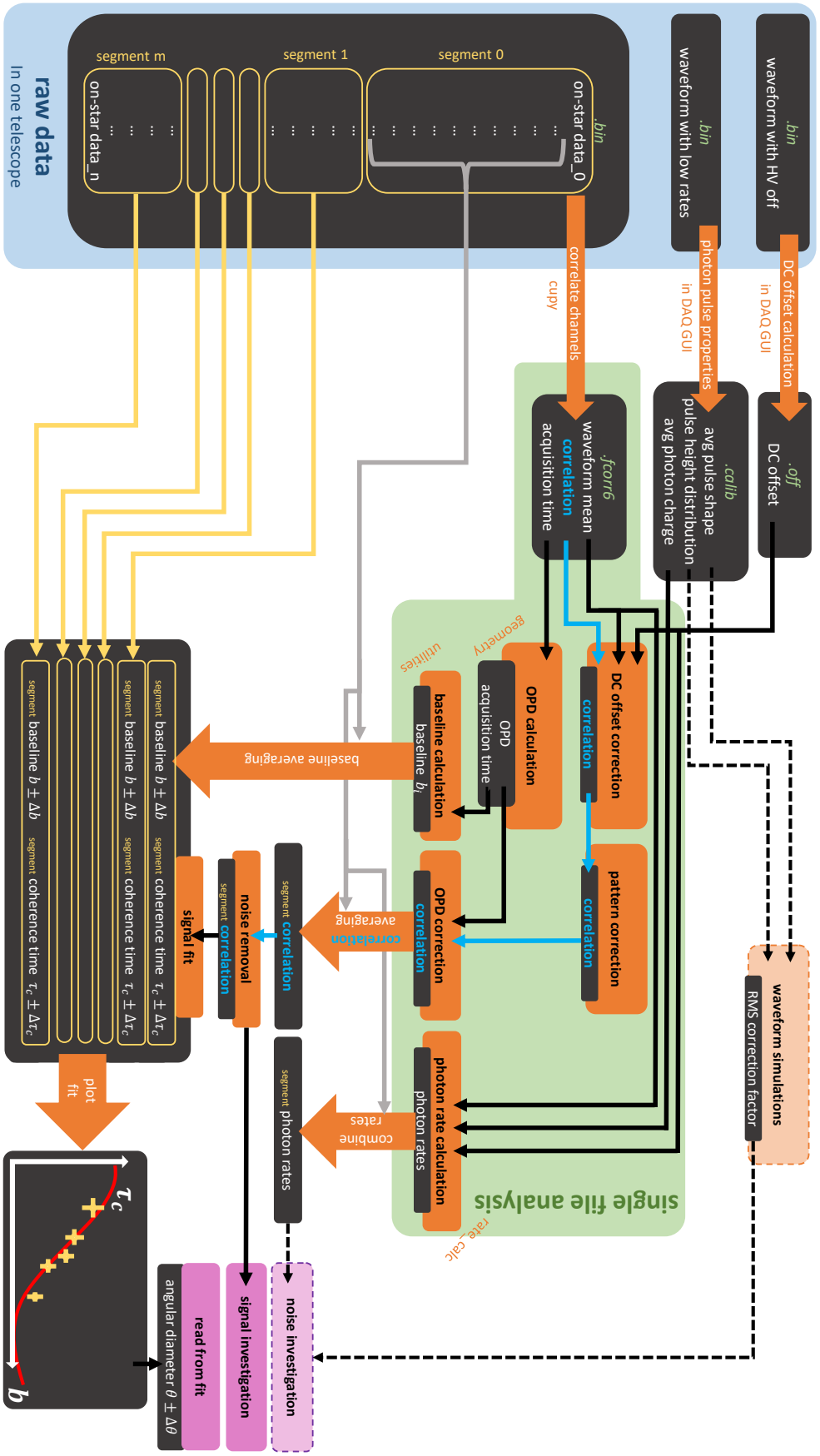

Figure 6.2: Extended analysis pipeline for the usage at H.E.S.S.. Dashed arrows and fields indicate actions that are not performed routinely any more, but only for occasional checks.

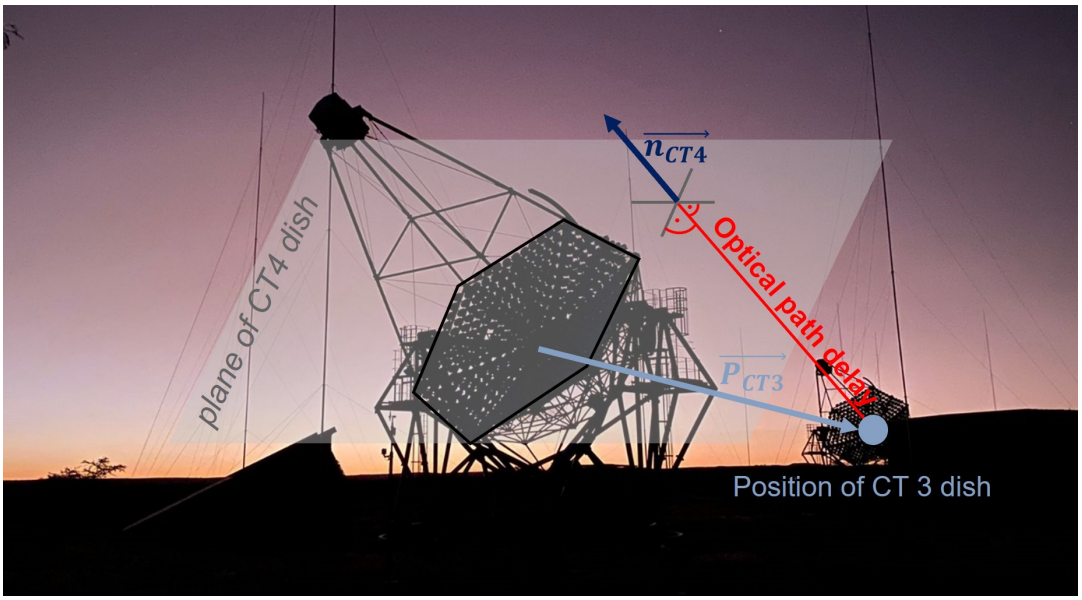

Figure 6.3: Geometry for the optical path length correction

As briefly described in section 5.7 of the publication, there are two counteracting aspects concerning the perfect segment length. The longer the segment size is, the higher the signal-to-noise of the observed photon bunching peak in that segment, and thus the smaller the uncertainty on the determination of the coherence time. On the other hand, long segment sizes correlate with the star moving significantly in the night sky, and the range of projected baselines within one segment is becoming larger, resulting in a larger error bar for the baseline of that segment. A good compromise can be found by iteratively changing the segment sizes, e.g. starting at small segments and increasing the sizes until the bunching peaks become significant enough for a proper analysis.

6.5 Optical Path Delay Correction

Another additional issue that has to be accounted for with on-sky measurements is the continuously changing optical path delay (OPD) between the two telescopes. Just as the projected baseline changes over time in a measurement when both telescopes track the same source, so does the path length difference that initially coincident photons need to travel to arrive at the different telescopes. Since the telescopes are 120 m apart, this optical path delay time can be on the order of several hundreds of nanoseconds, depending on the exact pointing direction. A correction for this effect needs to be applied to the data, not only because this delay is shifting the position of the correlation peak in the $g^{(2)}$ function for a certain measurement segment. A change in optical path delay within one measurement segment results in a washing out of the correlation peak if not accounted for. For faint targets a measurement segment has to be chosen rather long in order to gain enough statistics for a peak analysis. However, long measurement times result in the correlation peak being washed out even further.

The optical path delay distance for an arbitrary telescope pointing direction can be calculated with the help of figure 6.3.

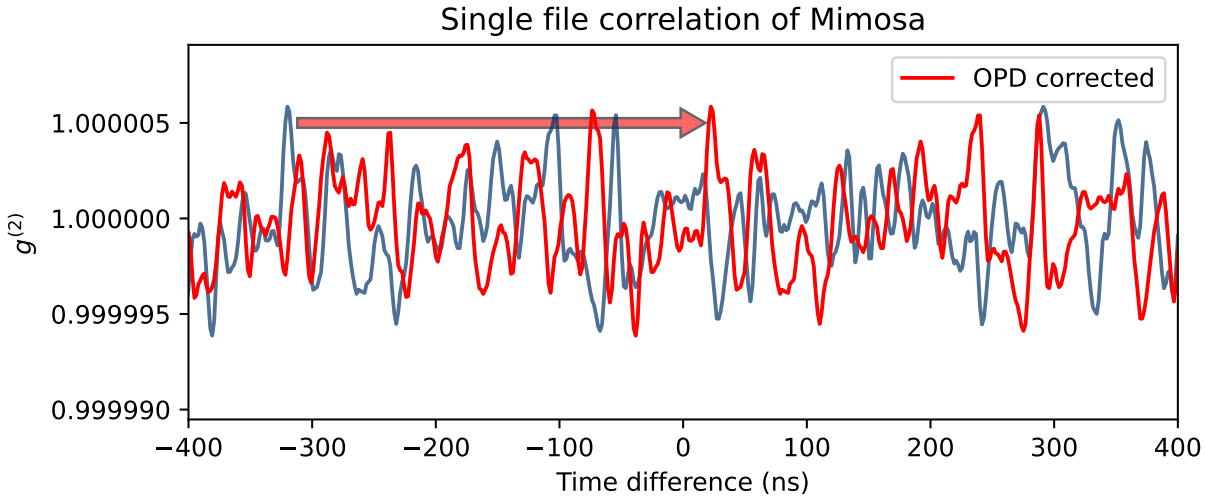

Figure 6.4: Optical path delay correction in a single data file. The arrow displays the shift of the correlation with the help of an exemplary noise peak.

In this example, the telescopes are pointing mainly southwards, which results in the light from the star arriving at the front telescope (CT4) first. The light grey plane symbolizes the plane defined by the mirror dish of CT4, more precisely the border of the (curved) dish. This plane is perpendicular to the pointing direction of the telescope and its orientation changes in time. The additional path a photon has to travel to reach CT3 can be obtained by computing the distance of the aforementioned plane to the position of the CT3 dish, which is not changing in time. This quantity can be calculated by the product of the norm vector defining the CT4 plane (this vector is facing towards the source position) and the position vector of the CT3 dish (defined from the position of the CT4 dish).

$$\Delta l = -\vec{n}_{\mathrm{CT4}} \cdot \vec{P}_{\mathrm{CT3}} \tag{6.1}$$

An additional minus sign was added to account for the correct definition of the path delay: if the vectors span an angle $> 90°$, as it is the case in figure 6.3, the vector product is negative, but the difference in arrival times of photons of the same wavefront $\Delta t = t_{\mathrm{CT3}} - t_{\mathrm{CT4}}$ is positive.

The OPD is calculated for every single correlation file. The correlation function is shifted by the number of time bins corresponding to the OPD before the averaging process of all correlation files. Figure 6.4 shows an exemplary single file $g^{(2)}$ function from a measurement of the star Mimosa (β Cru) in 2023. The time shift is made apparent by the arrow in the plot.

Figure 6.5 shows the $g^{(2)}$ function of one measurement segment of Mimosa for both the uncorrected as well as for the OPD corrected case. In the uncorrected data the correlation peak is positioned at a negative time difference. It is also visible how the correlation peak is broadened, and as a consequence reduced in signal height (and signal-to-noise). The OPD correction is shifting the peak position close to zero time difference. The small remaining deviation can be explained by a small difference in signal cable lengths.

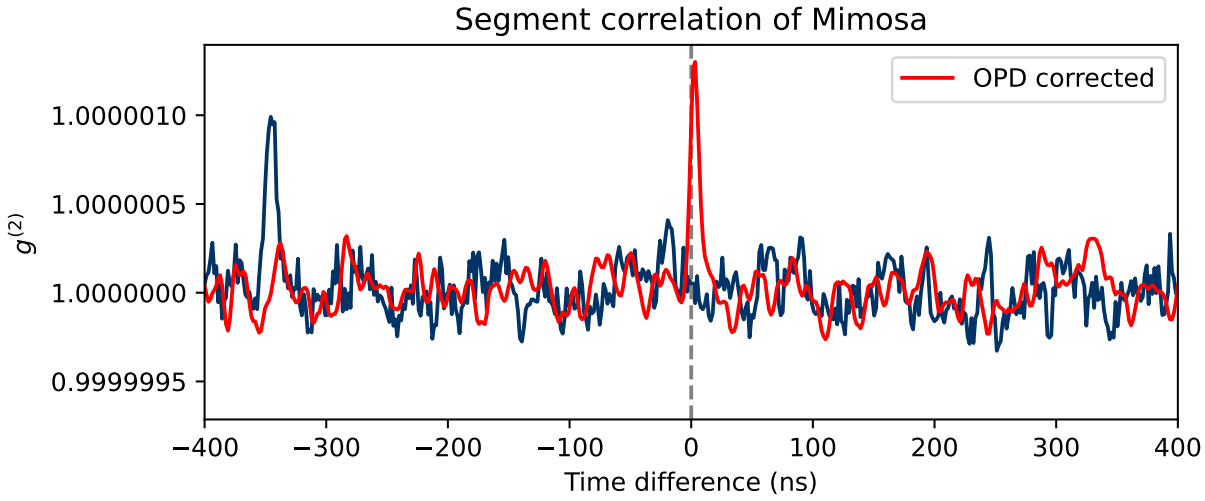

Figure 6.5: Optical path delay correction for a complete measurement segment.

6.6 Publication: First Intensity Interferometry Measurements With The H.E.S.S. Telescopes

The publication has been published as a journal article in the Monthly Notices of the Royal Astronomical Society

First intensity interferometry measurements with the H.E.S.S. telescopes

Volume 527, Issue 4, February 2024, Pages 12243-12252
https://doi.org/10.1093/mnras/stad3676

The authors are Andreas Zmija, Naomi Vogel, Frederik Wohlleben, Gisela Anton, Adrian Zink and Stefan Funk.

First author's contribution (Andreas Zmija) Andreas developed major parts of the analysis pipeline, which contains the complete analysis of the measurement data from the pure correlation data to the final spatial coherence curves and angular diameter fits, except for the data cleaning algorithms (noise cuts). Together with Naomi Vogel and Frederik Wohlleben he executed the measurement campaign, including setting up major parts of the equipment and taking the data. He developed the software for data acquisition and synchronization.
Andreas wrote abstract, part of the introduction (section 1), the theory section (section 2), and the last paragraph in section 3.2 concerning the digitization. He observed the night sky background behaviour of section 4.3, and is main contributor to chapter 5 (except for the noise cuts in section 5.2). Conclusion and outlook (section 6) were discussed and written together with Naomi Vogel.

Co-authors' contributions Naomi Vogel was planning and testing major parts of the motorized mechanical setup. She developed the software for the motors together with Frederik Wohlleben, who specialized on the online pointing correction algorithm resulting in section 4.1 and figure 5. Naomi wrote parts of the introduction. She is the main contributor to chapter 3 and furthermore contributed with writing sections 4, 4.1, 4.2 and 4.4. She provided the calculation and plotting of the photon rates seen in figure 7. In chapter 5 she performed data cleaning, which is described in section 5.2. Adrian Zink provided most of the electronics for the setup, which includes the power supply electronics for the photomultipliers, amplifiers, the PCIe boards and the motor control boards. He also provided the software for the correlation procedure (see section 5.1). Together with Andreas Zmija, Naomi Vogel and Frederik Wohlleben executed the measurement campaign, including setting up major parts of the equipment and taking the data. All the authors contributed with valuable ideas and discussions for the development of the project, as well as proof reading of the paper draft.

6.7 Signal-To-Noise With Background Photons

The measurements at the H.E.S.S. telescopes contain a significant amount of photons coming from sources other than the observed star, denoted to as night sky background, which have to be considered as background. The ratio of background to signal photons is still less than 5 % in every measurement, however, if fainter stars will be measured in the future, the relative background photon rate will increase and effects of the night sky background to the interferometer must be considered.

Background photons increase the random number of photon pairs at arbitrary time bins τ, and by that reduce the relative number of bunching photon pairs. Again assuming equal photon rates in the detectors, the rates can be divided into signal photon rates R_S and background rates R_B.

$$R = R_\mathrm{S} + R_\mathrm{B} = R_\mathrm{S}(1 + Q) \tag{6.2}$$

defining $Q = {}^{R_\mathrm{B}}/_{R_\mathrm{S}}$ as the ratio between background and signal photon rates. While photon bunching only appears from R_S photons, random coincidences appear between both signal and background photons. This results in an effective decrease of the bunching peak height in the $g^{(2)}$ function. One can quantify this effect from an experimental point of view: the number of bunching photon pairs P_B is a fraction $\epsilon \propto \tau_c$ of the random photon pairs C, as defined in equation 3.11, where $C = C_\mathrm{S}$ is restricted to the photon pairs coming from signal photons.

$$P_\mathrm{B} = \epsilon \cdot C_\mathrm{S} = \epsilon \cdot {R_\mathrm{S}}^2 \delta_\tau T \tag{6.3}$$

When neglecting background photons the $g^{(2)}$ function is calculated by division of C_S, whereas the number of random photon events including background photons is increased to $C_\mathrm{S+B}$.

$$C_\mathrm{B+S} = R^2 \delta_\tau T = {R_\mathrm{S}}^2 (1 + Q)^2 \delta_\tau T \tag{6.4}$$

While signal-to-noise without background is proportional to ${P_\mathrm{B}}/{\sqrt{C_\mathrm{S}}}$, including the background it is proportional to ${P_\mathrm{B}}/{\sqrt{C_\mathrm{S+B}}}$:

$$S/N \propto \frac{\tau_c {R_\mathrm{S}}^2 \delta_\tau T}{\sqrt{{R_\mathrm{S}}^2 (1+Q)^2 \delta_\tau T}} = \frac{\tau_c R_\mathrm{S}}{1+Q}\sqrt{\delta_\tau T} \tag{6.5}$$

Rearranging this equation for T gives

$$T \propto \frac{{S/N}^2 (1+Q)^2}{\tau_c^2 {R_\mathrm{S}}^2 \delta_\tau} \tag{6.6}$$

to find the measurement time necessary to detect a bunching signal at a given signal-to-noise. Due to background photons T increases by the factor $(1+Q)^2$.

Implications of night sky background to the H.E.S.S. intensity interferometer

For the stars measured in the first campaign, the background rate ratio did not exceed $Q = 5\,\%$, resulting in a less than 10 % increase of the necessary measurement time. For fainter stars, however, the signal photon rates will decrease, while the night sky background rate remains constant (if the night conditions are the same). According to equation 4.6 the signal rates decrease by $\approx 60\,\%$ per apparent magnitude of the star. Table 6.1 lists the increase in necessary measurement time to detect the bunching signal with a given signal-to-noise, compared to the ideal situation without background photons. Here $Q = 0.05$ is considered for a magnitude-2 star (e.g. Nunki) at low elevations.

m_v	Q	T/T_0
1	0.02	1.04
2	0.05	1.10
3	0.13	1.28
4	0.32	1.74
5	0.79	3.20
6	1.99	8.94

Table 6.1: Effects of night sky background on measurements of stars. m_v is the apparent stellar magnitude, Q the ratio of night sky background to star photons, and T/T_0 the increase in measurement time to detect a bunching signal of a given signal-to-noise compared to the case of no background photons.

Note that T/T_0 acts in addition to the fact that signal-to-noise is already decreasing for fainter stars because of the decreasing photon flux $n(\lambda)$ (see equation 3.18), making measurements of fainter stars even less feasible. Limitations of intensity interferometry observations of bright targets remains to be an issue also for IACTs, and advancing the measurements towards fainter targets raises the quest for observations during dark time, which is a strong argument for a dedicated stellar intensity interferometer in the future.

CHAPTER 7

Summary and Prospects

7.1 Recap of the Long Road to the H.E.S.S. Intensity Interferometer

In chapter 6, the first intensity interferometry measurement results with the H.E.S.S. telescopes are published. These recent results conclude the work around this thesis, which - apart from the initial work summarized in [48] - describes the entire process of intensity interferometry research at the *Erlangen Centre for Astroparticle Physics*, which started in summer 2017.

Laboratory experiments were always performed with two photomultipliers separated through a beamsplitter. This way zero-baseline correlations were recorded. The spatial coherence is only reduced by the size of the coherence cell of the light source in the observation plane being on the same order as the interferometer's aperture. In chapter 3 the first approach for measuring the bunching signals of thermal light sources made use of photon time-tagging electronics, recording the arrival times of single photon events in both detectors. The arrival times were correlated to detect the excess of coincident w.r.t randomly in time distributed photon pairs. The treatment of photons as single counts in the detector allowed for a straight forward discussion of the theoretical expectations regarding the signal's shape and the stochastic noise contributions, which follow Poissonian statistics. A mercury discharge lamp, where the narrow emission lines result in high coherence times, was used for initial tests of the interferometer, before an LED with a broad emission spectrum served as simulation of starlight, where the light was actively optically filtered in the interferometer. With the help of reference measurements using a spatially incoherent light bulb, the measurement results were consistent with statistical expectations and the interferometer was understood quantitatively. As an additional finding, the convenience of using LEDs as thermal light sources was demonstrated.

Given that the combination of the used photomultipliers and photon time-tagging electronics was not able to record photon rates significantly above 10 MHz, a requirement essential for measuring bright stars with huge telescopes, the setup was changed in chapter 4 into a system

which continuously records the photomultiplier currents in both channels, the waveforms, which were correlated afterwards. The detection of multiple overlapping photons in the same channel was now possible and therefore eliminated the upper limit on detectable photon rates. The new system, however, required an improved understanding of the measured correlation, as the extended photon pulse shapes in the waveforms resulted in the correlation of neighbouring time bins in the $g^{(2)}$ function. This effect acts on the correlation effectively as a low-pass filter, decreasing both the signal and the noise, but leaving signal-to-noise constant. New analysis techniques for a comprehensive quantitative understanding include the execution of offset and calibration measurements to characterize the photomultipliers for each measurement. With these new methods it was shown that also the new interferometer was able to be operated at the theoretical signal-to-noise limit, meaning that the photon bunching signal as well as the noise behaved according to expectations and no systematic noise contributions were detected. A xenon lamp was used as a thermal light source, which is able to provide a much higher photon flux compared to commercial LEDs. In contrast to the time-tagging measurements from chapter 3, the necessary measurement time for a highly significant detection of the bunching peaks decreased from 40 hours to 30 minutes due to the much higher photon rates.

While the working group concluded for the specific case of intensity interferometry at IACTs that current-correlation systems are better suited than time-tagging of single photons, this statement can not be generalized. With very high time resolution electronics it would be possible to compete with the large collection areas of IACTs in terms of signal-to-noise, even on smaller optical telescopes. As this approach is followed by a collaborative working group, a comparison of both intensity interferometry systems was performed in chapter 5, measuring the same light source (again a xenon lamp). While both interferometers operated close to the shot noise limit, a higher significance was detected in the *HPR* (high photon rate) system than in the *HTR* (high time resolution) system. The difference lies in the actively attenuated photon flux for HTR in order not to exceed the count rate limit of the current detector generation. But as it was discussed the current development of new detector systems may indeed allow for intensity interferometry measurements on small optical telescopes that can compete with IACT installations.

Eventually in chapter 6 the HPR setups were installed at two of the H.E.S.S. Phase I telescopes. Additional components in hardware and software were necessary in order to measure the light from the stars and detect the photon correlations. On the hardware side these include the motorized elements which enabled a remote adjustment of the optical elements while the telescopes were tracking the targets, while in the software the optical path delay correction, among other things, had to be implemented. The interferometer was able to detect the bunching signals in the starlight of various stars and star systems. The angular diameter of the Star Nunki (σ Sgr) was determined from the spatial coherence curve, and estimations of the angular diameters of the two main components of the system Shaula (λ Sco) were given. Latter system, however, can not be treated as single star and the angular diameter estimations should be read with care. The spatial coherence curve of the system Acrux (α Cru) was also presented, but due to it being a multiple star system, no angular diameter estimation was performed. Besides these successful measurements, there remain open questions, the greatest being why the coherence times measured with H.E.S.S. are almost a factor 4 smaller than expected and measured in the lab.

7.2 Science Cases of the H.E.S.S. Intensity Interferometer

While the first intensity interferometry measurement campaign at the H.E.S.S. telescopes concludes this PhD project, it definitely doesn't conclude the efforts of the working group, aiming for improvements and new measurements with H.E.S.S.. A second campaign was already executed in April/May 2023, the results of which will be published. Until the inauguration of the CTA Southern array, H.E.S.S. remains the only IACT array on the southern hemisphere, which complements the list of stars yet to be measured by intensity interferometry with VERITAS or MAGIC. The analysis techniques of spatial coherence curves are currently concentrated on measuring single stars with assumed uniform disk diameters. As a first step to improving this analysis, it is reasonable to get familiarized with the concept of limb-darkening for a more advanced interpretation of single-star spatial coherence curves [116, 117]. Analysis techniques for extracting orbital as well as stellar parameters of binary or multiple star systems open up additional science cases for the intensity interferometer.

Besides the commissioning of a third telescope for intensity interferometric observations, the biggest innovation in the second campaign is the extension to simultaneous two-color measurements with the interferometer. Instead of measuring the zero-baseline correlation, the two arms of the beamsplitter have the option of featuring different optical band-pass filters, so that the angular extent of stars is measured in different wavelength bands at the same time. This can be interesting for common stars in case different angular diameters are detected, but is especially exciting for systems that show characteristic features in specific wavelengths. A famous example is γ^2 Velorum, a binary system consisting of a *Wolf-Rayet star* and a *blue supergiant* [118]. Wolf-Rayet stars are known for having strong emission lines dominating the spectra [119], such as the Carbon emission line at 465 nm. Hanbury Brown et. al. in fact studied this system, measuring in the emission line as well as in the continuum of the common spectrum (at 443 nm). They found that the system's angular size in the continuum is different to the one in the emission region, which was identified with the size of the critical Roche lobe around the Wolf-Rayet star [120]. Precise measurements with the H.E.S.S. intensity interferometer in two colors simultaneously could confirm these observations and constrain the obtained parameters of this and other systems further.

The current (temporal) intensity interferometry installations at H.E.S.S. are limited to the Phase I telescopes. Including the Phase II telescope *CT5* into the interferometer would on the one hand enable an increased sensitivity towards larger objects, given that CT5 is positioned in the center of the array, which provides smaller baselines in combination with the Phase I telescopes. But on the other hand it also offers the option of exploring possibilities on how to implement intensity interferometry directly into the *FlashCam* camera, the Cherenkov camera design that is currently installed at CT5 and planned to be installed at the *Medium Sized Telescopes* of CTA [121]. An equipment of the FlashCam camera with intensity interferometry electronics at H.E.S.S. can lead the way for implementation into CTA.

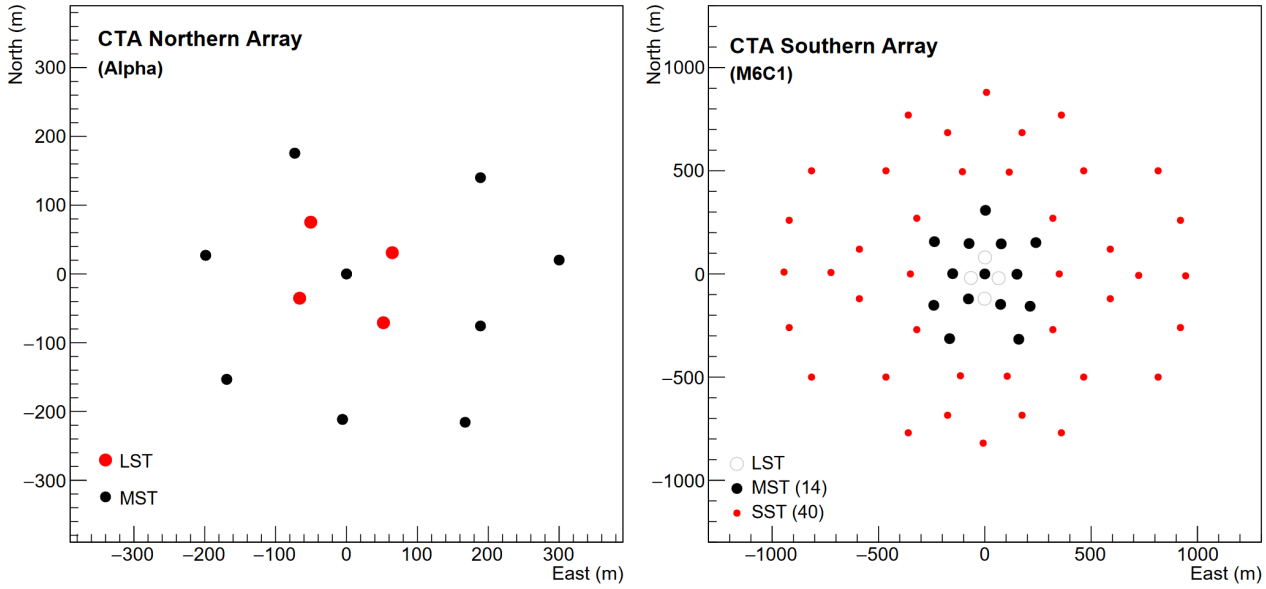

Figure 7.1: Potential configurations of the northern and southern array sites of CTA. Image taken from [122].

7.3 Intensity Interferometry With Future Telescopes

As mentioned before, while the current generation of IACTs do not provide baselines long enough to improve in angular resolving power in contrast to modern amplitude interferometers, the next generation will: the Cherenkov Telescope Array, currently in construction. With two locations, one on La Palma in the northern (CTA-N), and one in Chile in the southern hemisphere (CTA-S), it will consist of three different types of telescopes, Large- (LST), Medium- (MST), and Small-Sized Telescopes (SST). Figure 7.1 shows a potential layout for both sites.

While the northern array will contain maximum baselines on the order of 500 m using the MSTs, observations with the SSTs on the southern site span baselines of up to 2 km. In addition to the huge number of potential instantaneous baselines (40 SSTs and 14 MSTs together would form $54 \cdot 53/2 = 1431$ simultaneous baselines, of which some, however, are most likely identical), access to these large baselines extend current angular resolution limits in the optical by an order of magnitude, as visualized in figure 7.2.

Work towards implementation of intensity interferometry into CTA is currently in progress. The MAGIC collaboration plans to perform measurements in the near future, combining the two MAGIC telescopes with the LST prototype of the northern CTA array, which is located next to the MAGIC telescopes, and as a next step expand the interferometer to the other upcoming CTA-N LSTs [85]. The development of an intensity interferometry module for the *ASTRI Mini-Array* [124], which is being built using the same telescope design as for the SSTs in CTA, is in principle a proof of concept for SST intensity interferometry observations. If an implementation into H.E.S.S. CT5 will be realized as well, concepts for all the different telescope or camera designs which will be in use at CTA show their capability of adding intensity interferometry as an additional science case to the array. Observations can certainly be performed during the moonlight breaks of the gamma-ray measurements, but also potential

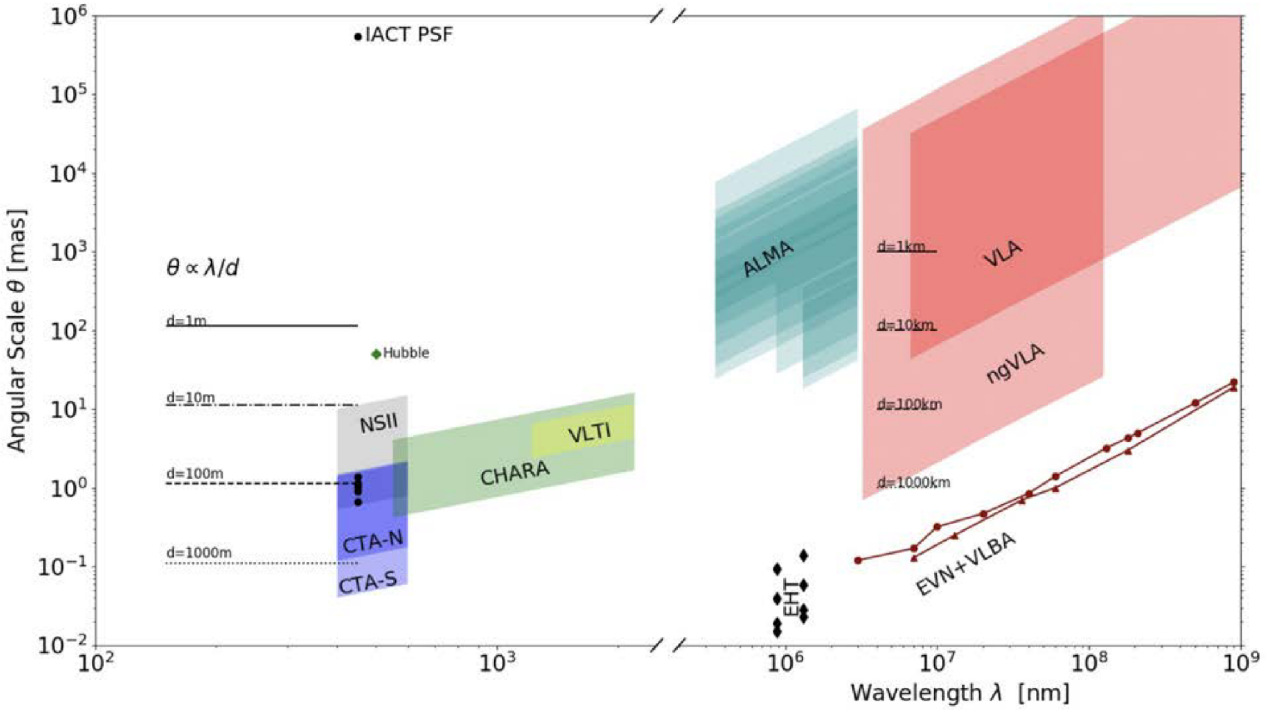

Figure 7.2: Angular resolution limits of various interferometers for the different wavelengths, on the left optical and infrared and on the right radio wavelengths. The blue dots within the regime of CTA-N are the different VERITAS baselines. Image taken from [123].

sub-configurations of the arrays could be considered for simultaneous gamma-ray and intensity interferometry observations during dark night times.

At wavelengths close to UV, say $\lambda = 350\,\mathrm{nm}$, the largest CTA-S baselines would enable angular resolutions on the order of 40 µas. This resolution is visualized in figure 7.3, where a hypothetical planet is transiting the close star Sirius. Given the relatively small general signal-to-noise in intensity interferometry in combination with the CTA largest baselines being produced by the smallest telescopes (the SSTs), the realization of this amount of detail in an image formed by CTA intensity interferometry observations can be questioned. However, prospects and images like these lubricate the gears of science and scientists around the world, who keep pushing the physical and technical limits to the extreme, and with the next generations of photo-detectors, electronics and PhD students, nobody can predict the magnificent discoveries that an intensity interferometry-friendly scientific community will make.

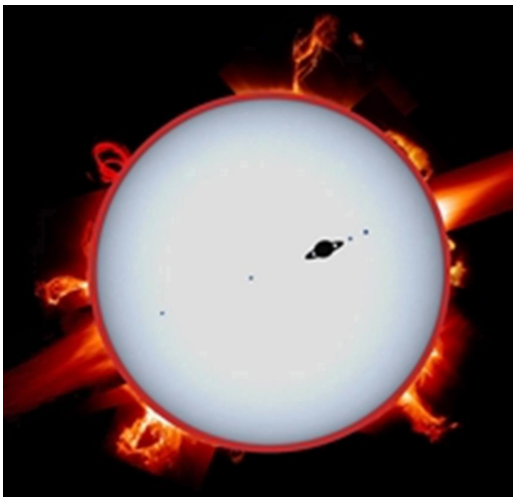

Figure 7.3: A simulated image of a hypothetical planet with four moons transiting the star Sirius with an angular resolution of 40 µas. Image taken from [125].

Bibliography

[1] Robert Hanbury Brown and Richard Q Twiss. "A test of a new type of stellar interferometer on Sirius". In: *Nature* 178 (1956), pp. 1046–1048.

[2] R Hanbury Brown and RQ Twiss. "Interferometry of the intensity fluctuations in light IV. A test of an intensity interferometer on Sirius A". In: *Proceedings of the Royal Society of London. Series A. Mathematical and Physical Sciences* 248.1253 (1958), pp. 222–237.

[3] R Hanbury Brown. "Stellar interferometer at Narrabri observatory". In: *Nature* 218.5142 (1968), pp. 637–641.

[4] R Hanbury Brown, J Davis, and LR Allen. "The angular diameters of 32 stars". In: *Monthly Notices of the Royal Astronomical Society* 167.1 (1974), pp. 121–136.

[5] WJ De Wit et al. "Towards micro-arcsecond spatial resolution with Air Cherenkov Telescope arrays as optical intensity interferometers". In: *arXiv preprint arXiv:0811.2377* (2008).

[6] Stephan LeBohec et al. "Toward a revival of stellar intensity interferometry". In: *Optical and infrared interferometry*. Vol. 7013. SPIE. 2008, pp. 774–783.

[7] Dainis Dravins. "Intensity interferometry: optical imaging with kilometer baselines". In: *Optical and Infrared Interferometry and Imaging V*. Vol. 9907. SPIE. 2016, pp. 128–139.

[8] W Guerin et al. "Temporal intensity interferometry: photon bunching in three bright stars". In: *Monthly Notices of the Royal Astronomical Society* 472.4 (2017), pp. 4126–4132.

[9] Luca Zampieri et al. "Stellar intensity interferometry of Vega in photon counting mode". In: *Monthly Notices of the Royal Astronomical Society* 506.2 (2021), pp. 1585–1594.

[10] Sebastian Karl, Stefan Richter, and Joachim von Zanthier. "Temporal Intensity Interferometry at a 0.5 m Telescope". In: *arXiv preprint arXiv:2303.13265* (2023).

[11] AU Abeysekara et al. "Demonstration of stellar intensity interferometry with the four VERITAS telescopes". In: *Nature Astronomy* 4.12 (2020), pp. 1164–1169.

[12] VA Acciari et al. "Optical intensity interferometry observations using the MAGIC Imaging Atmospheric Cherenkov Telescopes". In: *Monthly Notices of the Royal Astronomical Society* 491.2 (2020), pp. 1540–1547.

[13] Robert Hanbury Brown. "The intensity interferometer; its application to astronomy". In: *London* (1974).

[14] S LeBohec and J Holder. "Using ACT arrays as Intensity Interferometers". In: *arXiv preprint astro-ph/0507010* (2005).

[15] S Le Bohec and J Holder. "Optical intensity interferometry with atmospheric Cerenkov telescope arrays". In: *The Astrophysical Journal* 649.1 (2006), p. 399.

[16] Dr. David R. Williams. *Moon Fact Sheet (Nasa)*. 2021. URL: https://nssdc.gsfc.nasa.gov/planetary/factsheet/moonfact.html (visited on 06/29/2023).

[17] Dr. David R. Williams. *Sun Fact Sheet (Nasa)*. 2022. URL: https://nssdc.gsfc.nasa.gov/planetary/factsheet/sunfact.html (visited on 06/29/2023).

[18] Dr. David R. Williams. *Jupiter Fact Sheet (Nasa)*. 2023. URL: https://nssdc.gsfc.nasa.gov/planetary/factsheet/jupiterfact.html (visited on 06/29/2023).

[19] Dr. David R. Williams. *Saturn Fact Sheet (Nasa)*. 2023. URL: https://nssdc.gsfc.nasa.gov/planetary/factsheet/saturnfact.html (visited on 06/29/2023).

[20] Dr. David R. Williams. *Mars Fact Sheet (Nasa)*. 2023. URL: https://nssdc.gsfc.nasa.gov/planetary/factsheet/marsfact.html (visited on 06/29/2023).

[21] RW Wilson et al. "High-resolution imaging of Betelgeuse and Mira". In: *Monthly Notices of the Royal Astronomical Society* 257.3 (1992), pp. 369–376.

[22] Dr. David R. Williams. *Pluto Fact Sheet (Nasa)*. 2023. URL: https://nssdc.gsfc.nasa.gov/planetary/factsheet/plutofact.html (visited on 06/26/2023).

[23] Daniel B Schmolze et al. "Advances in microscopy techniques". In: *Archives of pathology & laboratory medicine* 135.2 (2011), pp. 255–263.

[24] Lord Rayleigh. "XXXI. Investigations in optics, with special reference to the spectroscope". In: *The London, Edinburgh, and Dublin Philosophical Magazine and Journal of Science* 8.49 (1879), pp. 261–274.

[25] Jay C Bradley et al. "Dark-adapted pupil diameter as a function of age measured with the NeurOptics pupillometer". In: *Journal of refractive surgery* 27.3 (2011), pp. 202–207.

[26] Ronald L Gilliland and AK Dupree. "First image of the surface of a star with the Hubble Space Telescope". In: *The Astrophysical Journal* 463.1 (1996), p. L29.

[27] Christopher J Burrows et al. "The imaging performance of the Hubble Space Telescope". In: *Astrophysical Journal, Part 2-Letters (ISSN 0004-637X), vol. 369, March 10, 1991, p. L21-L25.* 369 (1991), pp. L21–L25.

[28] Michael Hart, Simone Esposito, and Sebastian Rabien. *Adaptive Optics at the World's Biggest Optical Telescope*. Tech. rep. ARIZONA UNIV TUCSON, 2010.

[29] J Gorosabel et al. "Observing GRB afterglows, SNe and their host galaxies with the 10.4 m Gran Telescopio Canarias (GTC)". In: *European Astronomical Society Publications Series* 61 (2013), pp. 235–239.

[30] Matt Johns et al. "Giant magellan telescope: overview". In: *Ground-based and Airborne Telescopes IV* 8444 (2012), pp. 526–541.

[31] Jerry Nelson and Gary H Sanders. "The status of the Thirty Meter Telescope project". In: *Ground-based and Airborne Telescopes II*. Vol. 7012. SPIE. 2008, pp. 504–521.

[32] Roberto Gilmozzi and Jason Spyromilio. "The European extremely large telescope (E-ELT)". In: *The Messenger* 127.11 (2007), p. 3.

[33] Dainis Dravins et al. "Stellar intensity interferometry: Prospects for sub-milliarcsecond optical imaging". In: *New Astronomy Reviews* 56.5 (2012), pp. 143–167.

[34] A. A. Michelson and F. G. Pease. "Measurement of the Diameter of α Orionis with the Interferometer." In: *Astrophysical Journal* 53 (May 1921), pp. 249–259. DOI: 10.1086/142603.

[35] Albert A Michelson. "I. On the application of interference methods to astronomical measurements". In: *The London, Edinburgh, and Dublin Philosophical Magazine and Journal of Science* 30.182 (1890), pp. 1–21.

[36] Albert A Michelson and Francis G Pease. "Measurement of the diameter of Alpha-Orionis by the interferometer". In: *Proceedings of the National Academy of Sciences* 7.5 (1921), pp. 143–146.

[37] Anthony Mark Fox. *Quantum optics: an introduction*. Vol. 15. Oxford University Press, USA, 2006.

[38] Cedric Foellmi. "Intensity interferometry and the second-order correlation function in astrophysics". In: *Astronomy & Astrophysics* 507.3 (2009), pp. 1719–1727.

[39] Pieter Hendrik van Cittert. "Die wahrscheinliche Schwingungsverteilung in einer von einer Lichtquelle direkt oder mittels einer Linse beleuchteten Ebene". In: *Physica* 1.1-6 (1934), pp. 201–210.

[40] Frederik Zernike. "The concept of degree of coherence and its application to optical problems". In: *Physica* 5.8 (1938), pp. 785–795.

[41] Max Born and Emil Wolf. *Principles of optics: electromagnetic theory of propagation, interference and diffraction of light*. Elsevier, 2013, pp. 499–509.

[42] J Davis, WJ Tango, and AJ Booth. "Limb-darkening corrections for interferometric uniform disc stellar angular diameters". In: *Monthly Notices of the Royal Astronomical Society* 318.2 (2000), pp. 387–392.

[43] Antoine Labeyrie, Stephen G Lipson, and Peter Nisenson. *An introduction to optical stellar interferometry*. Cambridge University Press, 2006.

[44] Markus Schöller. "The very large telescope interferometer: current facility and prospects". In: *New Astronomy Reviews* 51.8-9 (2007), pp. 628–638.

[45] TA Ten Brummelaar et al. "First results from the CHARA array. II. A description of the instrument". In: *The Astrophysical Journal* 628.1 (2005), p. 453.

[46] Ibrahim Abdulhalim. "Spatial and temporal coherence effects in interference microscopy and full-field optical coherence tomography". In: *Annalen der Physik* 524.12 (2012), pp. 787–804.

[47] Leonard Mandel and Emil Wolf. *Optical coherence and quantum optics*. Cambridge university press, 1995, pp. 56–59.

[48] Andreas Zmija. "Design and characterization of an intensity interferometer with thermal light sources". MA thesis. Friedrich-Alexander-Universität Erlangen-Nürnberg, 2018.

[49] CHARA. *Basics of Interferometry*. URL: https://www.chara.gsu.edu/public/basics-of-interferometry (visited on 07/06/2023).

[50] Theo Armand ten Brummelaar et al. "Update on the CHARA array". In: *Interferometry for Optical Astronomy II*. Vol. 4838. SPIE. 2003, pp. 69–78.

[51] Konrad RW Tristram. "Mid-infrared interferometry of nearby Active Galactic Nuclei". PhD thesis. 2007.

[52] Peter Marley Chingaipe et al. "High-contrast detection of exoplanets with a kernel-nuller at the VLTI". In: *arXiv preprint arXiv:2304.14193* (2023).

[53] Arsen R Hajian et al. “Direct confirmation of stellar limb darkening with the Navy Prototype Optical Interferometer”. In: *The Astrophysical Journal* 496.1 (1998), p. 484.

[54] Éric Thiébaut. “Principles of image reconstruction in interferometry”. In: *European Astronomical Society Publications Series* 59 (2013), pp. 157–187.

[55] Éric Thiébaut and John Young. “Principles of image reconstruction in optical interferometry: tutorial”. In: *JOSA A* 34.6 (2017), pp. 904–923.

[56] John Davis and William Tango. “Measurement of the atmospheric coherence time”. In: *Publications of the Astronomical Society of the Pacific* 108.723 (1996), p. 456.

[57] M Shao and MM Colavita. “Long-baseline optical and infrared stellar interferometry”. In: *Annual Review of Astronomy and Astrophysics* 30.1 (1992), pp. 457–498.

[58] David Buscher. “The optical error budget for the MRO Interferometer”. In: (2007).

[59] David F Buscher et al. “The conceptual design of the Magdalena ridge observatory interferometer”. In: *Journal of Astronomical Instrumentation* 2.02 (2013), p. 1340001.

[60] RJ Dorn et al. “NAOMI—A New Adaptive Optics Module for Interferometry”. In: *The Messenger* 156 (2014), pp. 12–15.

[61] Robin Arsenault et al. “MACAO-VLTI: an adaptive optics system for the ESO Interferometer”. In: *Adaptive Optical System Technologies II*. Vol. 4839. SPIE. 2003, pp. 174–185.

[62] Theo A Ten Brummelaar et al. “Adaptive optics for the CHARA array”. In: *Adaptive Optics Systems III*. Vol. 8447. SPIE. 2012, pp. 1207–1216.

[63] Ellyn K Baines et al. “Fundamental parameters of 87 stars from the navy precision optical interferometer”. In: *The Astronomical Journal* 155.1 (2017), p. 30.

[64] Event Horizon Telescope Collaboration et al. “First M87 event horizon telescope results. IV. Imaging the central supermassive black hole”. In: *arXiv preprint arXiv:1906.11241* (2019).

[65] Kazunori Akiyama et al. “First Sagittarius A* Event Horizon Telescope results. IV. Variability, morphology, and black hole mass”. In: *The Astrophysical Journal Letters* 930.2 (2022), p. L15.

[66] FG Pease. “The new fifty-foot stellar interferometer”. In: *Scientific American* 143.4 (1930), pp. 290–293.

[67] DG Currie, SL Knapp, and KM Liewer. “Four stellar-diameter measurements by a new technique: amplitude interferometry.” In: *Astrophysical Journal, Vol. 187, p. 131-134* 187 (1974), pp. 131–134.

[68] R Hanbury Brown, RC Jennison, and MK Das Gupta. “Apparent angular sizes of discrete radio sources: Observations at jodrell bank, manchester”. In: *Nature* 170.4338 (1952), pp. 1061–1063.

[69] Peter Fellgett. “The question of correlation between photons in coherent beams of light”. In: *Nature* 179.4567 (1957), pp. 956–957.

[70] R Hanbury Brown, Richard Quinton Twiss, and givenName surName. “Interferometry of the intensity fluctuations in light-I. Basic theory: the correlation between photons in coherent beams of radiation”. In: *Proceedings of the Royal Society of London. Series A. Mathematical and Physical Sciences* 242.1230 (1957), pp. 300–324.

[71] R Hanbury Brown and RQ Twiss. "Interferometry of the intensity fluctuations in light. II. An experimental test of the theory for partially coherent light". In: *Proceedings of the Royal Society of London. Series A. Mathematical and Physical Sciences* 243.1234 (1958), pp. 291–319.

[72] Peter Grünwald. "Effective second-order correlation function and single-photon detection". In: *New Journal of Physics* 21.9 (2019), p. 093003.

[73] Rodney Loudon. *The quantum theory of light*. OUP Oxford, 2000.

[74] Dilleys Ferreira et al. "Connecting field and intensity correlations: The Siegert relation and how to test it". In: *American Journal of Physics* 88.10 (2020), pp. 831–837.

[75] Rodney Loudon. "Photon bunching and antibunching". In: *Physics Bulletin* 27.1 (1976), p. 21.

[76] R Hanbury Brown, J Davis, and LR Allen. "The stellar interferometer at Narrabri observatory—i: A description of the instrument and the observational procedure". In: *Monthly Notices of the Royal Astronomical Society* 137.4 (1967), pp. 375–392.

[77] R Hanbury Brown et al. "The stellar interferometer at Narrabri observatory—ii: The angular diameters of 15 stars". In: *Monthly Notices of the Royal Astronomical Society* 137.4 (1967), pp. 393–417.

[78] Manuel Bojer et al. "A quantitative comparison of amplitude versus intensity interferometry for astronomy". In: *New Journal of Physics* 24.4 (2022), p. 043026.

[79] John Davis and William J Tango. "New determination of the angular diameter of Sirius". In: *Nature* 323.6085 (1986), pp. 234–235.

[80] T Hassan and M Daniel. "Proving the outstanding capabilities of Imaging Atmospheric Cherenkov Telescopes in high time resolution optical astronomy". In: *36th International Cosmic Ray Conference (ICRC2019)*. Vol. 36. 2019, p. 692.

[81] R Hanbury Brown, J Davis, and LR Allen. "The Effects of Čerenkov Light Pulses on a Stellar Intensity Interferometer". In: *Monthly Notices of the Royal Astronomical Society* 146.4 (1969), pp. 399–409.

[82] JE Grindlay et al. "Results of a Southern-Hemisphere search for gamma-ray sources at energies of at least 300 GeV". In: *Astrophysical Journal, vol. 201, Oct. 1, 1975, pt. 1, p. 82-89. Research supported by the Smithsonian Institution, Australian Research Grants Committee, and University of Sydney* 201 (1975), pp. 82–89.

[83] JE Grindlay et al. "Evidence for the detection of gamma rays from Centaurus A at gamma-ray energies above 300 GeV". In: *Astrophysical Journal, vol. 197, Apr. 1, 1975, pt. 2, p. L9-L12. Research supported by the Smithsonian Institution, Australian Research Grants Committee, and University of Sidney* 197 (1975), pp. L9–L12.

[84] David B Kieda. "Performance of the upgraded VERITAS Stellar Intensity Interferometer (VSII)". In: *Optical and Infrared Interferometry and Imaging VIII*. Vol. 12183. SPIE. 2022, pp. 142–156.

[85] Juan Cortina et al. "First measurements and upgrade plans of the MAGIC intensity interferometer". In: *Optical and Infrared Interferometry and Imaging VIII*. Vol. 12183. SPIE. 2022, pp. 127–141.

[86] Rene A Ong, CTA Consortium, et al. "The Cherenkov Telescope Array Science Goals and Current Status". In: *EPJ web of conferences*. Vol. 209. EDP Sciences. 2019, p. 01038.

[87] Nolan Matthews et al. "Intensity interferometry at calern and beyond: progress report". In: *Optical and Infrared Interferometry and Imaging VIII*. Vol. 12183. SPIE. 2022, pp. 171–183.

[88] Nolan Matthews et al. "Intensity Interferometry Observations of the Hα Envelope of γCas with MéO and a Portable Telescope". In: *The Astronomical Journal* 165.3 (2023), p. 117.

[89] Yuanbo Deng and Daping Chu. "Coherence properties of different light sources and their effect on the image sharpness and speckle of holographic displays". In: *Scientific reports* 7.1 (2017), p. 5893.

[90] Elizabeth Newton et al. "Quantum secrecy in thermal states". In: *Journal of Physics B: Atomic, Molecular and Optical Physics* 52.12 (2019), p. 125501.

[91] Olivier Lai et al. "Intensity interferometry revival on the Côte d'Azur". In: *Optical and Infrared Interferometry and Imaging VI*. Vol. 10701. SPIE. 2018, pp. 599–610.

[92] DB Kieda et al. In: *PoS* ICRC2021 (2021), p. 710. DOI: 10.22323/1.395.0710.

[93] René Cornils et al. "Mirror alignment and performance of the optical system of the HESS imaging atmospheric Cherenkov telescopes". In: *FRONTIERS SCIENCE SERIES* 5 (2003), pp. 2875–2878.

[94] Hamamatsu. *H10770B-40 Specifications*. URL: https://neurophysics.ucsd.edu/Manuals/Hamamatsu/H10770B-40%20Specifications.PDF (visited on 08/02/2023).

[95] K Bernlöhr et al. "The optical system of the HESS imaging atmospheric Cherenkov telescopes. Part I: layout and components of the system". In: *Astroparticle Physics* 20.2 (2003), pp. 111–128.

[96] Dmitry A Orlov et al. "From single photon counting to high rate capability with fast timing MCP-PMTs for LIDAR". In: *Advanced Photon Counting Techniques XIII*. Vol. 10978. SPIE. 2019, pp. 93–100.

[97] Edwin Budding and Osman Demircan. *Introduction to astronomical photometry*. 6. Cambridge University Press, 2007.

[98] Eric Schulman and Caroline V Cox. "Misconceptions about astronomical magnitudes". In: *American Journal of Physics* 65.10 (1997), pp. 1003–1007.

[99] MS Bessell. "UBVRI photometry II: the Cousins VRI system, its temperature and absolute flux calibration, and relevance for two-dimensional photometry." In: *Publications of the Astronomical Society of the Pacific* 91.543 (1979), p. 589.

[100] Hamamatsu. *Photomultiplier Tubes R11265 U Series*. URL: https://www.hamamatsu.com/content/dam/hamamatsu-photonics/sites/documents/99_SALES_LIBRARY/etd/R11265U_H11934_TPMH1336E.pdf (visited on 07/17/2023).

[101] Université de Strasbourg/CNRS. *SIMBAD Astronomical Database*. URL: http://simbad.cds.unistra.fr/simbad/ (visited on 07/17/2023).

[102] WA Hiltner, RF Garrison, and RE Schild. "Mk spectral types for bright southern ob stars". In: *Astrophysical Journal, vol. 157, p. 313* 157 (1969), p. 313.

[103] Spectrum Instrumentation. *M4i.2212-x8 - 8 bit high speed digitizer*. URL: https://spectrum-instrumentation.com/products/details/M4i2212-x8.php (visited on 07/18/2023).

[104] Andreas Zmija et al. "LED as laboratory test source for astronomical intensity interferometry". In: *Optics Express* 28.4 (2020), pp. 5248–5256.

[105] Angelo Gulinatti et al. "Large-area avalanche diodes for picosecond time-correlated photon counting". In: *Proceedings of 35th European Solid-State Device Research Conference, 2005. ESSDERC 2005.* IEEE. 2005, pp. 355–358.

[106] A Fukasawa et al. "High speed HPD for photon counting". In: *IEEE Transactions On Nuclear Science* 55.2 (2008), pp. 758–762.

[107] Sebastian Karl et al. "Comparing different approaches for stellar intensity interferometry". In: *Monthly Notices of the Royal Astronomical Society* 512.2 (2022), pp. 1722–1729.

[108] Simon Archambault et al. "Gamma-ray observations under bright moonlight with VERITAS". In: *Astroparticle Physics* 91 (2017), pp. 34–43.

[109] Max L Ahnen et al. "Performance of the MAGIC telescopes under moonlight". In: *Astroparticle Physics* 94 (2017), pp. 29–41.

[110] Stefan Ohm, Stefan Wagner, HESS Collaboration, et al. "Current status and operation of the HESS array of imaging atmospheric Cherenkov telescopes". In: *Nuclear Instruments and Methods in Physics Research Section A: Accelerators, Spectrometers, Detectors and Associated Equipment* (2023), p. 168442.

[111] Naomi Vogel. personal communication. July 26, 2023.

[112] Georges Vasileiadis, HESS collaboration, et al. "The HESS experimental project". In: *Nuclear Instruments and Methods in Physics Research Section A: Accelerators, Spectrometers, Detectors and Associated Equipment* 553.1-2 (2005), pp. 268–273.

[113] Dirk Lennarz. "A study of transient very-high-energy gamma-ray emission from gamma-ray bursts and supernovae with HESS". PhD thesis. 2012.

[114] Sebastian Konrad. "Ray Tracing Simulation for Astro Quantum Optics". MA thesis. Friedrich-Alexander-Universität Erlangen-Nürnberg, 2021.

[115] Frederik Wohlleben. "Multidimensional Optimizations of Photon Flux by Alignment of the H.E.S.S. Astro Quantum Optics Setup". MA thesis. Friedrich-Alexander-Universität Erlangen-Nürnberg, 2022.

[116] R Hanbury Brown et al. "The effects of limb darkening on measurements of angular size with an intensity interferometer". In: *Monthly Notices of the Royal Astronomical Society* 167.3 (1974), pp. 475–484.

[117] D Hestroffer. "Centre to limb darkening of stars. New model and application to stellar interferometry." In: *Astronomy and Astrophysics, v. 327, p. 199-206* 327 (1997), pp. 199–206.

[118] JR North et al. "γ2 Velorum: orbital solution and fundamental parameter determination with SUSI". In: *Monthly Notices of the Royal Astronomical Society* 377.1 (2007), pp. 415–424.

[119] Paul A Crowther. "Physical properties of Wolf-Rayet stars". In: *Annu. Rev. Astron. Astrophys.* 45 (2007), pp. 177–219.

[120] R Hanbury Brown et al. "A study of γ 2 Velorum with a stellar intensity interferometer". In: *Monthly Notices of the Royal Astronomical Society* 148.1 (1970), pp. 103–117.

[121] Gerd Pühlhofer et al. "Science verification of the new FlashCam-based camera in the 28m telescope of HESS". In: *arXiv preprint arXiv:2108.02596* (2021).

[122] Orel Gueta. "The Cherenkov Telescope Array: layout, design and performance". In: *arXiv preprint arXiv:2108.04512* (2021).

[123] David B Kieda et al. "Astro2020 white paper state of the profession: Intensity interferometry". In: *arXiv preprint arXiv:1907.13181* (2019).

[124] Luca Zampieri et al. "A stellar intensity interferometry instrument for the ASTRI Mini-Array telescopes". In: *Optical and Infrared Interferometry and Imaging VIII*. Vol. 12183. SPIE. 2022, pp. 157–170.

[125] Dainis Dravins and Colin Carlile. "Kilometer-baseline optical intensity interferometry for stellar surface observations". In: *SPIE* (2016).

Acknowledgements

⚠ Achtung – Kitschgefahr ⚠

This thesis is the result of a continuous work over the time span of almost five years. During that time I have collaborated with various different colleagues. Some of them only for a certain time, others for the whole period of my PhD. I will not succeed in mentioning every one of them here, but I want to express my gratitude to all the people that gave input into and advice for my work and my scientific life. The people which I collaborated most closely, however, shall be mentioned below.

- **Stefan Funk,** der mir die nahezu einzigartige Gelegenheit gegeben hat, ein ganz neues Projekt aufzubauen, und der den perfekten Weg gefunden hat, mir sehr viele Freiräume zu geben, das Projekt zu entwickeln, und dabei aber dennoch Struktur in die Arbeit gebracht hat, sodass wir mit den ersten Intensitätsinterferometrie-Messungen bei H.E.S.S. unser großes Ziel – und das finale Ziel meiner Doktorarbeit – erreichen konnten.

- **Gisela Anton,** die wie eh und je vor Begeisterung sprüht, jede wissenschaftliche Diskussion einzugehen und durchzuexerzieren. Sie hat die große Fähigkeit, in einer Art wissenschaftliche Erkenntnisse zu vermitteln, auf Fehler hinzuweisen, und Vorschläge einzubringen, sodass stets die Wissenschaft im Vordergrund steht, und dass mir etwaige eigene Unwissenheit niemals unangenehm ist.

- **Adrian Zink** sei gedankt für sein Engagement in sämtlichen Bereichen unserer Forschung, vom Beisammensitzen über Code bis zum Frieren bei Teleskopmessungen in den kalten Winternächten, und für die gesunde Portion Pragmatismus, die so manches Problem im Handumdrehen lösen kann.

- **Frederik Wohlleben**, der eine essenziell wichtige Rolle bei unseren Messungen in Namibia eingenommen hat, von der Netzwerkeinrichtung bis zu nötigen Improvisations-Ingeneurarbeiten an unseren Setups. Darüber hinaus fügt er einem solchen Abenteuer noch einmal eine besondere Note hinzu – Namibia wäre nicht Namibia ohne eine ordentliche Portion Fredy!

- **Sebastian Karl**, **Stefan Richter** und **Joachim von Zanthier** für die sehr produktive Zusammenarbeit, bei der nicht nur erfolgreiche Messungen entstanden, sondern auch alle Parteien voneinander viel lernen konnten.

- I want to thank the **H.E.S.S. local crew** for their unlimited help during our stay, as well as **Dmitriy Kostunin** and **Gianluca Giavitto** for their remote support even over the Easter holidays!

- Ich danke **Dmitry Malyshev**,**Thilo Michel** und **Alison Mitchell** für die erfolgreiche und angenehme Zusammenarbeit in verschiedenen Bereichen.
- Ich danke der **mechanischen Werkstatt**, sowie der **Elektronikwerkstatt**, ohne die nahezu jeder Teil dieser Forschung unmöglich wäre.
- Ich möchte mich auch bei **Johannes Schäfer** und **Benjamin Schwab** für ihre hilfreichen Verbeserungsvorschläge zu vielen Teilen meiner Arbeit bedanken.

It has been a long and very eventful time since I started my PhD, and I experienced many changes during that time. Changes in office mates, in offices, and with the new ECAP even in the building that my office was located in. Changes in collaborators, in my group of friends, and changes of myself, some of which I would have not predicted before. During all this time, however, I constantly felt the familiar atmosphere of ECAP in general, but especially of the people around me. Whether it were my old office mates (**Michi** and **Franzi E.**), my new office mates (**Katrin, Bennie**), or the group of all the PhD students, who not only guaranteed scientific help and support, but essentially turned into a therapy group with our online meetings during Covid times, I could have not asked for a better community! Again it is impossible to mention every single person I am thankful for, but to list some:

- I want to thank **Rodrigo** for bringing much joy into my life, and for the motivation to put genuine emotion into the acknowledgements.
- Thanks to **Kaori** and **Benedetta**, not only for all the fun we have, but also for lending me an ear for my problems and helping me overcome difficult times.
- Ich danke **Franzi L.** für die vielen Momente auf großen sowie kleinen Skalen, in denen sie meinen Tag ein bisschen schöner gemacht hat – von den langen Spaizergängen am Abend, bis zu den flüchtigen Momenten, wenn ich an ihrem Büro vorbei gegangen bin während sie sich mit Kopfhörern hinter ihrem Bildschirm verschanzt hat.

Mein größter Dank gilt allerdings **Naomi Vogel**. Natürlich einerseits, weil sie fast die gesamte Dauer meiner Doktorarbeit an meiner Seite geforscht hat – wir haben zusammen diskutiert, verzweifelt, Erfolge gefeiert, und eine unzählige Anzahl an Stunden zusammen vor dem Bildschirm, im Labor und auf Dienstreisen verbracht. Aber noch viel wichtiger wiegt mir die Tatsache, dass wir nicht nur als Kollegen zusammen gewachsen sind, sondern als echte Freunde. Freunde, die wirklich immer füreinander da waren und sind. Es ist nicht übertrieben zu behaupten, dass ich ohne Naomi an manchen Tagen nicht die Kraft gehabt hätte, in die Uni zu kommen, und schlussendlich nicht das Durchhaltevermögen, meine Arbeit erfolgreich zu Ende zu bringen. So vergänglich alle Erlebnisse, Kontakte und Erinnerungen während einer Doktorarbeit sein mögen, so überzeugt bin ich, dass unsere Freundschaft für immer bleibt!

”What they doin with my telescopes?”